

Space-mapping optimization applied
to the design of a novel electromagnetic
actuator for active suspension

PROEFSCHRIFT

ter verkrijging van de graad van doctor aan de
Technische Universiteit Eindhoven, op gezag van de
Rector Magnificus, prof.dr.ir. C.J. van Duijn, voor een
commissie aangewezen door het College voor
Promoties in het openbaar te verdedigen
op woensdag 26 november 2008 om 16.00 uur

door

Laurențiu Encică

geboren te Boekarest, Roemenië

Dit proefschrift is goedgekeurd door de promotoren:

prof.dr.ir. J.H. Blom

en

prof.dr. P.W. Hemker

Copromotor:

dr. E.A. Lomonova MSc

prof.dr.ir. J.H. Blom vervult namens wijlen prof.dr.ir. A.J.A. Vandenput de rol van 1^e promotor.

This work is part of the IOP-EMVT program (Innovatiegerichte Onderzoeksprogramma's - Elektromagnetische Vermogenstechniek). This program is funded by SenterNovem, an agency of the Dutch Ministry of Economic Affairs.

Copyright © 2008 by L. Encică

Printed by Eindhoven University Press

A catalogue record is available from the Eindhoven University of Technology Library

ISBN: 978-90-386-1464-9

Această lucrare este dedicată părinților mei ...

Contents

1	Introduction	1
1.1	Goal of the thesis	2
1.2	Vehicle stability and (semi-)active suspension systems	2
1.2.1	Roll control	3
1.2.2	Vibration control	5
1.2.3	Commercial solutions	7
1.3	Electromagnetic active suspension	10
1.3.1	Linear actuators	10
1.3.2	Proposed topologies	11
1.4	Design approach: space-mapping	12
1.5	Thesis objectives and organization	14
2	Design requirements for an electromagnetic active suspension	17
2.1	Quarter-car mechanical model of a vehicle	17
2.2	Calculation of the cornering force and the anti-roll force envelope	23
2.3	Reference measurements	30
2.3.1	Strut geometry	32
2.3.2	Elastic properties	36
2.3.3	Damper characterization	38
2.4	Design assumptions	40
2.5	Design requirements	41
2.6	Conclusions and remarks	42
3	Space-mapping optimization	45
3.1	Introduction	45
3.2	Optimization: short theoretical overview	45
3.2.1	Problem statement	46
3.2.2	Solution existence	46
3.2.3	Feasible region, feasible solution, optimal solution	47

3.2.4	Necessary and sufficient optimality conditions	48
3.2.5	The Karush-Kuhn-Tucker optimality conditions	50
3.2.6	Approaches for solving constrained optimization problems	51
3.2.7	Trust-region	53
3.3	Main concept of space-mapping	55
3.3.1	Input mapping	56
3.3.2	Output mapping	59
3.3.3	Parameter extraction	61
3.4	SM and constrained optimization	62
3.5	Review of SM algorithms	64
3.5.1	Original SM	64
3.5.2	Aggressive SM	65
3.5.3	Trust region ASM	65
3.5.4	Hybrid ASM	66
3.5.5	Surrogate model-based SM	67
3.5.6	Implicit SM	67
3.5.7	Output SM interpolating surrogate	68
3.5.8	Manifold-mapping	68
3.6	Convergence of SM algorithms	69
3.7	A new algorithm: aggressive output SM	70
3.8	Numerical examples	71
3.9	SM-based design flow	72
3.10	Conclusions and remarks	76
4	Case I: Tubular linear actuator for active suspension	77
4.1	Introduction	77
4.2	Preliminary design considerations	80
4.3	AOSM size optimization of the tubular actuator	89
4.3.1	Design specifications and problem formulation	89
4.3.2	Coarse and fine models	92
4.3.3	Comparison of obtained results	95
4.4	Solution post-processing	103
4.4.1	Force response	103
4.4.2	Translator skewing	111
4.4.3	Temperature rise and distribution	117
4.5	Conclusions and remarks	121
5	Case II: Novel electromagnetic spring for active suspension	123
5.1	Introduction	123

5.1.1	A pre-prototype: the α -ELMASP	125
5.2	Design requirements: the output force envelope	126
5.3	AOSM size optimization of the α -ELMASP	128
5.3.1	Design specifications and problem formulation	128
5.3.2	Coarse and fine models	130
5.3.3	Results	132
5.4	Novel ELMASP topology	132
5.5	Passive design: AOSM shape-optimization	134
5.5.1	Design specifications and problem statement	136
5.5.2	Coarse and fine models	138
5.5.3	Results	139
5.5.4	Experimental setup and measurements	148
5.5.5	Passive eddy-current damping	155
5.6	Active design	156
5.6.1	Novel design of commutated coils for active ELMASP re- sponse	158
5.6.2	Demagnetization verification	162
5.7	Conclusions and remarks	162
6	Conclusions and recommendations	167
6.1	Space-mapping optimization	168
6.2	The tubular linear actuator solution	169
6.3	The novel electromagnetic spring	169
6.4	Thesis contributions	170
6.5	Recommendations for future research	171
6.5.1	Space-mapping and coarse models	171
6.5.2	Redesign of the electromagnetic spring	172
6.5.3	The future electric car	172
A	List of symbols and abbreviations	173
A.1	Symbols	173
A.2	Abbreviations	177
B	Magnetic equivalent circuit models	179
B.1	MEC model from Section 4.2	179
B.2	MEC model from Section 4.3.2	180
B.3	MEC model from Section 5.3.2	182
C	NdFeB properties	185

Bibliography	195
Summary	197
Acknowledgments	199
Curriculum Vitae	201

1

Introduction

A major consideration for the automotive industry is to provide passenger safety, through optimal road holding, and comfort, for a large variety of road conditions and vehicle manoeuvres. The passenger comfort and safety can be improved by providing an optimal road contact for the tires while minimizing the roll and heave of the vehicle body. The system responsible for this actions is the vehicle suspension, i.e., a complex system incorporating various arms, springs and dampers that separate the vehicle body, i.e., the sprung mass, from the tires and axles, i.e., the unsprung mass. Due their low cost and simple construction, many vehicles are equipped with fully passive suspension systems, incorporating springs, dampers and anti-roll bars with fixed characteristics. Noting that optimal handling and passenger comfort are conflicting objectives, these passive systems can only obtain a compromise between safety and comfort. However, this compromise has been significantly reduced with the introduction of (semi-)active suspension systems. These systems incorporate adjustable elements which provide spring stiffness and damping coefficients adaptable to the road conditions. The majority of the (semi-)active systems are pneumatic or hydraulic solutions which suffer from low efficiencies and response bandwidths, however they are characterized by high force and power densities. Commercial systems incorporating electromagnetic elements exploit the properties of the

magneto-rheological fluids in damper technology or combine rotary actuators and mechanical elements in order to provide an adjustable spring stiffness. However, given their form factor, high force densities and response bandwidth, linear electromagnetic actuators appear as a beneficial solution for a (semi-)active suspension system. Even though no commercial solutions are existing at this date, (semi-)active suspension systems with linear actuators have been proposed and demonstrated [1, 2]. Nevertheless, the same concept has been exploited, i.e., a suspension strut composed of a mechanical spring connected in parallel with a linear actuator.

1.1 Goal of the thesis

An actuator topology that can provide both a zero-power spring characteristic and actuation forces necessary for vibration damping and vehicle body-roll control in a fully electromagnetic active suspension has not been investigated in the literature up to this moment. Therefore, this thesis introduces a novel topology of electromagnetic actuator aimed at replacing both spring and damper in a suspension strut. Furthermore, a design solution is obtained by means of a multi-level optimization approach, i.e., space-mapping, employing a new algorithm variant which is also derived in this thesis. The objectives of the thesis are further detailed in Section 1.5.

The following sections present several essential aspects regarding the vehicle stability and suspension systems, the proposed novel solution and design approach.

1.2 Vehicle stability and (semi-)active suspension systems

Typical vehicle behavior is pitching during braking and acceleration, and rolling in corners. Additionally, road irregularities cause vibrations in the vehicle and twisting forces. The body-roll during cornering is a demanding aspect of the vehicle attitude variation, which, apart from the reduced comfort, impairs the stability of the vehicle. The first impediment to passenger comfort is motion sickness, which is a common by-product of exposure to optical depictions of inertial motion, especially when reading [3]. This phenomenon, called visually induced motion sickness (VIMS), has also been reported in a variety of virtual environments, such as fixed-base flight and automobile simulation [4]. The essential characteristics of stimuli that induce motion sickness is that they gen-

erate discordant information from the sensory systems that provide the brain with information about the spatial orientation and motion of the body. The principal feature of this discord is a mismatch between the signals provided, principally, by the eyes and inner ear, and those that the central nervous system "expects" to receive and to be correlated. Vertical translational oscillatory motion at a frequency of about 0.2Hz is the most provocative [4], [5]. For a given intensity (peak acceleration) of oscillation, the incidence of sickness falls quite rapidly with an increase in frequency above 0.2Hz. Motion at 1Hz is less than one-tenth as provocative as that at 0.2Hz.

1.2.1 Roll control

An actively controlled suspension system should significantly reduce body-roll and vibrations in order to increase both safety and comfort. An important vehicle safety aspect is that taking a turn at a sufficient high velocity causes the vehicle's center of gravity to move with respect to the wheels, hence a potential rollover of the vehicle. An additional influence of roll motions is that traction and steering are reduced (go-cart effect). Hence, reducing roll improves the vehicle steering, since the vehicle sensitivity to fast steering inputs increases due to the fact that the roll is strongly reduced. However, an additional important characteristic of a good suspension is to filter road vibrations. The ideal anti-roll solution would therefore reduce body roll and still maintain independence of the tires on both sides, where compared to passive systems an improved behavior can be achieved by hydraulic systems. The mostly used commercial solution is the anti-roll bar, which can be passive or active.

Passive anti-roll bar

The passive anti-roll bar, also known as stabilizer bar, sway bar or anti-sway bar is oriented parallel to the ground, with the center of the anti-roll bar attached to the chassis serving as a hinge and the ends to the lower control arms of opposite wheels. In fact, it is a torsion spring, a component that springs back when twisted. When the vehicle drives over a bump and the control arms rise simultaneously on both sides and the ends of the stabilizer bar pivot upward with them, and the bar does not influence the behavior. In a turn, however, the control arm on the outer side lifts its end of the bar, and the opposite control arm pulls its end down. By resisting this torsion, or twisting, the anti-roll bar reduces the control arms' movement and minimizes body roll.

A disadvantage of this passive anti-roll bar is the coupling between the left



Figure 1.1: Commercial active anti-roll bar control systems. A rotary equivalent with the actuator situated in the middle [6] is shown in (a), where (b) shows the linear variant [7] with the actuator situated on the right in the picture.

and right side of the vehicle. For example, when a vehicle driving in a straight line hits a bump with only one side of the vehicle, the passive anti-roll bar is twisted by the control arms, and its resistance to this movement results in the other wheel being lifted, reducing road contact and thus wheel grip on that side and transferring the bump to the vehicle body, impairing comfort. This effect is worse when, e.g., during cornering the inner wheel hits a bump, reducing the degree of twisting of the anti-roll bar and thus the vertical force on the outer wheel, possibly resulting in loss of control. To prevent this, commercial active anti-roll systems have been introduced.

Active anti-roll bar

In active anti-roll bars, linear or rotary hydraulic actuators act in series with a conventional passive anti-roll bar to provide forces that resist vehicle roll. These systems reduce anti-roll forces under normal driving conditions and road impacts by lowering the hydraulic pressure in the actuators and thus decoupling the left and right side. During cornering the actuators are pressurized, applying the required anti-roll bar forces to maintain near to zero body roll angle. The active system, shown in Fig. 1.1(a) and (b), not only consists of hydraulic actuator cylinders, but of a power source, a control manifold (with integral valves and a pressure sensor), a controller and on-board vehicle sensors which monitor steering angle, lateral acceleration and vehicle speed. All these dynamic body control systems use hydraulic cylinders to provide the active suspension system which improves vehicle roll behavior and ride control. The advantages and disadvantages for these hydraulic systems are mentioned in Section 1.2.2.

Active roll control, incorporating an actuator placed in series with the anti-roll bar, requires a high force with short stroke and low bandwidth, hence, is more suitable for hydraulic systems than electromagnetic systems. Good results can be achieved with hydraulic actuators having a 1Hz bandwidth. However, for example the response to bumps during cornering is still impaired due to the low bandwidth.

Active anti-roll bars are already commercially available and implemented into vehicles. The solution with a linear hydraulic actuator is used in, e.g., the Dynamic Handling System (DHS) by Delphi [7] and Active Roll Control (ARC) by TRW [8], where the rotary equivalent is used in Dynamic Drive by BMW [6].

1.2.2 Vibration control

Most modern cars are equipped with independent suspensions, where the left and right wheels are connected to the chassis by flexible-joint shafts, instead of being directly connected by a fixed shaft. The wheels, or unsprung mass, are connected to the body, or sprung mass, by the suspension, which can be classified based on the level of external control [9], [10].

Passive suspension

This conventional low-cost suspension principle, shown in Fig. 1.2a, incorporates spring and damper elements with non-variable rates, thus providing a compromise between ride comfort and road holding over a wide range of road/speed conditions. A possible addition to this system is the use of a self-leveling system designed to compensate for variations in static load only, involving time delays of many seconds. Nevertheless, the passive suspension strut is still the dominant choice in all vehicles because of its cost-effectiveness. A more advanced version of the passive suspension is the adaptive suspension, e.g., variable-rate shock absorbers which allow the driver to select ride firmness.

Semi-active suspension

Semi-active, or adjustable, suspensions fill the region between fully passive suspensions, and fully active suspensions. Although hardware requirements for semi-active systems are considerably less compared to the conventional hydraulic fully active systems in terms of pumps, reservoirs and coolers, they still may offer good performances. They are most often characterized by a mechanical spring supporting the static load parallel to a rapidly adjustable damper, which is independently adjustable at each wheel and often uses a closed-loop control,

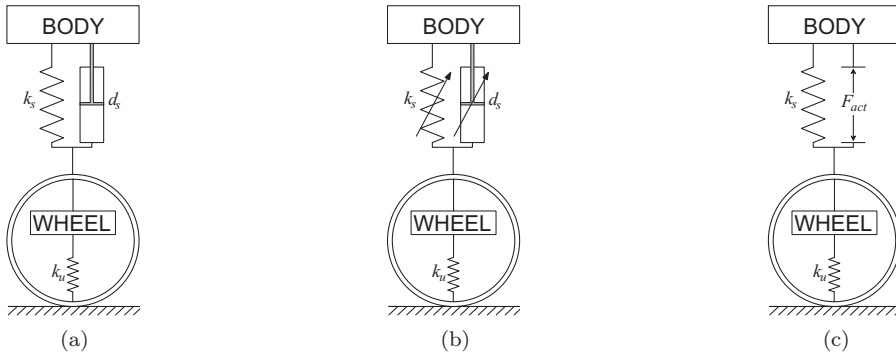


Figure 1.2: Schematic quarter-car representation of (a) passive suspension, (b) semi-active suspension and (c) active suspension.

as shown in Fig 1.2b. The semi-active damping system must be contrasted with the previously mentioned adaptive (damper) systems. The semi-active system offers a high bandwidth control for rapidly varying damping properties, hence places an increased demand on the damper hardware. Meantime, the adaptive system exhibits a slow reaction time and less switching cycles, and is only capable of adapting the system parameters to general conditions (not real-time).

Strictly speaking, the semi-active suspension is a passive device, since it contains a spring and an adjustable damper which is solely capable of dissipating power rather than supplying it. These systems are designed to actively maintain the body as flat as possible in order to minimize bouncing, body roll and pitch. More sophisticated adjustable systems monitor wheel motion and match the suspension's firmness to the road surface, hence improving the system performance.

Active suspension

In contrast to semi-active suspensions, which vary the parameters of the passive elements to control ride quality and body movement, active suspensions utilize powerful, fast-acting actuators in addition to / or in place of conventional steel springs and shock absorbers. Therefore, they are able to inject energy into the system, as well as storing and dissipating it. Because present commercial hydraulic systems are able to actively raise and lower the vehicle's chassis independently at all four corners rather than simply firming and softening the

shocks or struts, these systems are more effective in controlling body roll than semi-active systems, but are considerably more expensive.

Conventional fully active suspension systems involve the replacement of the passive suspension elements by a hydraulic actuator that is controlled by a servo valve. Since the natural wheel-hop frequency of a car generally varies between 10Hz and 15Hz, as shown in Section 2.1, the bandwidth of the controller should be high. In addition energy consumption is very high, in the region of 5-10kW [10], albeit that force levels can be reduced by incorporating a mechanical supporting spring parallel to the actuator, shown in Fig. 1.2c.

To summarize, hydraulic systems have certain advantages, such as:

- high force density,
- ease of control and design,
- commercial availability of the various parts,
- reliability,
- commercial maturity,

although disadvantages such as

- high energy consumption (due to the required continuously pressurized system, even on a straight road),
- slow response (due to pressure losses and flexible hoses),
- large mass (due to the large number of parts),
- high level of acoustic noise,
- environmental pollution (toxic flammable hydraulic fluids, additional energy use),

are still subject to improvement. Furthermore, these hydraulic systems need to be designed for their maximum load, which, if this load level does not occur often, causes the system to be more powerful than required for most of the time, thus increasing the weight.

1.2.3 Commercial solutions

Some of the most common commercial available systems for vibration and roll control are presented in this section.



Figure 1.3: Artist's impression of the Sachs ABC suspension strut [16].

Hydropneumatic suspension

Hydropneumatic suspension has been used extensively by Citroën in its Hydractive suspension systems [11], [12]. It basically incorporates an accumulator placed on top of each suspension strut containing an inert gas separated from a hydraulic fluid by a membrane, which are all connected to a main accumulator and pump.

Magneto- and electro-rheological fluid dampers

The electromagnetic damper is already commercially viable in the form of a controllable fluid damper utilizing either electro-rheological (ER) or magneto-rheological (MR) fluid. An MR fluid is a solution of soft-magnetic particles in a synthetic hydrocarbon base fluid. The viscosity of the fluid can be controlled by means of an external magnetic field generated by an excitation coil. In this manner, MR fluid dampers provide semi-active suspension technology with no electro-mechanical valves or small moving parts [13, 14, 15]. They are more suitable for automotive applications, since they are not affected by most impurities and have low sensitivity to temperature variations.

Active Body Control

Active body control (ABC) developed for DaimlerChrysler by Sachs [16] is a very simple construction offering good performance for rolling. It consists of a strut, where the damper is enclosed in the spring, and a hydraulic chamber is present on top of the spring as shown in Fig. 1.3. By filling this chamber with hydraulic fluid, the spring is compressed, and thus the force exerted by the spring increases, although the spring stiffness is not compromised. By compressing the spring, high anti-roll forces can be generated without coupling left



Figure 1.4: Electromagnetic suspension system by Bose Corp [17]. A front suspension unit is shown in (a), where (b) shows the body roll of the test vehicle in a aggressive turn, where the left picture is without and the right picture is with the Bose suspension system.

and right wheels (no anti-roll bar) or stiffening the suspension (no change in spring/damping rate). However, the system is too slow to react to the resonances occurring at 10-15Hz. Furthermore, when the spring is compressed during the corner, the available stroke decreases which results in a decreased performance with respect to bumps in the road.

The Bose linear electromagnetic suspension

An electromagnetic suspension system has been researched by Bose Corp. from the 1980's. To date, prototypes are installed in standard production vehicles, where a combination of superior comfort and control in the same vehicle is achieved [2]. This system, shown in Fig. 1.4, uses a linear electromagnetic actuator and power amplifier on each corner of the car. It employs an air spring supporting the static weight [18] in order to reduce the consumed power, although this spring is not mentioned in other patent publications. For control reasons, each front and rear wheel unit includes a substantive reactive mass damper assembly packaged within the hub of the wheel, damping vertical wheel vibrations [19]. According to the manufacturer [17] this system enables a high bandwidth operation, stiffening of the suspension in corners to counter body roll, raise and lower ride height dynamically, four quadrant operations and the use of less than a third of the power of a typical vehicle's air conditioner sys-

tem. However, to date no design details or commercial tests are available which would enable an accurate comparison with other suspension systems. Nevertheless, this solution illustrated the advantage of an electromagnetic solution, where a closed loop structural vibration control system can be implemented to utilize the actuator bandwidth such that the commanded force is applied without significant phase or amplitude distortion.

1.3 Electromagnetic active suspension

1.3.1 Linear actuators

A brief note about the terms machine, actuator, motor and generator is perhaps necessary for the clearness of the following chapters. *Machine* is the most general term from the four mentioned and it refers to both *actuators/motors* and *generators*. While from linguistic point of view, the terms actuator and motor are not necessarily synonyms, i.e., *to actuate* is defined as "set in motion, cause to operate, to make a machine work" and a motor is "a device that changes electricity or fuel into movement and makes a machine work, a device that causes or increases motion or power" [20], in electrical engineering they generally refer to devices that produce movement. However, motor is mostly associated with the so-called classical machines, while actuator seems to be given a more general meaning and is also associated to other motion producing electromagnetic devices. Therefore, in order to reduce ambiguity, the term machines with two subclasses, i.e., actuators and generators, will be used further on.

Linear electromagnetic actuators develop electromagnetic thrust to produce linear progressive or oscillatory motion without the need for a gearing system.

A detailed classification and comparison of the different types of linear actuators is out of the scope of this thesis (detailed characterization and classification can be found in [21, 22]), nevertheless a short discussion is proposed here and is aimed at differentiating *long-stroke* from *short-stroke* actuators (Table 1.1 summarizes briefly their specific properties).

The main characteristic of the long-stroke actuators is their repetitive configuration along the movement axis coupled with multi-phase excitation. While rotary (multi-phase) machines provide infinite stroke due to their continuous circular configuration, the linear counterparts can provide unlimited stroke only if the primary or the secondary part are infinitely extended. Consequently, all induction, synchronous or switched-reluctance machines are included in this category. In current applications, the stroke range goes from a few centimeters,

Table 1.1: Characteristics and examples of typical long- and short-stroke actuators.

	Long-stroke	Short-stroke
<i>Geometry</i>	repetitive along movement axis	non-repetitive
<i>Excitation</i>	multi-phase	single-phase
<i>Stroke (up to)</i>	a few meters	a few centimeters
<i>Examples</i>	linear induction and synchronous machines	voice-coil and reluctance actuators

e.g., pick and place machines, to hundreds of kilometers, e.g., transportation systems, however in most applications a range up to a few meters would be typical.

Short-stroke actuators are characterized by single-phase excitation and provide a reduced stroke range, i.e., up to several mm-cm, for applications like precision lens focusing or positioning, valve actuation, electromagnetic switches etc. Two main actuator categories can be distinguished here: the Lorentz type (moving coil or moving magnet) and reluctance type (moving iron). In principle, the first can provide linear force versus current and constant force versus displacement characteristics, while the second is characterized by nonlinear force versus current and force versus displacement responses.

1.3.2 Proposed topologies

An active suspension which combines both vibration and active roll control in a strut based topology, thus decoupling left and right wheels, is the optimal solution for an electromagnetic suspension system. It optimally utilizes the properties of electromagnetic systems and since static weight can be supported by a passive device, energy consumption can be maintained at a low level. Furthermore, on straight roads the anti-roll control of the vehicle, for as far as the straight driving and cornering behavior of the vehicle can be separated in this integrated system, does not consume any energy. Two configurations are investigated in this thesis:

- the first solution incorporates a tubular permanent magnet (PM) brushless actuator implemented parallel to a mechanical spring, as shown in Fig. 1.5a.

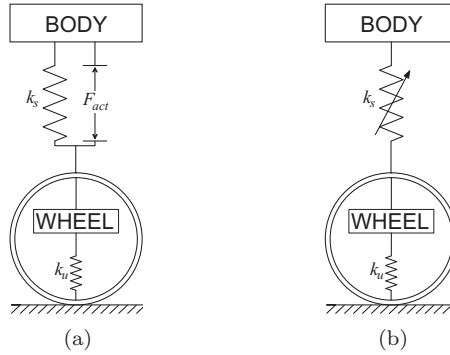


Figure 1.5: Quarter-car representation of (a) a mechanical spring parallel to a tubular actuator and (b) an electromagnetic spring.

- the second solution introduces a novel concept where all conventional mechanical suspension parts are removed. The passive spring is implemented by exploiting the cogging force component given by the attraction between PMs and a slotted iron topology, thus, without power consumption. The dynamic forces on the suspension, due to road noise, bumps or rolling tendency of the vehicle in corners, are compensated by actuation force generated by means of the incorporated excitation coils. This device will be referred to in the rest of this thesis as the electromagnetic spring (ELMASP) and can be schematically represented as an adjustable spring in Fig. 1.5b.

As it will be seen in Chapters 4 and 5, even though the same design specifications apply, the tubular PM actuator falls in the category of long-stroke actuators while the ELMASP configuration belongs to the class of short-stroke actuators.

1.4 Design approach: space-mapping

The structure of the proposed design problems, i.e., number of design variables and specifications and the nonlinear material properties, does not allow for a direct determination of the design solutions. Therefore, an optimization-based design approach is chosen in this thesis.

In mathematics, the term *optimization* refers to the study of problems in

which one seeks to minimize or maximize a real function by systematically choosing the values of real or integer variables from within an allowed set. Optimization has become a necessary part of design activity in all major disciplines, due to the fact that a design problem can be reformulated as an optimization problem whose minimizer coincides with the design solution. From engineering point-of-view, a distinction has to be made between *optimal design* and *design by optimization*. In both cases a given design problem is formulated as an optimization problem and solved by means of an available optimization method. However, considering the technological meaning of the chosen objective function(s) and constraints, the obtained solution can identify an optimal design or just a design which satisfies a given set of finite specifications. For example, if the objective function represents a performance criteria like the efficiency or the force/power density of a given actuator, the set of design variables that maximizes this objective identifies an optimal design. In contrast, if the objective function has to reach a finite value of one of the actuator responses within, for example, a given finite volume constraint, the solution of the optimization does not necessarily represent an optimal design from an engineering point of view.

Very common in electromagnetic or electromechanical design, optimization would be considered only in coherence with simplified models of the studied phenomena. The obtained approximate solution would then be verified on an accurate model and further refined in an iterative process. Nowadays, the rapid development of computer architectures allows for extensive numerical analysis of nonlinear phenomena yielding accurate response estimation for engineering devices and systems. The computational effort required in solving complex optimization problems of electromagnetic devices using such numerical models can still be prohibitive. However, the so-called surrogate modeling techniques have been developed to address this issue. Surrogate models are intended to take the place of the expensive model for the purpose of modeling or optimization of the latter. In optimization using surrogate models, a sequence of subproblems is solved in the search for the optimizer of the expensive model. In the optimization process, most of the model evaluations are performed with the surrogate model. The expensive model is only scarcely evaluated in order to re-calibrate the surrogate [23].

The space-mapping (SM) technique is a type of surrogate-based optimization method which allows expensive electromagnetic optimization to be performed efficiently with the help of fast and approximate coarse or surrogate models. The main idea of the approach is to replace a computationally expensive *fine model* with a *surrogate* based on an iteratively improved *coarse model*, which is significantly less time demanding at the expense of accuracy. Considering the

application area of electromagnetic design, a fine model is most often a numerical discretization of the representative partial differential equations, with finite element analysis being the preferred choice given its versatility, i.e., the capability of handling difficult geometries and nonlinear materials. Whereas, the range of possible coarse models varies from simplified numerical models, e.g., considering coarse discretization and/or linearized material properties, to analytical models or equivalent circuits (magnetic, electric, thermal or mechanical) and the choice and complexity of such models is significantly influenced by the engineering expertise of the designer. SM transforms the regular design approach mentioned above in an automated optimization routine which exploits the advantages of both simplified and complex engineering models, i.e., low computational effort and accuracy, respectively. Therefore, SM-based optimization is chosen in this thesis as a primary design tool.

1.5 Thesis objectives and organization

The main thesis objectives are the following:

1. Employ the SM optimization technique for the design of two actuator solutions for active suspension, i.e., the size optimization of a known type of linear actuator, i.e., a tubular PM actuator and the shape optimization of a novel proposed topology. Considering that prior to the work related to this thesis only one publication [24] has considered the SM technique for the design of an electromagnetic actuator, an overview of the SM optimization technique and publications resulted from the framework of this thesis is given.
2. Propose and compare a set of pre-design solutions, obtained by means of SM-based size optimization, of a tubular PM linear actuator for automotive active suspension.
3. Propose and investigate a novel proof-of-concept electromagnetic spring design that provides both a passive regime, which mimics the behavior of a mechanical spring, and an active regime necessary for vibration damping and vehicle body-roll control. The new actuator topology exploits the so-called cogging force component, which is considered as a parasitic contribution in most types of linear actuators. A linear profile of this force component, i.e., a spring characteristic, is obtained by means of SM-based shape optimization. Furthermore, a novel coil configuration is introduced

to provide a constant shift of the force profile for a constant excitation current, independent of the translator position.

As a first step, the design requirements for electromagnetic active suspension are derived in Chapter 2 from both idealized models and measurements. Once this data is available, fundamental aspects of optimization and the SM technique are presented in Chapter 3 together with an overview of existing SM implementations. Furthermore, a new algorithm variant is derived in the same chapter considering a linear mapping formulation.

The first solution for active suspension, denoted as **Case I**, is investigated in Chapter 4 where SM is employed to obtain a series of pre-design solutions which are compared, from the point of view of the static performance and geometrical characteristics in order to make a feasibility assessment of this particular solution.

The new proof-of-concept ELMASP for active suspension, denoted as **Case II**, is synthesized and dimensioned by means of SM-based shape optimization in Chapter 5. This actuator concept presents a unique topology and a commutated multi-coil configuration which provide the required passive and active response characteristics. An experimental setup is built to verify the linear zero-power response characteristic.

The final conclusions and recommendations are given in Chapter 6.

2

Design requirements for an electromagnetic active suspension

To enable a suitable system performance evaluation it is very important to obtain the requirements for a suspension system in an early stage of the design process. In this chapter these requirements are deduced by firstly discussing the quarter-car model which describes the vehicle in Section 2.1. The approach and measurements data are based on the work found in [25].

The specification of anti-roll, i.e., the maximum force, continuous force, the duty-cycle and the thermal endurance, are derived from a set of equations combined with race-track data in Section 2.2. Specifications for elastic and damping force envelopes are obtained from measurements of passive suspension struts in Section 2.3, followed by a summary of the results in Section 2.5 for the requirements of the active suspension using electromagnetic devices.

2.1 Quarter-car mechanical model of a vehicle

A well known method to evaluate the performance of a suspension system is the use of a quarter-car model, since it provides a proper representation of

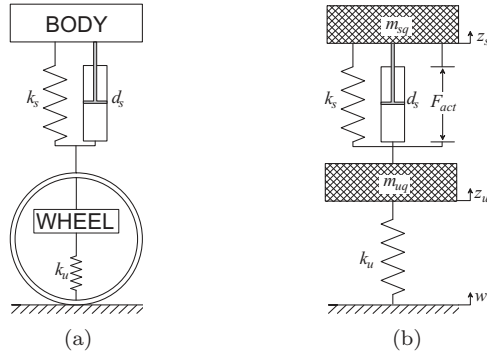


Figure 2.1: Schematic quarter-car representation of (a) passive and (b) active suspension, where the body and wheel mass are represented in (b) as the sprung and unsprung mass, respectively.

the wheel load variations whilst still maintaining simplicity, as it utilizes only a few design parameters, and has a single input. However, the quarter-car model does not include any geometrical effects or longitudinal connections, and can not describe problems related to handling. Nevertheless, it does contain the most basic features of the real problem, i.e., the problem of controlling wheel load variation, suspension working space and vertical vibrations. The quarter-car model has only two vertical degrees of freedom (DoF), viz. vertical displacements of the unsprung mass m_{uq} (quarter of the wheels and axles) and the sprung mass m_{sq} (quarter of the vehicle body), defined by z_u and z_s , respectively. Passive spring stiffness is defined by k_u and k_s , damper coefficient by d_s , and road irregularity by w . All passive components are assumed to be linear, even though in practice their behavior will be neither linear nor symmetrical. The system parameters for a typical vehicle having passive suspension are defined in Fig. 2.1(a) and in Table 2.1. A schematic active suspension, which is able to generate a force, F_{act} , between the sprung mass and the unsprung mass, also incorporating passive elements, is shown in Fig. 2.1(b).

The name 'quarter-car' suggests that this model is valid for all four corners of the vehicle, which is not completely true. The front part of the vehicle can only be described partially with the shown two-mass model, since the power train mounted on elastic mounts actually would be better described by a three-mass model. Therefore, the two-mass model is most suitable for the rear of the vehicle. However, in this thesis the two-mass quarter-car model is used for the

Table 2.1: Typical system parameters for automotive applications.

Quarter body mass	m_{sq}	400kg
Quarter unsprung mass	m_{uq}	40kg
Spring stiffness	k_s	$2.5 \cdot 10^4 \text{N/m}$
Damper coefficient	d_s	$1.2 \cdot 10^3 \text{Ns/m}$
Tire stiffness	k_u	$1.6 \cdot 10^5 \text{N/m}$

entire vehicle for simplification reasons.

Two differential equations are derived from the representation in Fig 2.1(b), and formed into a state-space representation

$$\ddot{z}_s = -\frac{k_s}{m_{sq}}(z_s - z_u) - \frac{d_s}{m_{sq}}(\dot{z}_s - \dot{z}_u) + \frac{F_{act}}{m_{sq}}, \quad (2.1)$$

$$\ddot{z}_u = \frac{k_s}{m_{uq}}(z_s - z_u) + \frac{d_s}{m_{uq}}(\dot{z}_s - \dot{z}_u) - \frac{F_{act}}{m_{uq}} - \frac{k_u}{m_{uq}}(z_u - w), \quad (2.2)$$

where F_{act} is the actuator force, \dot{z}_s and \ddot{z}_s are respectively the vertical velocity and acceleration of the sprung mass, where \dot{z}_u and \ddot{z}_u are velocity and acceleration of the unsprung mass. This results in the state-space representation:

$$\dot{X} = AX + BV, \quad (2.3)$$

$$Y = CX + DV, \quad (2.4)$$

where

$$X = [z_s \quad \dot{z}_s \quad z_u \quad \dot{z}_u]^T, \quad (2.5)$$

$$V = [w \quad F_{act}]^T \quad (2.6)$$

and

$$\dot{X} = \begin{bmatrix} 0 & 1 & 0 & 0 \\ -\frac{k_s}{m_{sq}} & -\frac{d_s}{m_{sq}} & \frac{k_s}{m_{sq}} & \frac{d_s}{m_{sq}} \\ 0 & 0 & 0 & 1 \\ \frac{k_s}{m_{uq}} & \frac{d_s}{m_{uq}} & -\frac{k_s + k_u}{m_{uq}} & -\frac{d_s}{m_{uq}} \end{bmatrix} X + \quad (2.7)$$

$$V = \begin{bmatrix} 0 & 0 \\ 0 & \frac{1}{m_{sq}} \\ 0 & 0 \\ \frac{k_u}{m_{uq}} & -\frac{1}{m_{uq}} \end{bmatrix} V$$

$$Y = \begin{bmatrix} 1 & 0 & 0 & 0 \\ -\frac{k_s}{m_{sq}} & -\frac{d_s}{m_{sq}} & \frac{k_s}{m_{sq}} & \frac{d_s}{m_{sq}} \\ 1 & 0 & -1 & 0 \\ 0 & 0 & 0 & 0 \end{bmatrix} X + \begin{bmatrix} 0 & 0 \\ 0 & \frac{1}{m_{sq}} \\ 0 & 0 \\ 0 & 1 \end{bmatrix} V. \quad (2.8)$$

A Bode representation for the magnitude response of the sprung mass displacement for a passive suspension containing the parameters from Table 2.1 is shown in Fig. 2.2, and exhibits two significant peaks. These peaks respectively are the resonant frequencies of the unsprung mass and sprung mass with the springs, and are equal to 9.2Hz (unsprung mass) and 1.2Hz (sprung mass) in this specific case, as shown in Fig. 2.2. Both resonance frequencies can also be checked in a simple analytical expression:

$$f_s = \frac{1}{2\pi} \sqrt{\frac{1}{m_{sq}} \frac{k_s k_u}{k_s + k_u}}, \quad (2.9)$$

$$f_u = \frac{1}{2\pi} \sqrt{\frac{1}{m_{uq}} (k_u - k_s)}. \quad (2.10)$$

To get an impression of the influence of the spring stiffness and damping rate of the system on the performance, Fig. 2.3 shows the influence of the variation of (a) the damping rate d_s and (b) the spring stiffness k_s on the frequency response. As demonstrated in Fig. 2.3(a) the damping rate does not have any effect on the resonance frequencies, as the damping is not present in (2.9) and (2.10). A

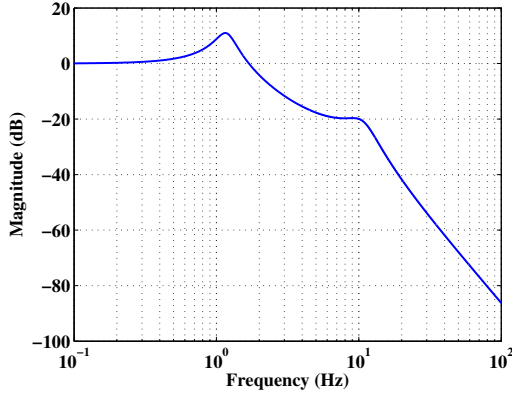
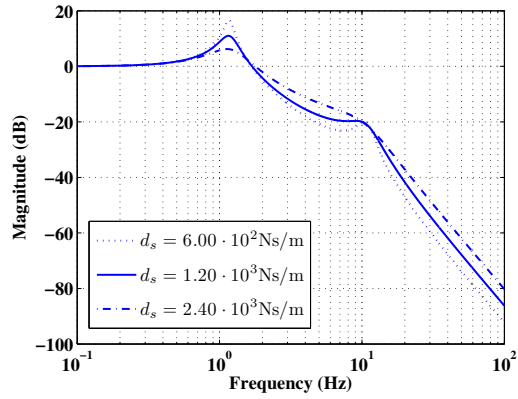


Figure 2.2: Bode representation of the frequency response for w to z_s of the passive suspension ($F_{act} = 0$) using the parameters from Table 2.1.

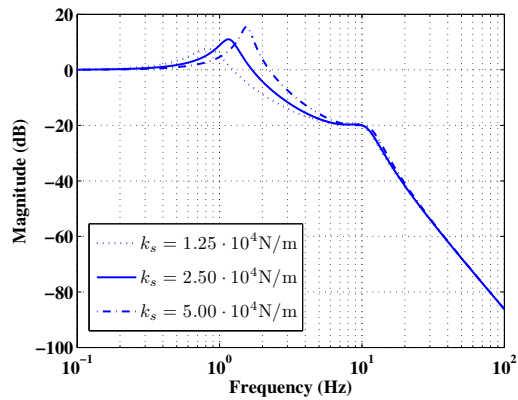
larger damping suppresses the amplitude of these resonance frequencies, which is beneficial in terms of oscillation repression, however a large damping rate dramatically decreases passenger comfort and safety on uneven road conditions, hence a very large damping rate is not preferable. A small damping rate does not suppress the oscillations sufficiently, resulting in large vehicle body articulations.

The influence of the spring stiffness on the frequency response is shown in Fig. 2.3(b), demonstrating that especially the frequency of the first resonance f_s is affected by the spring stiffness. Furthermore the amplitude varies, where lower stiffness implies a smaller peak. The resonance frequency of the unsprung mass f_u is virtually unaffected by the variation in spring stiffness.

An ideal suspension system has a frequency response without any peaks, hence no resonance frequencies. Using a passive suspension it is not possible to suppress both peaks, and thus compromises have to be made regarding comfort and road holding. By implementing semi-active or active suspension at least one of these peaks can be reduced, improving the performance of the suspension regarding frequency response.



(a)



(b)

Figure 2.3: Influence of the damping coefficient (a) and spring stiffness (b) on the frequency response of the sprung mass for a passive suspension system.

2.2 Calculation of the cornering force and the anti-roll force envelope

Due to the suspension geometry, the vehicle body has a longitudinal roll axis around which it rotates during cornering and a lateral pitch axis around which it rotates during braking and accelerating, which both are assumed to be horizontal and to have the same height above road level. The vertical force on the suspension is larger during cornering than it is during braking, since in both cases the suspension has to counteract a similar rolling torque, albeit at reduced arm in the case of lateral acceleration, since the left-right distance (track width) is smaller than the front-rear distance (wheel base). Therefore, the cornering force is taken as a benchmark.

The vehicle is modeled by two rigid bodies, one is to represent the sprung mass m_s (vehicle body), and another one is for the unsprung mass m_u (axles and wheels), as shown in Fig. 2.4. As mentioned, the vehicle body tends to rotate towards the outer side of the corner around the roll axis, marked by \oplus in Fig. 2.4. This produces a rolling torque that is to be counteracted by the suspensions. The vertical road input is omitted, i.e., the transient regions corresponding to the vehicle entering and exiting the corner are not considered, therefore, damping d_s is of no influence. To maintain no body roll (φ is zero), the active suspension is applied to fully counteract the force F_s due to the body roll, discussed hereafter, where the static weight of the body is supported by the springs, k_s . The tires, k_u , having infinite stiffness, support as well the static mass of the vehicle F_{stat} as the dynamic vertical roll force F_{dyn} , or load transfer. This dynamic force is separated into three components resulting from the torques around the rolling axes of the unsprung mass, vehicle and sprung mass, respectively:

- a force component due to the rolling tendency of the unsprung mass around its own center of gravity, F_u ;
- a force component due to the rolling tendency of the sprung mass around the vehicle roll-axis, F_{ra} ;
- a force component due to the rolling tendency of the sprung mass around its own center of gravity, F_s .

When considering the total vehicle without roll, this gives for the vertical dynamic force F_{dyn} on the tires:

$$F_{dyn} = m_{total} \frac{H_{CoG}}{T}, \quad (2.11)$$

where m_{tot} is the mass of the entire vehicle, a is the acceleration towards the center of the circle, H_{CoG} is the height of the center of gravity of the total vehicle and T is the track width which is assumed to be equal for both axles, shown in Fig. 2.4. This anti-roll force should be produced for the full vehicle by the front and rear axle together, hence, the designer has freedom in the ratio of force compensation between the front and the rear axle. By increasing this ratio to one of the axles, the net force along the z -axis, F_z , applied at the outer wheel on this axle increases, and thus the transmitted lateral guiding force along the y -axis, F_y , may reach a value at which the wheel loses road grip. In the case of the front axle, this behavior is called understeer (the car tends to drive in a straight line instead of cornering), and for the rear axle it is called oversteer (the rear of the car overtakes the front). Understeering, where the driver could e.g., brake, is a safer solution than oversteering, where the vehicle could uncontrollably spin. Therefore, consumer cars generally are tuned with understeering properties. A fully active suspension could rapidly determine the optimal force distribution ensuring no under- or oversteering at each moment, hence improving road holding.

Ideally, the suspension should be able to produce more than 100% of the total anti-roll force. In certain situations it could be beneficial to let, for example, one axle produce a force increasing the rolling, whilst the other axle encounters both this extra force and the total cornering force due to the vehicle body. This increases the vertical dynamic forces on that axle, and could help the vehicle in cornering. The roll force distribution ratio, γ , is defined as the ratio between the anti-roll force produced by the axle and the total anti-roll force of the vehicle. In this thesis it is assumed that a maximum of 70% of the required dynamic anti-roll force should be produced by the front suspension (where the rear axle would produce 30%, giving $\gamma_f = 0.7$, $\gamma_r = 0.3$), and a maximum of 50% by the rear axle (where the front axle would produce 50% of the required anti-roll force, giving $\gamma_f = 0.5$, $\gamma_r = 0.5$). The reason to predominantly use the front axle is the slight tendency for (safer) understeer, compared to the (more dangerous) oversteering behavior from the rear axle.

To obtain the required forces on the suspension struts, the force due to the wheel axles (unsprung mass) and due to the roll axis (sprung mass) are calculated and subtracted from the tire forces [26]. Assuming that the height of the centre of gravity of the unsprung mass, H_u , is equal for the front and rear axle, the vertical dynamic force F_{u_f} and F_{u_r} exerted on the tires by the

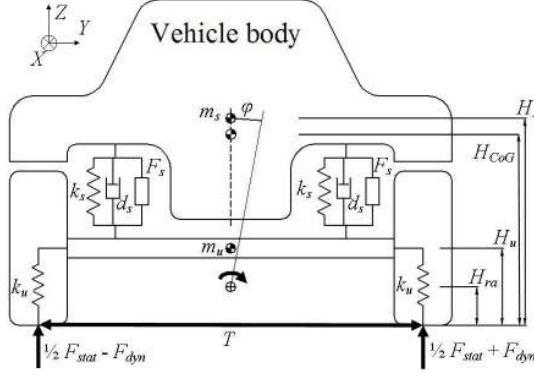


Figure 2.4: Vehicle axle free-body schematic: rear view in left-hand cornering maneuver.

unsprung mass for the front and the rear axle are respectively given by

$$F_{u_f} = m_{u_f} a \frac{H_u}{T}, \quad (2.12)$$

$$F_{u_r} = m_{u_r} a \frac{H_u}{T}, \quad (2.13)$$

where m_{u_f} and m_{u_r} are the weight of the front and rear axle, respectively. Assuming the height of the roll axis, H_{ra} , is equal for both axles, the vertical dynamic tire forces F_{ra} due to the sprung mass acting on the roll axis are respectively given by

$$F_{ra_f} = \psi_m m_s a \frac{H_{ra}}{T}, \quad (2.14)$$

$$F_{ra_r} = (1 - \psi_m) m_s a \frac{H_{ra}}{T}, \quad (2.15)$$

where ψ_m is the ratio of the body mass acting on the front axle, and m_s is the weight of the sprung mass (vehicle body). The third and last component in F_{dyn} is the force due to the rolling tendency of the sprung mass, given by

$$F_s = m_s a \frac{H_s - H_{ra}}{T}, \quad (2.16)$$

where H_s is the height of the center of gravity of the sprung mass, obtained from H_{CoG} , H_u , m_{tot} and m_u in Table 2.2. Summing (2.12) and (2.16) gives the same force value as (2.11).

Table 2.2: Geometrical parameters used in the calculation of the actuator force during cornering.

Description	Quantity	Value	origin
Total mass	m_{tot}	1800kg	BMW 545i
Front unsprung mass	m_{u_f}	96.6kg	BMW 530
Rear unsprung mass	m_{u_r}	89.8kg	BMW 530
Center of gravity height	H_{CoG}	$5.44 \cdot 10^{-1}$ m	BMW 530
Roll axis height	H_{ra}	$8.89 \cdot 10^{-2}$ m	BMW 530
Wheel axle height	H_u	$3.10 \cdot 10^{-1}$ m	BMW 530
Track width	T	1.57m	BMW 545i
Front/total mass ratio	ψ_m	50.9%	BMW 545i
Front suspension force ratio	C_f	0.925	BMW 530
Rear suspension force ratio	C_r	0.980	BMW 530

The anti-roll force ratio γ_f is applied to the total vertical dynamic force F_{dyn} , and F_u and F_{ra} are subtracted for each axle, resulting in the force required at the wheel mount to maintain zero body roll in the corner. Since the struts are not exactly vertically mounted at the wheels, a force ratio, C , between wheel mount and actuator is taken into account, and the required actuator force at both axles is calculated by

$$F_{act_f} = \frac{1}{C_f}(\gamma_f F_{dyn} - F_{u_f} - F_{ra_f}), \quad (2.17)$$

$$F_{act_r} = \frac{1}{C_r}((1 - \gamma_f)F_{dyn} - F_{u_r} - F_{ra_r}). \quad (2.18)$$

A BMW 545i is taken as a reference for the cornering behavior, however, not all required parameters are known for this vehicle, and therefore some data obtained from a BMW530, which is from the same series, is used. The relevant parameters are shown in Table 2.2, where the BMW 545i data is obtained from [27], the BMW530 data from [28]. H_s is calculated from the data in the table. By applying the parameters in the equations (2.11) to (2.18) the resulting actuator force is obtained.

As Fig. 2.5 shows, the dynamic force, and thus the actuator forces increase linearly with the lateral acceleration for zero body roll. To obtain an envelope

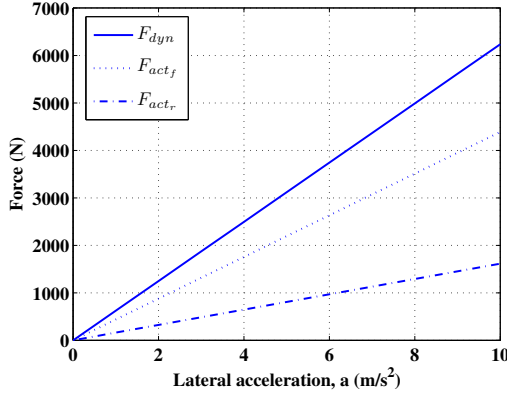
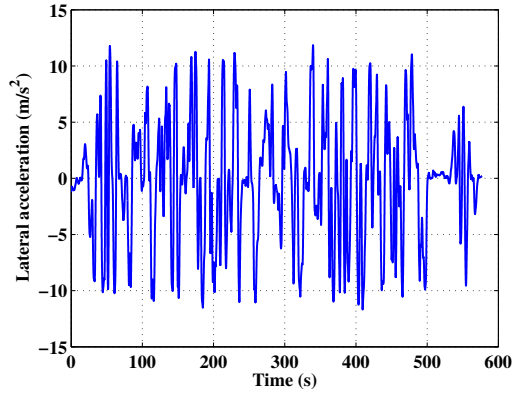


Figure 2.5: Vertical anti-roll force acting on the total vehicle (F_{dyn}) and on the front and rear actuators (F_{act_f} and F_{act_r}) versus the lateral acceleration, when the body roll φ is maintained at zero.

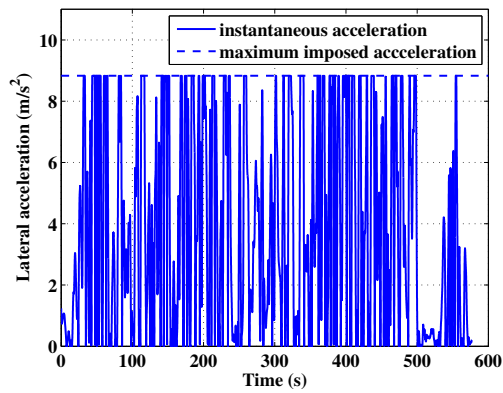
for the forces required to counteract the roll of the vehicle during cornering, test data have been obtained [28] which describe one lap over the Nürburgring race track in Germany. Figure 2.6(a) shows that the lateral acceleration measured in the test vehicle at some points exceeds 10m/s^2 . In this thesis the maximum lateral acceleration the vehicle should be able to withstand without rolling is set at 8.83m/s^2 , or $0.9g$ [29]. As shown in Fig. 2.6(b) the absolute value of the acceleration of Fig. 2.6 is taken and clipped at the maximum of $0.9g$ in order to calculate the required actuator force. At the points where this acceleration is clipped, the produced actuator force remains constant although the acceleration is larger than $0.9g$, and the vehicle gradually begins to roll. It is assumed that this roll does not influence the road behavior of the vehicle.

Considering the worst case where the front axle continuously compensates 70% of the total load transfer, as shown in Fig. 2.5, and the fact that this graph is a straight line, the derivative of this line is extracted, and is equal to $401\text{Ns}^2/\text{m}$ or 401kg . Using this with the data in Fig. 2.6(b), the momentary required force is obtained, which therefore has a maximum value of 3.54kN as Fig. 2.7 shows.

The mean force, F_{mean} , produced by the front suspension under assumed



(a)



(b)

Figure 2.6: Lateral acceleration for a vehicle driving one lap at the old track of the Nürburgring: (a) measured instantaneous acceleration and (b) the absolute value of the instantaneous acceleration clipped at the imposed value maximum value of $0.9g$, i.e., 8.83m/s^2 .

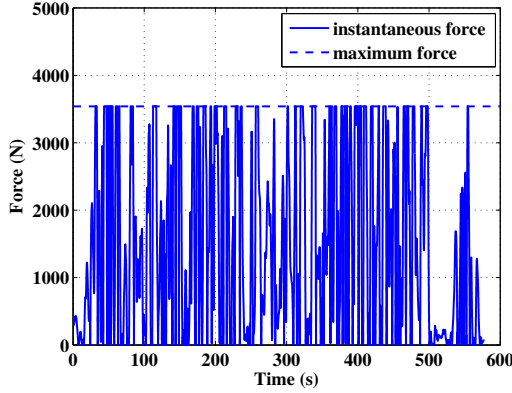


Figure 2.7: Force required to counteract body roll caused by the acceleration data presented in Fig. 2.6b.

conditions is given by

$$F_{mean} = \frac{1}{n} \sum_{i=1}^n F_i, \quad (2.19)$$

where n is the number of samples and F_i is the force measured at the i^{th} sample. Applying this equation to the test data in Fig. 2.7 gives a mean force of 1.59kN. However, one of the limiting factors for electromechanical devices is the maximum actuator temperature. The temperature rise is a direct consequence of the dissipated power, and therefore this power is a more suitable indicator than the produced force. The dissipation of the device can be described by means of the power duty cycle, indicating the ratio between the net dissipated power and the power that would be dissipated at a continuous operation with maximum force. By applying

$$d_p = \frac{1}{F_{max}^2} \left[\frac{1}{n} \sum_{i=1}^n F_i^2 \right], \quad (2.20)$$

where F_{max} is the maximum produced force, a power duty cycle of 33% is obtained. Obviously, reducing this power duty cycle to the force (square root)

and multiplying it with the maximum force F_{max} gives the RMS force:

$$F_{RMS} = \sqrt{\frac{1}{n} \sum_{i=1}^n F_i^2}, \quad (2.21)$$

which returns a value of 2.04kN. It is assumed that the thermal capacitance of the actuator is sufficiently large with respect to the frequency of the force variation and thus heat production. The power duty cycle can therefore be regarded either as the actuator dissipating the full power for 33% of the time, and being at rest for the rest of the time, or as the actuator producing 33% of the full power continuously. Since the power duty cycle can be reduced to the force as shown above, the power duty cycle can also be regarded as a continuous production of the RMS force, or 2.04kN. More specifically, instead of having a power duty cycle of 33% due to the force required to complete a lap at the Nürburgring as shown in Fig. 2.6(c), the actuator should be able to produce a continuous force of 2.04kN. Furthermore, as derived, the maximum force the actuator should produce is 3.54kN. Above results are worst-case, with a constant 70%/30% distribution of the anti-roll force. As a benchmark, it is assumed that this maximum force of 3.54kN is to be continuously produced for a maximum time of 1 min.

2.3 Reference measurements

In order to obtain a reference for the envelope in which the active electromagnetically actuated suspension should operate in terms of spring stiffness, stroke and damping force, a conventional front and rear suspension struts have been obtained and characterized. The reference vehicle is a BMW 545i, of which some data obtained from [27] and [30] are shown in Table 2.3. The leading sizes of the struts are summarized in Table 2.4.

The assumption for the nominal load contains the empty vehicle weight of 1700kg plus a driver and a half-filled fuel tank, evenly distributed over all wheels, hence 1800kg. This results in the assumption that the nominal weight on each suspension strut is 450kg, corresponding to a static force of 4.41kN. The struts, that have been measured, come from the sport version of the 545i, which presents stiffer shock absorbers than the regular road version.

Table 2.3: Technical data and assumptions for the BMW 545i.

Type	E60
Year	Sept. 2003
Serial number	B067069
Empty weight	1700kg
Weight distribution front / rear	50.9% / 49.1%
Maximum axle load front / rear	1070kg / 1235kg
Assumed nominal vehicle weight	1800kg
Assumed nominal suspension force	$4.41 \cdot 10^3\text{N}$

Table 2.4: Leading geometrical parameters for the passive BMW545i suspension struts.

Unit	Value rear	Value front
Total length (excluding thread)	0.60m	0.53m
Damper housing length	0.38m	0.40m
Damper diameter	$5.5 \cdot 10^{-2}\text{m}$	$6.5 \cdot 10^{-2}\text{m}$
Spring diameter (relaxed)	0.11m	0.16m
Stroke (total minus damper housing length)	0.22m	0.13m

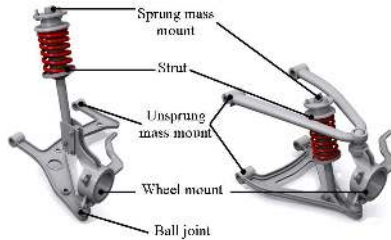


Figure 2.8: Schematic representation of the front suspension in the McPherson topology (left) and the rear unequal-length A-arm suspension (right) [12].

2.3.1 Strut geometry

In order to understand the geometry and exact functions of the struts, their properties are briefly discussed below. The front suspension strut of the BMW 545i is a so-called McPherson strut. This type of suspension is a commonly used suspension due to its compactness and low cost. The system consists of a single strut comprising a spring and shock absorber, which pivots on a ball joint on the single, lower arm, without an upper control arm, as schematically shown in Fig 2.8. Especially for vehicles where engine and transmission are all located inside the front compartment a small-sized suspension like the McPherson strut is the most suitable. Nevertheless, the angle between the axis around which the wheel revolves and the horizontal, called camber, is influenced by body roll and vertical wheel movement. For steering the strut and shock absorber housing are physically twisted to turn the wheel. Therefore, the strut is seated in a special free rotating plate at the top of the assembly which allows this twisting.

The rear suspension strut is an unequal-length A-arm design, deduced from the double wishbone suspension. This suspension type, schematically shown in Fig 2.8, comprises of two A-shaped arms forming a parallelogram which allows the wheel spindles to travel vertically up and down. Although camber control is very good for this suspension type, it causes slight side-to-side motion due to the arc that the wishbones describe around their pivot points when compressed. This side-to-side motion is known as scrub, which is inevitable unless the links are infinitely long. Both the front and rear suspension are shown in Fig 2.9.

A suspension strut is generally characterized by five parameters: the support spring, the rebound spring, the bump-stop, the damper and the Coulomb friction. The first three parameters are elastic, hence, the force depends on the

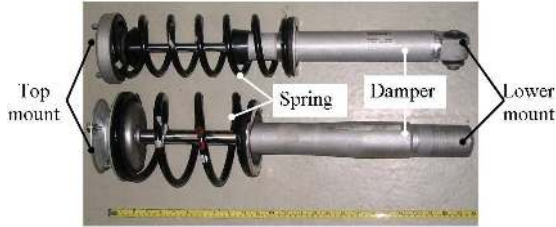


Figure 2.9: Picture of the front (lower) and rear (upper) suspension struts of a BMW545i (no bump-stops mounted).

displacement z . The damping force is solely related to the velocity v , whilst the Coulomb friction, discussed below, is a virtually constant force which solely depends on the traveling direction. The direction of suspension travel is described by the *bump* and the *rebound*, where automotive conventions are that bump is the direction in which the strut is more compressed (z decreases), and rebound is the direction in which the strut is less compressed (z increases).

Schematic views of both struts are shown in Fig. 2.10. Both geometries will be discussed by their elastic and damping properties, followed by measurement results.

Mechanical springs

The top and lower mount of the suspension struts, schematically shown in Fig. 2.10(a) and (b), are the connection points to the sprung and unsprung mass, which is supported by the support spring. Furthermore, the front strut incorporates a rebound spring located inside the damper cylinder. This rebound spring is on one side attached to the frame, where its length is smaller than the stroke of the device, as shown in Fig. 2.10(a). When the strut is fully compressed, the total external force is counteracted by the support spring, since the rebound spring is fully relaxed and at one side floating in air, where this rebound spring is excited at some point when decompressing the strut. Since the rebound spring's geometric position is reversed to the support spring, both components counteract each other, therefore the rebound spring cancels a part of the force produced by the support spring. By doing so, the external force on the strut decreases more rapidly for a small compression, hence the total spring stiffness is larger at low compression compared to the spring stiffness at high compression.

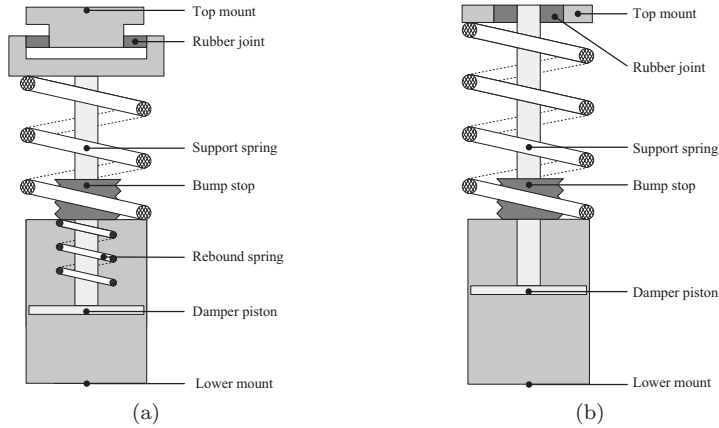


Figure 2.10: Schematic drawing of geometries deduced from the measurements for (a) the BMW 545i front suspension strut measurements and (b) the BMW 545i rear suspension strut.

The rebound spring is especially useful in driving across relatively large road irregularities, and during cornering since the rebound spring provides a larger spring stiffness at low compression. In the first situation the rebound spring is not excited when driving onto the bump, e.g., a kerb, as the compression increases, however when driving off the bump the suspension stroke should increase rapidly for the wheel to closely follow the road surface. In this case, where z is positive, the rebound spring increases the total spring stiffness, and herewith the force ($F_{dyn} + F_{stat}$) that pushes the wheel onto the road, improving the vehicle behavior. During cornering the discussed vehicle tendency to lean outwards causes the inside suspension to rise and the outside to drop. The rebound spring maintains a low rising rebound stroke at the inner wheel, since the large stiffness for rebound compression ensures that the stroke is smaller for a given dynamic force F_{dyn} , hence reducing roll. By acting so, it prevents the strut from hitting the suspension support. However, since the BMW 545i incorporates an anti-roll bar, the influence of the rebound spring on cornering behavior is reduced.

Coulomb friction

In an ideal suspension the springs are purely elastic, hence the force magnitude does not depend on the direction, speed or acceleration of the suspension. However in practice, some friction is apparent in the suspension strut, which in spring characterization measurements is most evident as a fixed force deviation between the inward and outward stroke. This deviation is caused by the Coulomb friction force, which is the commonly known minimal external force required to move any object over a surface. The energy dissipated in this process can be compared to hysteresis loss, dependent on the direction of movement.

Rubber parts

In a suspension strut the damper generally is not directly connected to the top mount of the strut and thus to the body of the vehicle. A rubber joint separates these parts, and provides some comfort in case a significant bump is hit (high velocity). In such an occasion the damper is very rigid, and the high frequencies occurring in the unsprung mass are filtered by this rubber joint which prevents transfer to the vehicle body, hence providing some extra comfort. This construction is seen in the rear strut as Fig. 2.10(b) shows. In the front strut shown in Fig. 2.10(a) however, both damper and spring are connected to the top mount by this rubber joint.

In order to prevent the strut from reaching the end of its stroke when highly compressed, specially shaped rubber modules called bump-stops are inserted over the damper shaft, as shown in Fig. 2.10. These bump-stops gradually increase the elastic force for high compression, mainly for comfort and material lifetime reasons.

Damper

Vehicle damping is an important parameter with respect to both driveability and comfort. A very stiff damper transfers too much road irregularities to the body of the vehicle, which impairs comfort although road holding is improved, whilst a very soft damper will not damp the resonances in the system sufficiently which compromises safety in manoeuvres.

In order to ensure optimal ride comfort and road grip for the passive suspension, the bump damping and the rebound damping have different values. When a bump is hit by the vehicle, the unsprung mass will follow the contours of this bump, since its movement is restricted by the bump on one side (neglecting the compression of the tire), and the suspension connecting it to the inertia of

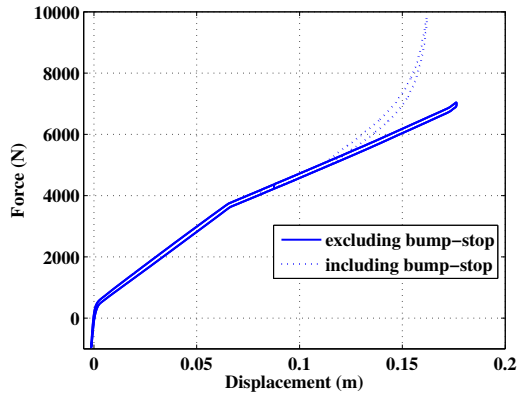
the vehicle body on the other side. The acceleration of the wheel in such steep bumps can be large, rapidly compressing the suspension. In order to prevent excessive forces and thus transmission of the vertical movement to the vehicle body in such occasions, bump damping has a relatively low value.

When driving off a bump, the retraction acceleration of the suspension is lower, since velocity and acceleration are limited by gravity and the rebound force of the spring, and therefore the rebound damping is higher than the bump damping. In a well-designed passive damper the rebound damping is below a maximum value which ensures that the unsprung mass is able to follow the road contours without transmitting large forces to the sprung mass up to a certain degree, thus reducing comfort, and above a minimum value which ensures sufficient energy dissipation, in order to prevent undesired oscillations.

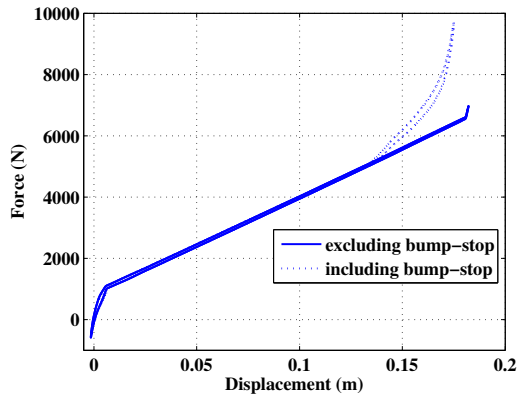
2.3.2 Elastic properties

Spring constants have been obtained by using a low-frequency triangularly-shaped waveform for the input z , and simultaneously measuring the output force. The amplitude and equilibrium point of the waveform are chosen within the maximum stroke of the device, whilst its frequency is of such a low value that damping is negligible (velocities are around 1mm/s). Spring characteristics for the front and rear strut are shown in Fig. 2.11. The derivative of each line is its stiffness k as summarized by Table 2.5. Each measurement includes two full triangular cycles, drawn on top of each other. Furthermore, these measurements have been conducted both with and without the rubber bump-stops, which causes the nonlinear high-force lines (bump-stop) emerging from the straight spring characteristic (no bump-stop) for increasing stroke and force, illustrated in Fig. 2.11. Further, the displacement-derivative of the front strut spring characteristic changes at $z = 0.066\text{m}$, shown in in Fig. 2.11a, due to the implementation of the rebound spring.

Figure 2.11 shows that, if the displacement value for the nominal load of 4.41kN is taken as a reference, little bump movement is allowed before the bump-stops are compressed, influencing the force characteristic. For both struts the bump-stops change the linear characteristic at a dynamic stroke of approximately 0.021m or a dynamic force of 650N above the nominal 4.41kN. Comparing the two characteristics for the front and the rear strut, it turns out that both spring characteristics are very similar, where the bump-stop are employed at approximately the same dynamic displacement with similar characteristics, and support springs which have comparable spring coefficients.



(a)



(b)

Figure 2.11: Spring characteristics of BMW545i: (a) front and (b) rear suspension struts, where each sub-figure shows two separate measurements, i.e., excluding and including the bump-stops, respectively.

Table 2.5: Spring coefficients for the front- and rear strut of BMW545i

Parameter	Range	Value
$k_{support_{rear}}$	$0 - 6.6 \cdot 10^3 \text{N}$	$31.5 \cdot 10^3 \text{N/m}$
$k_{support_{front}}$	$0 - 6.9 \cdot 10^3 \text{N}$	$29.1 \cdot 10^3 \text{N/m}$
$k_{rebound_{front}}$	$0 - 3.7 \cdot 10^3 \text{N}$	$21.0 \cdot 10^3 \text{N/m}$

2.3.3 Damper characterization

The damping has been measured in [25] using a standard VDA (Verband Der Automobilindustrie) test, supplemented with additional points, as the maximum velocity in the standard VDA test is limited to 1.05m/s. This velocity is sufficient for normal road behavior, although for very steep bumps, e.g., a kerb, taken with a high speed, the velocity increases beyond this point. For passive industrial hydraulic dampers this test suffices, since the damping force of those dampers can be extrapolated from these measurements. For electromagnetic actuators this increase of the force for high velocities is not trivial, since the force in these actuators is the result of a controlled current, hence, the produced force which will have a certain maximum.

The required actuator force, derived from the damper measurements, for the electromechanical active suspension is shown in Fig. 2.12. As this figure shows, the bump damping (negative force) increases approximately linearly, where rebound damping is slightly progressive (increasing derivative).

For velocities under 1m/s a force envelope of 2kN suffices to achieve the performance of a passive damper, and with a force of 4kN it is possible to achieve a similar performance up to 1.75m/s.

For the electromagnetic actuator it is also of importance to know the magnitude of the power dissipated by the passive damper, since an electromagnetic actuator is capable of energy recuperation. The energy dissipated per cycle is calculated for all measurements by integrating the force over one full cycle of z , thus calculating the surface of the cycle. By multiplying this energy with the frequency, the dissipated power for a constant sinusoidal excitation is obtained, which is shown in Fig. 2.13, and demonstrates that the dissipated power exponentially increases with the frequency, up to 3kW. Under normal road conditions, the imposed frequencies are low (<1Hz) and thus there is little dissipation. These low frequencies are most common, and the degree of occurrence decreases for higher frequencies and thus velocities.

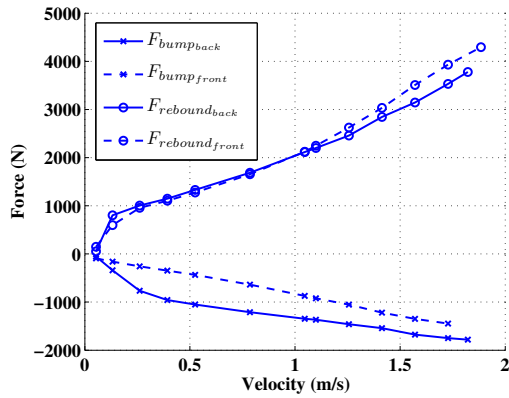


Figure 2.12: Damping force characteristics for the front and rear damper of BMW 545i, where rebound force is positive and the bump force is negative.

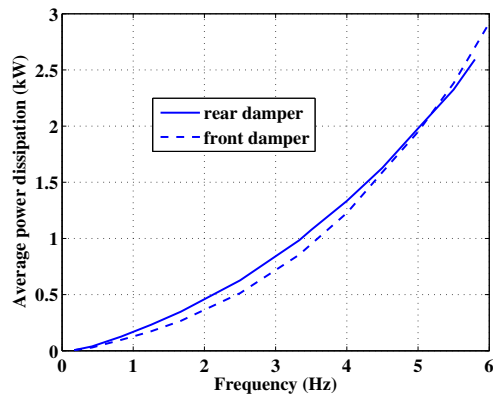


Figure 2.13: Average dissipated power in BMW 545i front and rear damper for a sinusoidal excitation with an amplitude of 0.05 mm.

2.4 Design assumptions

A complete multidisciplinary design would require the detailed knowledge of the entire system in which the actuator is to be incorporated, e.g., power supply capabilities and mechanical and thermal properties of the neighboring components. These characteristics could be determined for a typical existing car model and, consequently, the design aim would be to adapt the actuator characteristics to the given conditions. However, such suspension systems are mostly envisaged as a solution for future more-electric-cars where many vehicle subsystems are to be redesigned according to new specifications. This thesis is focused only on the electromagnetic design of the two actuator solution with due account of necessary thermal requirements. However, a strict or standardized set of design requirements does not exist and therefore, a number of assumptions and simplifications are proposed in order to introduce a set of design specifications. Firstly, the design requirements concerning the tubular PM actuator (Section 4.3) and the active ELMASP design (Section 5.6) and, secondly, the use of static models for both design cases:

- If the high road surface quality of modern highways is taken as a standard, it could be assumed that the main role of the actuator will be to compensate for body-roll in cornering maneuvers, since road irregularities which would require high damping forces would have a rare occurrence. However, in city traffic road irregularities are more present, nevertheless at significantly lower speeds, and high speed cornering is rather nonexistent. Thus, it can be assumed that a nominal actuator force of 2kN, with a peak of 4kN, is sufficient to cover both typical anti-roll and damping requirements. Generally, for safety reasons, it should be verified that the actuator can provide a maximum force of 7.54kN (anti-roll + rebound damping) at least for a short instant (thermal and demagnetization phenomena have to be investigated in this case).
- From thermal point of view, typical operation conditions are rather unknown. It can be predicted that forced cooling is necessary to provide a force output higher than the nominal level. In a typical situation, a large amount of heat is generated by the engine and transmitted to the suspension elements, while forced air cooling is always present due to the movement of the vehicle. Larger force output is arguably necessary at higher speeds where, actually, the forced air cooling becomes more efficient. Moreover, these external factors are different for each car model and complex measurements or thermal and fluid dynamics simulations would

Table 2.6: Requirements for the anti-roll behaviour of the electromagnetic suspension.

Quantity	Description	Value	Duration
d_p	Power duty cycle	33%	Continuously
F_{RMS}	RMS force	2.04kN	Continuously
$F_{anti-roll_{max}}$	Maximum anti-roll force	3.54kN	<1 min

be necessary. In this thesis, natural cooling and an ambient temperature of 25°C for nominal thrust force are defined as design parameters, and it is assumed that forced air or even water cooling is available if necessary.

- Considering body-roll and low speed road disturbance to be the principal external loads, it can be assumed that, because of the associated low mechanical frequencies, static electromagnetic and thermal models should be sufficient to predict an optimum design solution and they are preferred against the transient, time-dependent models. The use of static models in the optimization process reduces the calculation time by a significant margin, however by disregarding transient phenomena, e.g., eddy-currents or hysteresis, the final accuracy is affected. Nevertheless, the trade-off is considered acceptable in this case and transient analysis is employed as solution post-processing in Sections 4.4 and 5.5.5.

2.5 Design requirements

The required data for the anti-roll behavior of the system obtained in Section 2.2 are shown in Table 2.6. The most critical requirement for this system is the high RMS force, since dissipated power increases with the squared force. The suspension strut measurements from Section 2.3 have led to the requirements shown in Table 2.7.

Although the values in Table 2.6 are relatively clear, the data from Table 2.7 must be seen in the right perspective. The 4kN rebound damping force occurs at a rebound speed of 1.75m/s, which is a very uncommon speed during normal road conditions, and in case it would occur, the duration will be very short since the stroke is limited. The same is valid for the maximum bump damping force of 1.8kN which occurs at a bump velocity as high as 1.8m/s. Therefore, the

Table 2.7: Requirements for the vertical suspension behavior of the electromagnetic suspension.

Quantity	Description	Value
k_s	Spring stiffness	30N/mm
$F_{s_{nom}}$	Nominal static force	4.41kN
s	Stroke	0.17m
$F_{rebound_{max}}$	Maximum rebound damping force	4kN
$F_{bump_{max}}$	Maximum bump damping force	1.8kN
$F_{rebound_{nom}}$	Nominal rebound damping force	2kN
$F_{bump_{nom}}$	Nominal bump damping force	1.3kN

nominal bump and damping force are introduced, which represent the respective damping forces occurring at a velocity of 1m/s, assuming that for normal road conditions (no kerbs taken at abnormal high speeds, etc.) these nominal forces provide a sufficient force envelope. Data on the statistical distribution of these velocities would provide a more comprehensive view on the requirements regarding damping.

For compatibility reasons, it is desirable for the electromagnetic suspension to be sized similarly to the passive suspension struts, hence no re-design would be required for implementing this system in vehicles. These geometrical limits, which were shown in Table 2.4, together with the anti-roll and vertical suspension specification forces are very demanding for the electromagnetic suspension. The geometrical parameters from Table 2.4 are not used as a strict reference, i.e., only the larger dimensions are used as design constraints and combined into a single set of design specs for both front and rear suspension struts. The chosen parameters of the space envelope together and the leading design requirements for vehicle mass suspension, anti-roll and damping, given in Tables 2.6 and 2.7, are summarized in Table 2.8 and are used as reference for Chapters 4 and 5.

2.6 Conclusions and remarks

Design requirements for an electromagnetic active suspension have been defined in this chapter from both calculated and measured data and are further employed in Chapters 4 and 5. Considering that these results are generally de-

Table 2.8: Chosen design requirements for the electromagnetic active suspension.

Quantity	Description	Value
Geometric requirements		
r_t	Outer radius	0.08m
L_t	Axial length	0.60m
s	Stroke	0.17m
Anti-roll characteristics		
F_{RMS}	RMS force (continously)	2.04kN
$F_{anti-roll_{max}}$	Maximum actuator force (<1 min)	3.54kN
Spring characteristics		
k_s	Spring stiffness	30N/mm
$F_{s_{nom}}$	Nominal static force	4.41kN
Damping characteristics		
$F_{rebound_{max}}$	Maximum rebound damping force	4kN
$F_{rebound_{nom}}$	Nominal rebound damping force	2kN

pendent on a the specific vehicle model and, furthermore, that active suspension solutions are implemented only on a limited number of vehicle models, no standardized set of requirements for active suspension exists. Therefore, the results of this chapter can be used as a reference in other studies related to automotive active suspension.

3

Space-mapping optimization

3.1 Introduction

The purpose of this chapter is to present, starting from a short introduction of relevant optimization theoretical aspects in Section 3.2, the SM underlying ideas and the current state of the art in Section 3.3. Furthermore, a new algorithm variant is proposed in Section 3.7 and the general approach considered for solving the design problems from Chapters 4 and 5 is given in Section 3.9.

3.2 Optimization: short theoretical overview

The ability to describe the considered design problem in mathematical terms, i.e., constructing a mathematical model of the involved physical phenomena, is the first step required for solving an optimization problem. Subsequently, the choice of *design variables* and *parameters*, *objective* and *constraint functions* follows from the given technical design specifications. A remark regarding the so-called design parameters is necessary here, due to the fact that in some publications the term actually addresses the design variables: design parameters are entities that do not change during the optimization process, however they

can be used to steer the procedure towards different solutions. Examples of such parameters specific to electromagnetic design include material properties, mechanical loads, amplitude and frequency of input sources. It needs noting that in the case of nonlinear physical properties or phenomena the corresponding parameters are described as functions of the design variables and input sources, e.g., BH curves that describe the nonlinear behavior of soft magnetic materials.

Based on several criteria, the optimization problems can be classified as: size, shape or topology optimization [31], linear or nonlinear, single- or multi-objective, unconstrained or constrained problems, uni- or multi-disciplinary [32, 33]. Most of the practical electromagnetic/electromechanical designs give rise to nonlinear, constrained, single- or multi-objective and often multi-disciplinary optimization problems. Multi-objective optimization is not considered in this thesis and hence the following short theoretical overview will address the class of nonlinear, constrained, single-objective optimization problems. The points covered in this overview are the standard problem formulation, the necessary and sufficient optimality conditions, penalty functions and the trust-region approach. Comprehensive formal mathematical description of the optimization theory together with extensive references can be found in [33].

3.2.1 Problem statement

The general formulation of a nonlinear optimization problem (also denoted as a *nonlinear programming problem*) is given by:

$$\begin{aligned}
 & \text{minimize} && \mathcal{F}(\mathbf{x}), \mathbf{x} \in \mathbf{X} \subseteq \mathbb{R}^n, \\
 & \text{subject to} && g_i(\mathbf{x}) \leq 0, \quad i = 1, \dots, m, \\
 & && h_j(\mathbf{x}) = 0, \quad j = 1, \dots, l, \\
 & && \mathbf{A} \cdot \mathbf{x} \leq \mathbf{b},
 \end{aligned} \tag{3.1}$$

where \mathcal{F} is the *objective function*, g_i and h_j are the *nonlinear inequality and equality constraint functions*, \mathbf{A} and \mathbf{b} define the *linear equality and inequality constraints* and the set \mathbf{X} is a compact subset, i.e., closed and bounded, of \mathbb{R}^n .

3.2.2 Solution existence

The first step, before engaging in the characterization of an optimal solution to the problem in hand, is to prove that such a solution exists. Weierstrass' theorem formally states the conditions in which a minimizer exists: let \mathbf{X} be a nonempty compact set and let $\mathcal{F} : \mathbf{X} \rightarrow \mathbf{Y}$ be continuous on \mathbf{X} . Then, the minimization problem $\min\{\mathcal{F}(\mathbf{x}) \mid \mathbf{x} \in \mathbf{X}\}$ has at least one solution.

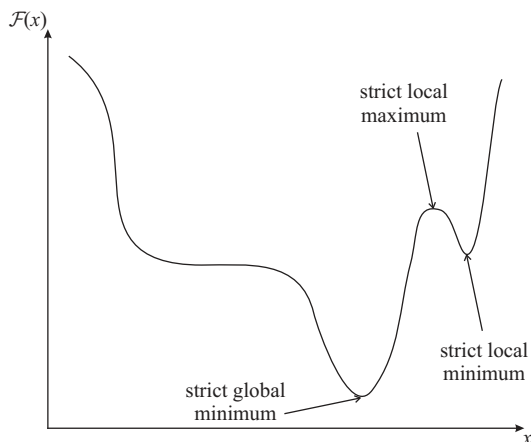


Figure 3.1: Objective function that presents both local and global extrema.

3.2.3 Feasible region, feasible solution, optimal solution

A vector \mathbf{x} satisfying all the constraints is called a *feasible point* and the collection of all such points forms the *feasible region* $\bar{\mathbf{X}}$:

$$\bar{\mathbf{X}} = \{\mathbf{x} \in \mathbf{X} \mid g_i(\mathbf{x}) \leq 0, h_j(\mathbf{x}) = 0, \mathbf{A} \cdot \mathbf{x} \leq \mathbf{b}\}. \quad (3.2)$$

The nonlinear programming problem is to find an *optimal solution*, i.e., a feasible point \mathbf{x}^* satisfying

$$\mathcal{F}(\mathbf{x}^*) \leq \mathcal{F}(\mathbf{x}) \quad \forall \mathbf{x} \in \bar{\mathbf{X}}_\varepsilon \subseteq \bar{\mathbf{X}}, \quad (3.3)$$

where

$$\mathbf{x}^* = \begin{cases} \text{local optimum,} & \bar{\mathbf{X}}_\varepsilon \subset \bar{\mathbf{X}}, \\ \text{global optimum,} & \bar{\mathbf{X}}_\varepsilon = \bar{\mathbf{X}}, \end{cases} \quad (3.4)$$

with $\bar{\mathbf{X}}_\varepsilon$ being defined as neighborhood of \mathbf{x}^* and a subset of $\bar{\mathbf{X}}$. Furthermore, \mathbf{x}^* becomes an *isolated* or *strict* local or global optimum (Fig. 3.1) if and only if

$$\mathcal{F}(\mathbf{x}^*) < \mathcal{F}(\mathbf{x}) \quad \forall \mathbf{x} \in \bar{\mathbf{X}}_\varepsilon \subseteq \bar{\mathbf{X}}, \mathbf{x} \neq \mathbf{x}^*. \quad (3.5)$$

In an equivalent formulation, the optimization problem can be written as follows:

$$\mathcal{F}(\mathbf{x}^*) = \min\{\mathcal{F}(\mathbf{x}) \mid g_i(\mathbf{x}) \leq 0, h_j(\mathbf{x}) = 0, \mathbf{A} \cdot \mathbf{x} \leq \mathbf{b}, \mathbf{x} \in \mathbf{X} \subseteq \mathbb{R}^n\}, \quad (3.6)$$

and, using (3.2), its solution is denoted by

$$\mathbf{x}^* = \operatorname{argmin}_{\mathbf{x} \in \bar{\mathbf{X}}} \mathcal{F}(\mathbf{x}). \quad (3.7)$$

Equation (3.3) gives the basis for the so-called *zero-order methods*, or *direct search methods*, suitable for problems where gradient information is difficult to obtain or not available due to possible causes like discontinuities, numerical noise or very computational expensive models. Examples of zero-order methods include: random walk, pattern search, Powell's method [32] and Nelder-Mead simplex [34], etc.

However, assuming that $\mathcal{F}(\mathbf{x})$ is a twice-differentiable function, the local or global optima are best characterized from mathematical point of view by means of the corresponding Jacobian and Hessian matrices, leading to the first and second order conditions for optimality [33].

3.2.4 Necessary and sufficient optimality conditions

The first order necessary conditions and the second order necessary or sufficient conditions describe the mathematical properties of an extremum and, furthermore, provide the central mechanism for the gradient-based optimization methods. Considering that these properties are symmetrically applicable for minima and maxima, the following discussion is done only in terms of local minima.

First-order necessary conditions

Let $\mathcal{F} : \mathbf{X} \rightarrow Y \subseteq \mathbb{R}$ be differentiable at \mathbf{x}^* . If

$$\mathbf{J}(\mathbf{x}^*) = \nabla \mathcal{F}(\mathbf{x}^*) = 0, \quad (3.8)$$

then \mathbf{x}^* is called a stationary point for \mathcal{F} .

Second-order necessary conditions

Let $\mathcal{F} : \mathbf{X} \rightarrow Y \subseteq \mathbb{R}$ be twice-differentiable at \mathbf{x}^* . If

$$\mathbf{J}(\mathbf{x}^*) = \nabla \mathcal{F}(\mathbf{x}^*) = 0 \text{ and } \mathbf{H}(\mathbf{x}^*) = \nabla^2 \mathcal{F}(\mathbf{x}^*) \geq 0, \quad (3.9)$$

then \mathbf{x}^* is called a local minimum for \mathcal{F} .

Second-order sufficient conditions

Let $\mathcal{F} : \mathbf{X} \rightarrow Y \subseteq \mathbb{R}$ be twice differentiable at \mathbf{x}^* . If $\nabla \mathcal{F}(\mathbf{x}^*) = 0$ and $\mathbf{H}(\mathbf{x}^*) = \nabla^2 \mathcal{F}(\mathbf{x}^*)$ is positive definite, i.e.,

$$\mathbf{H}(\mathbf{x}^*) = \nabla^2 \mathcal{F}(\mathbf{x}^*) > 0, \quad (3.10)$$

then \mathbf{x}^* is a strict local minimum of \mathcal{F} . The inequality (3.10) is considered valid in a neighborhood $\bar{\mathbf{X}}_\epsilon \subset \bar{\mathbf{X}}$ of \mathbf{x}^* . However if (3.10) holds over the entire set $\bar{\mathbf{X}}$, i.e., $\mathbf{H}(\mathbf{x}) > 0 \forall \mathbf{x} \in \bar{\mathbf{X}}$, \mathbf{x}^* is a global minimum. However, most of the practical engineering problems are not characterized by global convexity, therefore the discussion will not be extended further. If desired, identification of possible global minima is performed through extensive search of the design space and, most often, by means of stochastic methods.

In contrast with the zero-order methods (Section 3.2.3), the *first-order methods* exploit the gradient of the objective function in order to determine a search direction (leading to a higher convergence speed) and, possibly, perform a convergence check by means of the first order optimality conditions. Due to the fact that these are not sufficient conditions, the validation of an optimal solution can be realized by a local perturbation of the design variables. Examples of first-order methods are: steepest descent, conjugate gradient and the Broyden-Fletcher-Goldfarb-Shanno quasi-Newton method, etc. The 'quasi-Newton' term identifies optimization algorithms that employ an iteratively updated approximation of the Hessian matrix, e.g., the BFGS update, in contrast with the (modified) Newton method which belongs to the class of *second-order methods* and requires the computation of the second-order partial derivatives. Moreover, as they approach the solution, the quasi-Newton algorithms can present convergence properties similar to the Newton method.

Until this point, the given optimality conditions are directly applicable for unconstrained problems, and the discussion might be also considered valid for constrained problems where the constraints are assumed to be implicitly satisfied, however, without revealing an explicit approach for their treatment. Hence, the optimality conditions are developed further in terms of the gradients of the objective and the given constraints, therefore bringing to the Karush-Kuhn-Tucker (KKT) conditions [32, 33]. It needs noting that, even though only the nonlinear constraint functions are included in the following mathematical results, the discussion can be seamlessly extended to include the linear constraints and the lower and upper bounds imposed on the design vector \mathbf{x} .

3.2.5 The Karush-Kuhn-Tucker optimality conditions

Necessary conditions

Considering the general nonlinear constrained problem defined by (3.1), let \mathbf{x}^* be a feasible solution, and let $I = \{i \mid g_i(\mathbf{x}) = 0\}$. Suppose that \mathcal{F} and g_i for $i \in I$ are differentiable at \mathbf{x}^* , that each g_i for $i \notin I$ is continuous at \mathbf{x}^* , and that each h_j for $j = 1, \dots, l$ is continuously differentiable at \mathbf{x}^* . Further, suppose that $\nabla g_i(\mathbf{x}^*)$ for $i \in I$ and $\nabla h_j(\mathbf{x}^*)$ for $j = 1, \dots, l$ are linearly independent. If \mathbf{x}^* is a local minimum, then unique scalars u_i for $i \in I$ and v_j for $j = 1, \dots, l$ exist such that

$$\nabla \mathcal{F}(\mathbf{x}^*) + \sum_{i \in I} u_i \nabla g_i(\mathbf{x}^*) + \sum_{j=1}^l v_j \nabla h_j(\mathbf{x}^*) = 0, \quad u_i \geq 0 \quad \forall i \in I, \quad (3.11)$$

where u_i and v_j are called *Lagrange multipliers*. In addition, if each g_i for $i \notin I$ is also differentiable at \mathbf{x}^* , then the KKT necessary conditions can be written in the following equivalent form:

$$\nabla \mathcal{F}(\mathbf{x}^*) + \sum_{i=1}^m u_i \nabla g_i(\mathbf{x}^*) + \sum_{j=1}^l v_j \nabla h_j(\mathbf{x}^*) = 0, \quad (3.12)$$

$$u_i \geq 0 \text{ for } i = 1, \dots, m, \quad (3.13)$$

$$u_i g_i(\mathbf{x}^*) = 0 \text{ for } i = 1, \dots, m, \quad (3.13)$$

where the last equation translates into

$$u_i = \begin{cases} = 0, & g_i(\mathbf{x}^*) < 0, \\ > 0, & g_i(\mathbf{x}^*) = 0. \end{cases} \quad (3.14)$$

Under certain convexity assumptions addressing the objective and constraint functions, the KKT necessary conditions are also sufficient conditions [33]. Second order KKT optimality conditions, involving the second order partial derivatives of the objective and the nonlinear constraints, can also be formulated, however, many of the algorithms employ only the first order KKT conditions for verifying the solution optimality. One of the reasons is that verifying the second order conditions would involve the calculation of a $n \times n$ matrix of second order derivatives which is computationally expensive, particularly when the objective value is the result of a complex numerical simulation, e.g., finite elements.

3.2.6 Approaches for solving constrained optimization problems

All the above mentioned zero- and first-order methods and their variants are categorized in the literature as algorithms for unconstrained optimization, i.e., algorithms that through different mechanisms search for a local minimum of a given function (without any other restrictions expressed as constrained functions). There are two classes of methods for solving constrained optimization problems, i.e., the indirect and the direct methods. The indirect methods consider a transformation of the given constrained problem into an equivalent unconstrained one, which is then solved by means of any algorithm for unconstrained optimization. The direct methods exploits low-order expansions of the objective and constraint functions and solves the problem without considering a transformation into an unconstrained equivalent.

Indirect methods

These methods were developed to take advantage of algorithms that solve unconstrained optimization problems and are also referred to as sequential unconstrained minimization techniques (SUMT). As already stated, the given constrained problem is transformed into an unconstrained problem by augmenting the objective function with additional *penalty functions* that reflect the constraint violation. The exterior penalty functions (EPF) are briefly discussed in this section because a particular form of EPF will be employed in Chapter 5.

Considering the problem defined by (3.1), the equivalent EPF unconstrained problem is:

$$\text{minimize } \mathcal{F}_{pen} = \mathcal{F}(\mathbf{x}) + \mathbf{P}(\mathbf{x}, \mu, \nu), \quad (3.15)$$

where μ and ν are penalty multipliers and the penalty function \mathbf{P} is given by

$$\mathbf{P}(\mathbf{x}, \mu, \nu) = \mu \sum_{i=1}^m (\max(g_i(\mathbf{x}), 0))^p + \nu \sum_{j=1}^l |h_j(\mathbf{x})|^p, \quad (3.16)$$

with $p \geq 1$, where the most popular implementations are the so-called l_1 ($p = 1$) and l_2 ($p = 2$) penalty functions. The purpose of the penalty terms is to return high values for infeasible points and vanish otherwise. Theoretically, the equivalent unconstrained problem solves the original constrained problems as the multipliers approach infinity [33]. However, the choice of large multiplier values may lead to computational difficulties as ill-conditioned matrices. Another consequence can be that more emphasis will be placed on the feasibility

and the unconstrained minimization procedure may stop prematurely and return a feasible point that can be far from an optimum. In order to avoid this phenomenon, most of the algorithms using EPF employ a sequence of increasing penalty multipliers, where each new obtained solution is used as a starting point for a new minimization together with updated multiplier values. The terminology of *exterior penalty* indicates that, in general, the solution of the problem is approached from outside the feasible region and feasibility is achieved at the solution.

A particular case of EPF is the l_1 penalty, an exact penalty function with a simple implementation and that will be considered in Chapter 5. It conforms with the form given by (3.16) with $p = 1$ and fixed multiplier values:

$$\mathbf{P}(\mathbf{x}, \mu, \nu) = \mu \sum_{i=1}^m (\max(g_i(\mathbf{x}), 0)) + \nu \sum_{j=1}^l |h_j(\mathbf{x})|. \quad (3.17)$$

The choice of exact multiplier values is supported by a mathematical result [33], which shows that under suitable convexity assumptions there exists a finite multiplier value which will recover an optimum solution. In practice, the l_1 penalty offers a compromise between feasibility and optimality, however, it avoids the earlier mentioned sequential approach. The multiplier values are, in general, problem dependent and making an appropriate selection is not always a trivial task.

Direct methods

As opposed to the previous methods, direct methods do not perform a conversion of the original problem into an unconstrained equivalent. In general, these methods are based on a linear or quadratic expansion of the objective and constraint functions about the current design vector by means of Taylor series. The solution of the original problem is extracted by solving a sequence of simplified constrained problems. For example, the sequential linear programming (SLP) involves linearized objective and constraint functions, whereas the sequential quadratic programming (SQP) associates linearized constraints with a quadratically expanded objective function.

The SQP enjoys a high popularity given its versatility and is usually implemented in commercial software. Generally, the SQP employs quasi-Newton methods to directly solve the KKT conditions (3.12) for the original problem. The core of the method involves the introduction of a quadratic subproblem

(QP):

$$\begin{aligned}
 & \text{minimize} && \mathcal{F}(\mathbf{x}_k) + \nabla \mathcal{F}(\mathbf{x}_k)^t \mathbf{d} + \frac{1}{2} \mathbf{d}^t \mathbf{H}_k \mathbf{d}, \\
 & \text{subject to} && g_i(\mathbf{x}_k) + \nabla g_i(\mathbf{x}_k)^t \mathbf{d} \leq 0, \quad i = 1, \dots, m, \\
 & && h_j(\mathbf{x}_k) + \nabla h_j(\mathbf{x}_k)^t \mathbf{d} = 0, \quad j = 1, \dots, l,
 \end{aligned} \tag{3.18}$$

which returns as solution a search vector \mathbf{d}_k together with a set of Lagrange multipliers (u_{k+1}, v_{k+1}) . Once the search direction has been determined, it is necessary to calculate a step size α_k which will give the next iterate $\mathbf{x}_{k+1} = \mathbf{x}_k + \alpha_k \mathbf{d}_k$, where an auxiliary *merit function* is considered for this purpose. One of the popular implementations of the merit function is based on the l_1 penalty and, hence, α_k is the solution of

$$\begin{aligned}
 \text{minimize} \quad \phi(\mathbf{x}_k + \alpha \mathbf{d}_k) &= \mathcal{F}(\mathbf{x}_k + \alpha \mathbf{d}_k) + \dots \\
 & \mu \sum_{i=1}^m (\max(g_i(\mathbf{x}_k + \alpha \mathbf{d}_k), 0)) + \dots \\
 & \nu \sum_{j=1}^l |h_j(\mathbf{x}_k + \alpha \mathbf{d}_k)|.
 \end{aligned} \tag{3.19}$$

The advantage of (3.19) is that the new iterate \mathbf{x}_{k+1} simultaneously improves the objective value and the constraint satisfaction, therefore, the SQP is included in the class of *methods of feasible directions*, i.e., methods which solve the nonlinear programming problem by moving from a feasible point to an improved feasible point. For a new iteration, \mathbf{x}_k is updated to \mathbf{x}_{k+1} , (u_k, v_k) to (u_{k+1}, v_{k+1}) , \mathbf{H}_k to a positive defined matrix \mathbf{H}_{k+1} , and the QP step is repeated. If the new search direction \mathbf{d}_{k+1} is 0, the algorithm stops with \mathbf{x}_{k+1} being a KKT solution to the original problem. The mathematical foundation and convergence properties of the SQP methods are given in [35, 33].

3.2.7 Trust-region

A widely implemented approach for solving optimization problems where an approximation of the objective function is considered is the trust-region (TR) method. The central idea is general and thus applicable in conjunction with any type of surrogate model, therefore, the TR principle is introduced in the following section.

The common disadvantage of a surrogate model is its decreasing accuracy when moving away from the current iteration point, which can result in the

computation of a new design vector with worse objective value, leading to oscillations or even impeding the convergence of the algorithm. The undesired effects can be prevented by introducing a TR [36], i.e., a small region in the design space, most often centered around the current point, within which the surrogate model is considered to be adequate:

$$\mathbf{X}_k = \{\mathbf{x} \in \mathbf{X} \mid \|\mathbf{x} - \mathbf{x}_k\| \leq \delta_k\}, \quad (3.20)$$

where δ_k is the diameter of the TR. Further, based on the quality of the approximation to the objective function, the TR size is modified and, consequently, the step-length taken for a new iteration is adjusted. The advantage of a TR implementation is schematically illustrated in Fig. 3.2 for a one-dimensional arbitrary problem: without a TR, a large step leading away from the closest minimum is calculated based on a linear expansion about \mathbf{x}_k ; however, a TR restricted step offers a monotonic convergence towards the closest minimum. A simple TR algorithm presents the following structure:

1. Initialization: set \mathbf{x}_0 , δ_0 , $0 < \eta_1 < \eta_2 < 1$ and $0 < \gamma_1 < \gamma_2 < 1$. Compute $\mathcal{F}(\mathbf{x}_0)$ and set $k = 0$.
2. Model definition: define an approximation m_k to \mathcal{F} in \mathbf{X}_k .
3. Step calculation: compute an s_k that sufficiently reduces the model m_k with $\mathbf{x}_k + s_k \in \mathbf{X}_k$, i.e., $m_k(\mathbf{x}_k + s_k) < m_k(\mathbf{x}_k)$.
4. Acceptance of the trial point: compute $\mathcal{F}(\mathbf{x}_k + s_k)$ and define

$$\rho_k = \frac{\mathcal{F}(\mathbf{x}_k) - \mathcal{F}(\mathbf{x}_k + s_k)}{m_k(\mathbf{x}_k) - m_k(\mathbf{x}_k + s_k)}.$$

If $\rho_k \geq \eta_1$ set $\mathbf{x}_{k+1} = \mathbf{x}_k + s_k$, otherwise set $\mathbf{x}_{k+1} = \mathbf{x}_k$.

5. TR size update:

$$\delta_{k+1} \in \begin{cases} [\delta_k, \infty), & \rho_k \geq \eta_2, \\ [\gamma_2 \delta_k, \delta_k], & \rho_k \in [\eta_1, \eta_2), \\ [\gamma_1 \delta_k, \gamma_2 \delta_k], & \rho_k < \eta_1. \end{cases}$$

Set $k = k + 1$ and go to step 2.

As shown in the following section, an SM surrogate is given by a mapping applied to a simplified model and, therefore, the robustness of any SM algorithm can be enhanced by similar TR strategies.

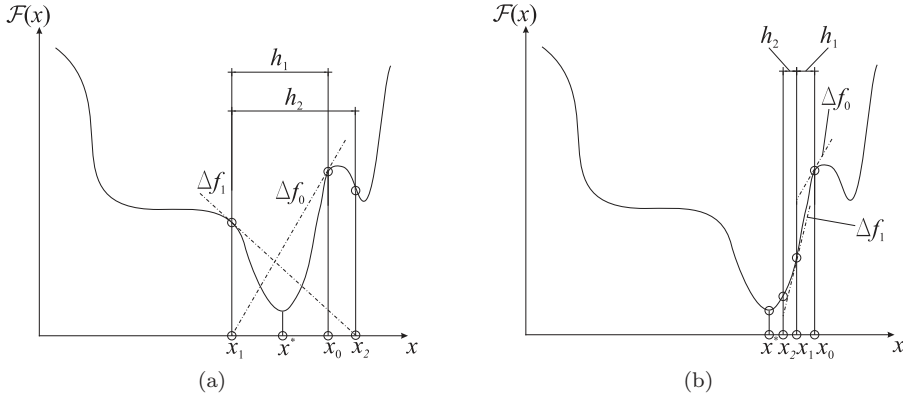


Figure 3.2: The trust-region approach: (a) with an unrestricted step-length, h_k , the optimizer can be trapped in a minimum other than the one indicated by the decent direction, Δf_i , at the initial point, x_0 ; (b) with a step-length restricted by a trust-region the optimizer converges monotonically towards the minimum, x^* , indicated by the decent direction at the initial point.

3.3 Main concept of space-mapping

The main idea of the space-mapping (SM) technique is to replace a computationally expensive *fine model* with a *surrogate* based on an iteratively updated *coarse model*, which is significantly less time demanding at the expense of accuracy. The SM optimization approach [37] has been extensively developed in the last decade [38, 39]. A distinction has to be made between SM for modeling and SM for optimization. In the first case, the purpose is to obtain a surrogate which is close, i.e., a small residual measured in some norm, to the fine model over a large part of the parameter space [40]. In the second case, as considered in this thesis, the purpose is to use the surrogate to obtain the fine model optimum by only scarcely evaluating the latter in the vicinity of the solution.

Considering the application area of electromagnetic/electromechanical design, a fine model is most often a numerical discretization of the representative partial differential equations, where a finite element model is the preferred choice given its versatility, i.e., the capability of handling difficult geometries and non-linear materials. The range of possible coarse models varies from simplified numerical models, e.g., considering coarse discretization and/or linearized ma-

terial properties, to analytical models or equivalent circuits (magnetic, electric, thermal or mechanical) and the choice and complexity of such models is significantly influenced by the engineering expertise of the designer.

Provided a relatively small coarse-fine model misalignment, SM based algorithms are able to converge after only a few evaluations of the fine model. In most SM variants, the surrogate is constructed by mapping the coarse model's input variables, i.e., an input mapping. However, it has been shown that input SM is not expected to yield the exact fine optimum [23, 41], even though the attained accuracy is usually sufficient for practical problems. Hence, the concept of output space-mapping [42] was introduced to address the residual misalignment between the coarse and fine model responses by means of a response or output mapping. The ideas behind input and output SM are summarized in Sections 3.3.1 and 3.3.2.

3.3.1 Input mapping

Consider an accurate model $\mathbf{f} : \mathbf{X} \subseteq \mathbb{R}^n \rightarrow \mathbb{R}^m$ denoted as a fine model. Given an optimization problem, the fine model optimizer is:

$$\mathbf{x}^* = \operatorname{argmin}_{\mathbf{x} \in \mathbf{X}} \|\mathbf{f}(\mathbf{x}) - \mathbf{y}\|, \quad (3.21)$$

where \mathbf{y} is a vector of design specifications. If solving (3.21) is considered to be too expensive, a standard approach is to introduce a so-called coarse model $\mathbf{c} : \mathbf{Z} \subseteq \mathbb{R}^n \rightarrow \mathbb{R}^m$, i.e., an easy to evaluate model, characterized by a lower accuracy. The equivalent problem

$$\mathbf{z}^* = \operatorname{argmin}_{\mathbf{z} \in \mathbf{Z}} \|\mathbf{c}(\mathbf{z}) - \mathbf{y}\|, \quad (3.22)$$

is solved with a significantly lower computational effort, however, \mathbf{z}^* is likely to differ from \mathbf{x}^* . To compensate for the misalignment between the models, a mapping function $\mathbf{p} : \mathbf{X} \rightarrow \mathbf{Z}$ (Fig. 3.3), is defined as:

$$\mathbf{p}(\mathbf{x}) = \mathbf{z} \text{ such that } \mathbf{c}(\mathbf{p}(\mathbf{x})) \simeq \mathbf{f}(\mathbf{x}), \quad (3.23)$$

where $\mathbf{c}(\mathbf{p}(\mathbf{x}))$ is a mapped coarse model employed as a surrogate for the fine model. The mapping, \mathbf{p} , is called an *input mapping* because it maps an input variable of the fine model onto an input variable of the coarse model. In this manner, the direct optimization of the fine model can be avoided and, instead, a solution is determined by solving the optimization problem of the surrogate model given by:

$$\mathbf{x}_{sm}^* = \operatorname{argmin}_{\mathbf{x} \in \mathbf{X}} \|\mathbf{c}(\mathbf{p}(\mathbf{x})) - \mathbf{y}\|. \quad (3.24)$$

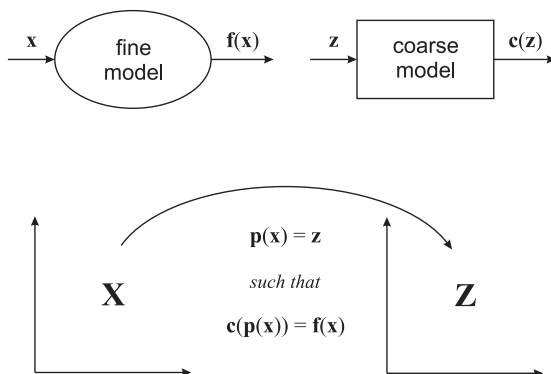


Figure 3.3: Schematic illustration of the original principle of space-mapping, namely the input mapping.

The SM function, \mathbf{p} , is defined as:

$$\mathbf{z}_k = \mathbf{p}(\mathbf{x}_k) = \operatorname{argmin}_{\mathbf{z} \in \mathbf{Z}} \|\mathbf{c}(\mathbf{z}) - \mathbf{f}(\mathbf{x}_k)\|, \quad (3.25)$$

i.e., for a given fine model design vector, \mathbf{x}_k , the mapping delivers the best coarse model design vector, \mathbf{z}_k , that yields a similar response. Most commonly, the input mapping, \mathbf{p} , is defined as an iteratively updated linear mapping, i.e.,

$$\mathbf{z}_k = \mathbf{p}_k(\mathbf{x}_k) = \mathbf{z} + \mathbf{J}_p^k(\mathbf{x}_k - \mathbf{x}), \quad (3.26)$$

where \mathbf{J}_p is the mapping Jacobian. A relation between the model and mapping Jacobians can be derived from (3.23):

$$\mathbf{J}_f \simeq \mathbf{J}_c \mathbf{J}_p, \quad (3.27)$$

where \mathbf{J}_f , \mathbf{J}_c and \mathbf{J}_p are the fine, coarse and mapping Jacobians, respectively. If the coarse and fine model Jacobians are available, the mapping can be established by solving [39]

$$\mathbf{J}_p = (\mathbf{J}_c^T \mathbf{J}_c)^{-1} \mathbf{J}_c^T \mathbf{J}_f \quad (3.28)$$

provided that \mathbf{J}_c has a full rank and $n \leq m$.

A mapping function which maps the true solution, \mathbf{x}^* , onto the optimal solution of the coarse model optimization, i.e.,

$$\mathbf{p}(\mathbf{x}^*) = \mathbf{z}^*, \quad (3.29)$$

is called a *perfect mapping* [23]. In other words, if a perfect mapping exist then the SM solution, \mathbf{x}_{sm}^* , is identical to the real fine model solution, \mathbf{x}^* . However, in general $\mathbf{p}(\mathbf{x}^*) \neq \mathbf{z}^*$ and thus it is unlikely that the solution of (3.24), \mathbf{x}_{sm}^* , will exactly match the fine model solution, \mathbf{x}^* . Conditions for the existence of a perfect mapping are given in [41, 43] and several mathematical results from [43] are summarized in this section:

1. A given set of design specifications \mathbf{y} is called *reachable* for a model $\mathbf{f}(\mathbf{x})$ if

$$\mathbf{y} \in \mathbf{f}(\mathbf{X}) \Rightarrow \mathbf{f}(\mathbf{x}^*) = \mathbf{y}. \quad (3.30)$$

2. A model is called *more flexible* than another if the set of its reachable designs contains the set of reachable designs of the other. Two models are *equally flexible* if their respective sets of reachable designs coincide.
3. If \mathbf{c} is more flexible than \mathbf{f} , i.e., $\mathbf{f}(\mathbf{X}) \subset \mathbf{c}(\mathbf{Z})$, then (a) $\mathbf{c}(\mathbf{p}(\mathbf{x})) = \mathbf{f}(\mathbf{x}) \forall \mathbf{x} \in \mathbf{X}$, and (b) if, additionally, \mathbf{f} is injective then also \mathbf{p} is injective, i.e., (3.25) has unique solution.
4. If \mathbf{f} is more flexible than \mathbf{c} , i.e., $\mathbf{c}(\mathbf{Z}) \subset \mathbf{f}(\mathbf{X})$, then (a) \mathbf{p} is surjective, and (b) if, additionally, $\mathbf{f}(\mathbf{X}) \setminus \mathbf{c}(\mathbf{Z}) \neq \emptyset$ then \mathbf{p} cannot be injective, i.e., (3.25) has multiple solutions.
5. The ideal situation is found if \mathbf{f} and \mathbf{c} are equally flexible and $\mathbf{f} : \mathbf{X} \rightarrow \mathbf{Y}$ is injective, then \mathbf{p} is a bijection and a perfect mapping. Taking into account that perfect mapping is a property that concerns only the solution, the assumptions for this result can be relaxed and stated only in terms of a small neighborhood around the solution (Fig. 3.4a and Fig. 3.4c).
6. Following from (3.25) and (3.29) the property of perfect mapping can be written as

$$\mathbf{p}(\mathbf{x}^*) = \operatorname{argmin}_{\mathbf{z} \in \mathbf{Z}} \|\mathbf{c}(\mathbf{z}) - \mathbf{f}(\mathbf{x}^*)\| = \operatorname{argmin}_{\mathbf{z} \in \mathbf{Z}} \|\mathbf{c}(\mathbf{z}) - \mathbf{y}\| = \mathbf{z}^*, \quad (3.31)$$

which shows that \mathbf{p} is a perfect mapping if either a design is reachable for the fine model (Fig. 3.4b), or if the fine and coarse model give the same optimal response (Fig. 3.4c), i.e., a perfect mapping is guaranteed if

$$\mathbf{f}(\mathbf{x}^*) = \mathbf{y} \quad (3.32)$$

or

$$\mathbf{f}(\mathbf{x}^*) = \mathbf{c}(\mathbf{z}^*). \quad (3.33)$$

The case corresponding to

$$\mathbf{y} \notin \mathbf{f}(\mathbf{X}), \mathbf{y} \notin \mathbf{c}(\mathbf{Z}) \text{ and } \mathbf{f}(\mathbf{x}^*) \neq \mathbf{c}(\mathbf{z}^*), \quad (3.34)$$

is given in Fig. 3.4d and it presents a particular interest since it reveals the disadvantage of the input SM based algorithms. In general, if (3.34) holds then a perfect mapping cannot be guaranteed and, thus, it is not expected for the SM solution to coincide with the real fine model solution, i.e., $\mathbf{x}_{sm}^* \neq \mathbf{x}^*$.

As mentioned above, equally flexible models are most desirable in SM, however this property does not hold for every pair of fine and coarse models used in practice and, therefore, the solution found by input SM may differ from the real solution of the fine model [43]. The case shown in Fig. 3.4c corresponds to the situation in which the models are equally flexible in a neighborhood around the solution and \mathbf{y} is not-reachable. In this situation, the corresponding manifolds tangent at $\mathbf{f}(\mathbf{x}^*)$ and $\mathbf{c}(\mathbf{z}^*)$ are aligned, i.e., $\mathbf{J}_f(\mathbf{x}^*) = \mathbf{J}_c(\mathbf{z}^*)$, and $\mathbf{f}(\mathbf{x}^*) = \mathbf{c}(\mathbf{z}^*)$, therefore, a perfect mapping exists. This condition is not satisfied in the case given in Fig. 3.4d. The flexibility of the models in the latter case can be improved by introducing a transformation which converts the problem from Fig. 3.4d into a problem of the type given in Fig. 3.4c, i.e., a transformation that maps the manifold $\mathbf{c}(\mathbf{Z})$ onto $\mathbf{f}(\mathbf{X})$ at least in the neighborhood of the solution. An input mapping cannot introduce a transformation on the sets $\mathbf{c}(\mathbf{X})$ or $\mathbf{f}(\mathbf{Z})$ and, therefore, the manifold alignment has to be realized by means of a response or output mapping.

3.3.2 Output mapping

With the introduction of an output mapping, the surrogate model becomes:

$$\mathbf{o}(\mathbf{c}(\mathbf{p}(\mathbf{x}))) \simeq \mathbf{f}(\mathbf{x}), \quad (3.35)$$

where $\mathbf{o} : \mathbf{c}(\mathbf{Z}) \rightarrow \mathbf{f}(\mathbf{X})$ and the corresponding surrogate optimization problem is given by

$$\mathbf{x}_{osm}^* = \operatorname{argmin}_{\mathbf{x} \in \mathbf{X}} \|\mathbf{o}(\mathbf{c}(\mathbf{p}(\mathbf{x}))) - \mathbf{y}\|. \quad (3.36)$$

The first output space-mapping (OSM) algorithm, based on a first order Taylor expansion, is proposed in [42] and it aims at compensating for the residual misalignment between the SM solution and the exact fine model solution, thus an input mapping is still employed to reach the vicinity of the solution.

Similar to the input mapping case, if the input mapping is disregarded and a linear output mapping is considered, a relation between the coarse, fine model

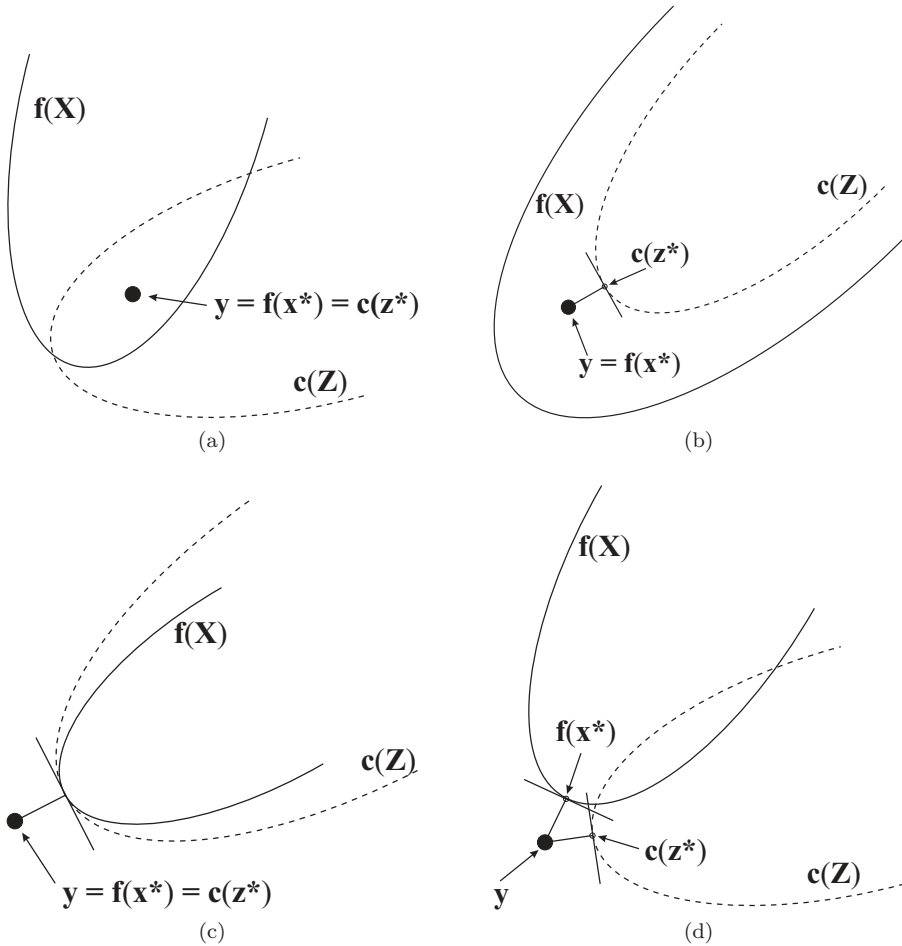


Figure 3.4: Coarse and fine model flexibility, reachable and not-reachable designs: (a) the models are equally flexible in the vicinity of the solution and \mathbf{y} is reachable, (b) the fine model is more flexible and \mathbf{y} is reachable only for the fine model, (c) the models are equally flexible in the vicinity of the solution and \mathbf{y} is not-reachable, (d) the models have different flexibility and \mathbf{y} is not-reachable.

and mapping Jacobians can be obtained here from (3.35):

$$\mathbf{J}_o \mathbf{J}_c \simeq \mathbf{J}_f \quad (3.37)$$

with \mathbf{J}_o being the mapping Jacobian. If the \mathbf{J}_c and \mathbf{J}_f are available, the mapping can be obtained by solving

$$\mathbf{J}_o = \mathbf{J}_f \mathbf{J}_c^T (\mathbf{J}_c \mathbf{J}_c^T)^{-1} \quad (3.38)$$

provided that \mathbf{J}_c has full rank and $n \leq m$.

A mathematical motivation for the aforementioned manifold alignment is given in [41], where following from the close similarity between SM and defect correction [44], the manifold-mapping (MM) technique is introduced. The original MM proposes a special surrogate, based on an affine output mapping:

$$\mathbf{s}(\mathbf{c}(\bar{\mathbf{p}}(\mathbf{x}))) \simeq \mathbf{f}(\mathbf{x}), \quad (3.39)$$

where $\bar{\mathbf{p}}$ is an arbitrary bijective input mapping.

It needs noting that any algorithm which considers an input mapping \mathbf{p} has a potential weak point introduced by the minimization procedure (3.25), also denoted as parameter extraction (PE).

3.3.3 Parameter extraction

Parameter extraction is the key point for many SM algorithms. Its purpose is to determine coarse model design vectors which align the coarse response to the fine response at a given iteration. The PE step is defined by (3.25), which is restated:

$$\mathbf{z}_k = \operatorname{argmin}_{\mathbf{z} \in \mathbf{Z}} \|\mathbf{c}(\mathbf{z}) - \mathbf{f}(\mathbf{x}_k)\|, \quad (3.40)$$

i.e., for a given fine model design vector, \mathbf{x}_k , the PE procedure aims at finding the coarse model design vector, \mathbf{z}_k , that yields a coarse model response, $\mathbf{c}(\mathbf{z}_k)$, as similar as possible to the fine model response, $\mathbf{f}(\mathbf{x}_k)$.

However, it is not guaranteed that the space-mapping function yields a unique value [38]. The problems arising from multiple solutions can be dealt with by means of regularization, where various approaches are proposed in the literature: multi-point PE [45], statistical PE [45], penalized PE [46], aggressive PE [47] or gradient based PE [48]. Recent implementations [49] propose even more complex formulations of the PE subproblem, where the coefficients of both input and output mappings have to be determined. While these enhance the general performance and robustness of the algorithms, the issue related to the

sensitivity of this step remains valid. The PE step can be avoided if the mappings are determined using the available sets of coarse and fine model responses, however, only the derivation of output mappings is possible in this manner.

3.4 SM and constrained optimization

The SM technique can also be applied to problems with constraints. For simplicity of notations,

$$\mathbf{k}_f(\mathbf{x}) \leq 0 \text{ and } \mathbf{k}_c(\mathbf{z}) \leq 0, \quad (3.41)$$

will denote both fine/coarse equality and inequality constraints. Next, the problem (3.21) rewritten to include constraint functions becomes:

$$\mathbf{x}^* = \operatorname{argmin}_{\mathbf{x} \in \mathbf{X}} \|\mathbf{f}(\mathbf{x}) - \mathbf{y}\| \text{ subject to } \mathbf{k}_f(\mathbf{x}) \leq 0 \quad (3.42)$$

and, assuming that both fine model and its respective constraints are functions difficult to evaluate, its coarse counterpart is given by

$$\mathbf{z}^* = \operatorname{argmin}_{\mathbf{z} \in \mathbf{Z}} \|\mathbf{c}(\mathbf{z}) - \mathbf{y}\| \text{ subject to } \mathbf{k}_c(\mathbf{z}) \leq 0, \quad (3.43)$$

where $\mathbf{k}_f : \mathbf{X} \rightarrow \mathbb{R}^k$ and $\mathbf{k}_c : \mathbf{Z} \rightarrow \mathbb{R}^k$. In many practical cases, the model is not closely related to its respective constraints. For example, the model could describe one physical quantity and the associated constraint a completely different one with only a weak dependency relation to the model. Moreover, the extraction of an SM function, which would map simultaneously the objective and constraints, might become a difficult optimization subproblem. A different strategy is proposed in [50], where separate model and constraint mappings are defined. The concept is elaborated in [51, 43] for input mapping based methods with application to electromagnetic actuator design. Two functions are introduced with their respective definitions following from (3.25):

$$\mathbf{p}_m(\mathbf{x}) = \operatorname{argmin}_{\mathbf{z} \in \mathbf{Z}} \|\mathbf{c}(\mathbf{z}) - \mathbf{f}(\mathbf{x})\| \quad (3.44)$$

and

$$\mathbf{p}_k(\mathbf{x}) = \operatorname{argmin}_{\mathbf{z} \in \mathbf{Z}} \|\mathbf{k}_c(\mathbf{z}) - \mathbf{k}_f(\mathbf{x})\|, \quad (3.45)$$

with $\mathbf{p}_m, \mathbf{p}_k : \mathbf{X} \rightarrow \mathbf{Z}$. Further, similar with (3.24), \mathbf{x}^* is the solution of:

$$\mathbf{x}^* = \operatorname{argmin}_{\mathbf{x} \in \mathbf{X}} \|\mathbf{c}(\mathbf{p}_m(\mathbf{x})) - \mathbf{y}\| \text{ subject to } \mathbf{k}_c(\mathbf{p}_k(\mathbf{x})) \leq 0. \quad (3.46)$$

A particular case is found when the coarse and fine models coincide, i.e., $\mathbf{f}(\mathbf{x}) = \mathbf{c}(\mathbf{x}), \forall \mathbf{x}$, and a misalignment is present only between the constraints. Hence \mathbf{p}_m can be disregarded and (3.46) simplifies to:

$$\mathbf{x}^* = \operatorname{argmin}_{\mathbf{x} \in \mathbf{X}} \|\mathbf{c}(\mathbf{x}) - \mathbf{y}\| \text{ subject to } \mathbf{k}_c(\mathbf{p}_k(\mathbf{x})) \leq 0. \quad (3.47)$$

A practical example for this situation is given in [51], where the mass of an electromagnetic device is minimized while output characteristics like force and magnetic field quantities are defined as design constraints. Furthermore, two regularization criteria regarding the PE step are suggested here:

$$\mathbf{p}_{k1}(\mathbf{x}) = \operatorname{argmin}_{\mathbf{z} \in \mathbf{Z}} \|\mathbf{c}(\mathbf{z}) - \mathbf{y}\| \text{ subject to } \mathbf{k}_c(\mathbf{z}) = \mathbf{k}_f(\mathbf{x}) \quad (3.48)$$

and

$$\mathbf{p}_{k2}(\mathbf{x}) = \operatorname{argmin}_{\mathbf{z} \in \mathbf{Z}} \|\mathbf{c}(\mathbf{z}) - \mathbf{f}(\mathbf{x})\| \text{ subject to } \mathbf{k}_c(\mathbf{z}) = \mathbf{k}_f(\mathbf{x}). \quad (3.49)$$

While in first case the preferred solution is the one closest to the specification \mathbf{y} , the second criterion is based on the proximity to the fine model response $\mathbf{f}(\mathbf{x})$. The proposed algorithm [51] will be denoted further as trust region surrogate-based SM (TRSSM) and is derived by replacing the minimization of a mapping residual in the TRASM procedure with the optimization of an SM based surrogate.

The same approach for constrained problems is applicable to output mapping algorithms, with two additional remarks: for simplicity of the presentation (1) an arbitrary input mapping $\bar{\mathbf{p}}$ is considered and (2) the notations \mathbf{o}_m and \mathbf{o}_k stand here for any output mapping algorithm, e.g., OSM, MM [43]. Starting from the fine (3.42) and coarse (3.43) problems, separate mappings addressing the models and their respective constraints are introduced:

$$\mathbf{o}_m(\mathbf{c}(\bar{\mathbf{p}}(\mathbf{x}))) \simeq \mathbf{f}(\mathbf{x}) \text{ with } \mathbf{o}_m : \mathbf{f}(\mathbf{X}) \rightarrow \mathbf{c}(\mathbf{Z}) \quad (3.50)$$

and

$$\mathbf{o}_k(\mathbf{k}_c(\bar{\mathbf{p}}(\mathbf{x}))) \simeq \mathbf{k}_f(\mathbf{x}) \text{ with } \mathbf{o}_k : \mathbf{k}_f(\mathbf{X}) \rightarrow \mathbf{k}_c(\mathbf{Z}). \quad (3.51)$$

Hence, \mathbf{x}^* is now the solution of:

$$\mathbf{x}^* = \operatorname{argmin}_{\mathbf{x} \in \mathbf{X}} \|\mathbf{o}_m(\mathbf{c}(\bar{\mathbf{p}}(\mathbf{x}))) - \mathbf{y}\| \text{ subject to } \mathbf{o}_k(\mathbf{k}_c(\bar{\mathbf{p}}(\mathbf{x}))) \leq 0. \quad (3.52)$$

Finally, in the particular case of $\mathbf{f}(\mathbf{x}) = \mathbf{c}(\mathbf{x}), \forall \mathbf{x}$, the expressions becomes:

$$\mathbf{x}^* = \operatorname{argmin}_{\mathbf{x} \in \mathbf{X}} \|\mathbf{c}(\mathbf{x}) - \mathbf{y}\| \text{ subject to } \mathbf{o}_k(\mathbf{k}_c(\bar{\mathbf{p}}(\mathbf{x}))) \leq 0. \quad (3.53)$$

A detailed discussion on the application of input and output SM for problems with constraints can be found in [43].

The main concept of SM optimization and the general approach for solving constrained optimization problems were presented up to this point without describing the particular implementations of the various algorithms. A non-exhaustive description of the major SM developments is given in the following section. A comprehensive review of the state of the art can be found in [38, 39, 43].

3.5 Review of SM algorithms

3.5.1 Original SM

The concept of the SM technique was introduced in [37]. In its original form, an initial approximation of the mapping, \mathbf{p}_0 , is obtained by performing fine model evaluations at a preselected set of at least m_0 base points, where $m_0 \geq n + 1$. One base point may be taken as the optimal coarse model solution, $\mathbf{x}_1 = \mathbf{z}^*$, with the remaining base points being chosen by local perturbation. A corresponding set of m_k coarse model points is constructed through the PE process (3.25). An affine mapping is assumed between the two spaces, i.e.,

$$\mathbf{z} = \mathbf{p}_k(\mathbf{x}) = \mathbf{B}_k \mathbf{x} + \mathbf{b}_k, \quad (3.54)$$

where $\mathbf{B}_k \in \mathbb{R}^{n \times n}$ and $\mathbf{b}_k \in \mathbb{R}^n$ are determined as the solution of the (over-determined) linear system of equations given by (3.54) for the m_k pairs of coarse and fine model points. The inverted mapping \mathbf{p}_k^{-1} is used to determine a new fine model iteration point as

$$\mathbf{x}_{k+1} = \mathbf{p}_k^{-1}(\mathbf{z}_k), \quad (3.55)$$

and if $\mathbf{f}(\mathbf{x}_{k+1}) \simeq \mathbf{c}(\mathbf{z}^*)$ within an acceptable tolerance, then $\mathbf{x}^* = \mathbf{x}_{k+1}$, else, the set of base points is augmented with $(\mathbf{x}_{k+1}, \mathbf{z}_{k+1})$ and (3.54) is solved for new mapping coefficients.

In spite of its simple form, the algorithm proved to be successful on a number of practical examples [38]. However, it has also revealed some inherent disadvantages: a linear mapping may not be valid for significantly misaligned models and the non-uniqueness in the PE process may lead to an erroneous mapping estimation and algorithm failure.

3.5.2 Aggressive SM

The aggressive SM (ASM) algorithm [52] considers a quasi-Newton iteration for iteratively solving the nonlinear system

$$\mathbf{r}(\mathbf{x}) = \mathbf{p}(\mathbf{x}) - \mathbf{z}^* = 0 \quad (3.56)$$

in order to obtain \mathbf{x}^* . Assuming that \mathbf{x}_k is the k^{th} iteration in the solution of (3.56), the next iteration \mathbf{x}_{k+1} is given by the quasi-Newton step

$$\mathbf{x}_{k+1} = \mathbf{x}_k + \mathbf{h}_k, \quad (3.57)$$

where \mathbf{h}_k is obtained from

$$\mathbf{B}_k \mathbf{h}_k = -\mathbf{r}(\mathbf{x}_k) \quad (3.58)$$

with \mathbf{B}_k being an approximation of the Jacobian of the residual vector \mathbf{r} at \mathbf{x}_k . There are several options regarding the calculation of \mathbf{B}_k [39] from which the most popular is the rank-one Broyden update [53]:

$$\mathbf{B}_{k+1} = \mathbf{B}_k + \frac{\mathbf{r}_{k+1} - \mathbf{r}_k - \mathbf{B}_k \mathbf{h}_k}{\mathbf{h}_k^T \mathbf{h}_k} \mathbf{h}_k^T. \quad (3.59)$$

3.5.3 Trust region ASM

The trust region ASM (TRAS) [54] considers a TR approach (Section 3.2.7) aiming to improve the global algorithm behavior. Hence, the iteration step \mathbf{h}_k is determined as the solution of a TR sub-problem and not as a quasi-Newton step. At each iteration, the residual function $\mathbf{r}(\mathbf{x})$ is replaced by a linearized local approximation

$$\mathbf{l}_k(\mathbf{x}_k, \mathbf{h}_k) = \mathbf{r}_k + \mathbf{B}_k \mathbf{h}_k, \quad (3.60)$$

and \mathbf{h}_k is the solution of the subproblem

$$\mathbf{h}_k = \operatorname{argmin}_{\|\mathbf{h}\|_2 \leq \delta_k} \|\mathbf{l}_k(\mathbf{x}_k, \mathbf{h})\|_2^2. \quad (3.61)$$

The solution of (3.61) can be found also by solving the system

$$(\mathbf{B}_k^T \mathbf{B}_k + \lambda_k \mathbf{I}) \mathbf{h}_k = -\mathbf{B}_k^T \mathbf{r}_k, \quad (3.62)$$

where λ_k is the parameter which controls the step length.

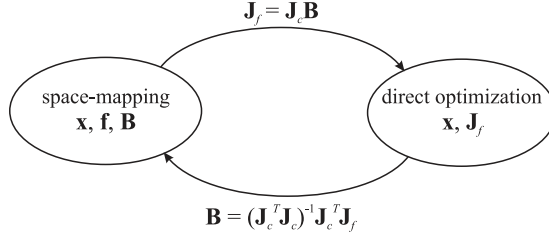


Figure 3.5: Switching between SM and direct optimization in the HASM algorithm [55].

3.5.4 Hybrid ASM

As stated in Section 3.3.1, SM yields the real fine mode solution only under certain conditions. A hybrid approach in combination with standard direct fine model optimization is proposed in [55]. The so-called hybrid ASM (HASM) algorithm starts with an SM optimization phase and defaults to a classical optimization approach when SM fails. Equations (3.27) and (3.28) are considered in order to enable the switching between SM and direct optimization, where the switching mechanism is schematically described in Fig. 3.5. The convergence properties of the HASM algorithm are studied in [23].

Remark

The base of the original SM, ASM, TRASM and HASM algorithms is a formulation in which the SM solution is found as the minimizer of the mapping residual (3.56), or in a more general form:

$$\mathbf{x}_p^* = \operatorname{argmin}_{\mathbf{x} \in \mathbf{X}} \|\mathbf{p}(\mathbf{x}) - \mathbf{z}^*\|. \quad (3.63)$$

Formulation (3.63) is termed in [41] as the *primal* SM approach, in contrast with the different formulation given by (3.24), which is denoted as the *dual* SM approach:

$$\mathbf{x}_d^* = \operatorname{argmin}_{\mathbf{x} \in \mathbf{X}} \|\mathbf{c}(\mathbf{p}(\mathbf{x})) - \mathbf{y}\|. \quad (3.64)$$

The conditions in which the primal and dual formulations become equivalent and their solution coincides with the real fine model solution are also stated in [41]. The subsequent SM developments, presented in Sections 3.5.5 to 3.5.8, follow the dual approach.

3.5.5 Surrogate model-based SM

The idea of an SM-based surrogate model, similar to (3.23), is for the first time introduced in [56]. The proposed algorithm exploits a convex combination of a mapped coarse model and a linearized fine model:

$$\mathbf{t}_k(\mathbf{x}) = w_k \mathbf{c}(\mathbf{p}_k(\mathbf{x})) + (1 - w_k)(\mathbf{f}(\mathbf{x}_k) + \mathbf{J}_f^{(k)}(\mathbf{x} - \mathbf{x}_k)), \quad (3.65)$$

where $w_k \in [0, 1]$ and \mathbf{p}_k is the linearized input mapping given by:

$$\mathbf{p}_k(\mathbf{x}) = \mathbf{p}(\mathbf{x}_k) + \mathbf{B}_k(\mathbf{x} - \mathbf{x}_k). \quad (3.66)$$

Switching between the two models is realized by means of the w_k factor, i.e., for $w_k = 0$ the surrogate is a mapped coarse model, whereas for $w_k = 1$ the surrogate becomes a linearized fine model. Different strategies for 'soft' or 'hard' switching are proposed in [57].

3.5.6 Implicit SM

The implicit SM (ISM) [58] is an attractive concept, although it is more application dependent than the other SM implementations. ISM stands in a class of its own in the sense that, in its original form, no explicit mapping function is considered. Instead, a set of preassigned model parameters, $\boldsymbol{\eta} \in \mathbb{R}^r$, other than the model variables, are extracted in order to align the fine and coarse models. In other words, a selected number of coarse model coefficients, which for example approximate certain physical properties like nonlinear material properties, are updated using information obtained from the fine model in order to improve the coarse model. A parallel between these preassigned parameters and the design parameters defined in Section 3.2 is directly visible at this point. The ISM surrogate is an iteratively updated coarse model:

$$\mathbf{c}(\mathbf{z}(\boldsymbol{\eta}_k), \boldsymbol{\eta}_k) \simeq \mathbf{f}(\mathbf{x}), \quad (3.67)$$

where the $\boldsymbol{\eta}_k$ vector is either directly available from the fine model simulations or it is obtained as the solution of the PE sub-problem

$$\boldsymbol{\eta}_k = \operatorname{argmin}_{\boldsymbol{\eta} \in \mathbb{R}^r} \|\mathbf{c}(\mathbf{z}_k, \boldsymbol{\eta}) - \mathbf{f}(\mathbf{x}_k)\|. \quad (3.68)$$

A well established approach in engineering design is the correction or enhancement of simplified analytical or circuit based models with data obtained from physical experiments or numerical simulations, therefore the main idea of the

technique is not new. Nevertheless, ISM exploits this approach and provides an elegant coherent procedure for engineering optimization.

It can be observed that the implicit mapping proposed by ISM can introduce a transformation similar to an output mapping. The preassigned parameters transform the set $\mathbf{c}(\mathbf{Z})$ into a parametric manifold $\mathbf{c}_\eta(\mathbf{Z})$ and, consequently, the coarse model flexibility is adjusted through ISM with the only limitation being given by the inherent (reduced) complexity of the model. Consequently, a manifold alignment is theoretically possible but generally it cannot be assumed. This discussion can be summarized as: a perfect implicit mapping is expected if there exists $\boldsymbol{\eta}^* \in \mathbb{R}^r$ such that

$$\mathbf{f}(\mathbf{x}^*) = \mathbf{c}(\mathbf{z}^*(\boldsymbol{\eta}^*), \boldsymbol{\eta}^*). \quad (3.69)$$

When (3.69) is not achievable, ISM can be employed together with an explicit output mapping [42, 59].

3.5.7 Output SM interpolating surrogate

The SM interpolating surrogate (SMIS) develops further the concept of the original OSM technique (Section 3.3.2). A new surrogate is explored, which involves both input and output mappings (3.35) and satisfies interpolating conditions, i.e., response match, Jacobian match at the current point and global match at a set of points [49]. The SMIS surrogate is defined as

$$\mathbf{o}(\mathbf{c}(\mathbf{p}(\mathbf{x}))) = \boldsymbol{\alpha}_k(\mathbf{c}(\mathbf{p}(\mathbf{x})) - \mathbf{c}(\mathbf{p}(\mathbf{x}_k))) + \boldsymbol{\beta}_k, \quad (3.70)$$

where the input mapping is

$$\mathbf{p}(\mathbf{x}) = \mathbf{B}_k \mathbf{x} + \mathbf{b}_k \quad (3.71)$$

with $\boldsymbol{\alpha}_k, \boldsymbol{\beta}_k \in \mathbb{R}^m$, $\mathbf{B}_k \in \mathbb{R}^{n \times n}$ and $\mathbf{b}_k \in \mathbb{R}^n$. A surface fitting approach is employed for PE, which involves the minimization of residuals between the surrogate and fine models, and extracting the parameters $\boldsymbol{\alpha}_{k+1}$, \mathbf{B}_{k+1} and \mathbf{b}_{k+1} with $\boldsymbol{\beta}_{k+1} = \mathbf{f}(\mathbf{x}_k)$. The SMIS algorithm delivers the accuracy expected from classical direct optimization using sequential linear programming.

Following a similar idea, an SM interpolation scheme is proposed in [60] to work in conjunction with SM optimization algorithms for cases when the fine model is available only on a structured grid.

3.5.8 Manifold-mapping

The idea of correcting the misalignment between the sets $\mathbf{f}(\mathbf{X})$ and $\mathbf{c}(\mathbf{Z})$ by means of a manifold mapping was introduced in [41] together with a conver-

gence study in [43]. It is assumed here that $\mathbf{Z} \equiv \mathbf{X}$ and input mapping is not considered. An output mapping $\mathbf{s} : \mathbf{c}(\mathbf{X}) \rightarrow \mathbf{f}(\mathbf{X})$, given by

$$\mathbf{s}(\mathbf{c}(\mathbf{x})) = \mathbf{f}(\mathbf{x}^*) + \bar{\mathbf{s}}(\mathbf{c}(\mathbf{x}) - \mathbf{c}(\mathbf{x}^*)) \quad (3.72)$$

with

$$\bar{\mathbf{s}} = \mathbf{J}_f(\mathbf{x}^*)\mathbf{J}_c^{-1}(\mathbf{x}^*), \quad (3.73)$$

is proposed to map the point $\mathbf{c}(\mathbf{z}^*)$ onto $\mathbf{f}(\mathbf{x}^*)$ and the tangent plane for $\mathbf{c}(\mathbf{Z})$ at $\mathbf{c}(\mathbf{z}^*)$ onto the tangent plane for $\mathbf{f}(\mathbf{X})$ at $\mathbf{f}(\mathbf{x}^*)$ (the $(\cdot)^{-1}$ matrix operator represents the pseudo-inverse). The original manifold-mapping (OMM) defines the surrogate as $\mathbf{s}(\mathbf{c}(\mathbf{x}))$ and determines a fine model iteration from:

$$\mathbf{x}_{k+1} = \operatorname{argmin}_{\mathbf{x} \in \mathbf{X}} \|\mathbf{s}_k(\mathbf{c}(\mathbf{x})) - \mathbf{y}\|, \quad (3.74)$$

where \mathbf{s}_k and, consequently, $\bar{\mathbf{s}}_k$ are iterative approximations of \mathbf{s} and $\bar{\mathbf{s}}$, respectively. A more attractive formulation from an implementation point of view is considered with the manifold-mapping (MM) technique where the pseudo-inverse of $\bar{\mathbf{s}}$ is applied to the design specification \mathbf{y} and hence at each iteration step the coarse model is optimized for an updated goal:

$$\mathbf{x}_{k+1} = \operatorname{argmin}_{\mathbf{x} \in \mathbf{X}} \|\mathbf{c}(\mathbf{x}) - \mathbf{y}_{k+1}\|, \quad (3.75)$$

with

$$\mathbf{y}_{k+1} = \mathbf{c}(\mathbf{x}_k) - \bar{\mathbf{s}}_k^{-1}(\mathbf{f}(\mathbf{x}_k) - \mathbf{y}). \quad (3.76)$$

Further, it is shown in [61] that $\bar{\mathbf{s}}_k$ converges to $\mathbf{J}_f(\mathbf{x}^*)\mathbf{J}_c^{-1}(\mathbf{x}^*)$, therefore also a generalized MM (GMM) algorithm is formulated by choosing:

$$\bar{\mathbf{s}}_k = \mathbf{J}_f(\mathbf{x}_k)\mathbf{J}_c^{-1}(\mathbf{x}_k). \quad (3.77)$$

Nonetheless, while \mathbf{J}_c may be available, \mathbf{J}_f would be replaced by an approximation like the Broyden update [53] in most of the cases.

Finally, the addition of a TR strategy leads to the trust-region MM (TRMM) algorithm proposed in [62].

3.6 Convergence of SM algorithms

The SM technique is appealing to the mathematical community for its applicability in different fields. Therefore, mathematicians have started to study

the formulation and convergence issues of SM based algorithms. A mathematical support of SM in the context of classical optimization based on local Taylor approximations is presented in [38]. Convergence studies of SM algorithms originally treated hybrid algorithms where the surrogate model is a convex combination of the mapped coarse model and the linearized fine model are found in [23], [63]. The convergence of a hybrid algorithm, assuming the objective function to be the l_2 norm, is proven in [64] and the case of non-differentiable objective functions is discussed in [63]. However, the convergence theories in these papers rely on the combination with a classical Taylor based method. Therefore, classical principles of convergence proofs are applicable. Unfortunately, it is not possible to prove convergence of true SM algorithms in this way because these algorithms do not necessarily provide local model interpolation at the current iterate [39]. Convergence properties of the OSM algorithm are discussed in [65]. The MM based algorithms are analyzed and their convergence is proven in [43].

3.7 A new algorithm: aggressive output SM

A review of the existing SM-based methods has been given in Section 3.5 and several of the presented algorithmic approaches can be merged into a new procedure that benefits from a simple implementation. The root of the algorithm proposed in this thesis is the OSM technique, however, in the inverse formulation where new design vectors are obtained from

$$\mathbf{x}_{k+1} = \operatorname{argmin}_{\mathbf{x} \in \mathbf{X}} \|\mathbf{c}(\mathbf{x}) - \mathbf{t}_k(\mathbf{y})\|. \quad (3.78)$$

The updated coarse model specifications, $\mathbf{y}_k = \mathbf{t}_k(\mathbf{y})$, are determined from quasi-Newton steps considering a Broyden-type update, similar to ASM, of the output mapping Jacobian. Therefore the algorithm is denoted as aggressive output space-mapping (AOSM).

It is assumed in the following that $\mathbf{Z} \equiv \mathbf{X}$ and an input mapping is not considered. Hence, the response mapping is defined as $\mathbf{t} : \mathbf{f}(\mathbf{X}) \rightarrow \mathbf{c}(\mathbf{X})$ with its linear approximation being given by

$$\mathbf{t}_k(\mathbf{y}) = \mathbf{c}(\mathbf{x}_k) + \mathbf{B}_k(\mathbf{y} - \mathbf{f}(\mathbf{x}_k)) \quad (3.79)$$

where \mathbf{B}_k is the approximate Jacobian of the mapping function \mathbf{t} at the point given by $\mathbf{f}(\mathbf{x}_k)$. The algorithm searches for the fine model minimizer \mathbf{x}^* by iteratively solving (3.78). The core of the AOSM algorithm is structured as follows:

1. Initialize $k = 1$, $\mathbf{B}_1 = \mathbf{I}_{m \times m}$, $\bar{\mathbf{y}}_1 = \mathbf{I}_{m \times 1}$, and ε_{10} and ε_{20} .
2. Compute $\mathbf{x}_k = \operatorname{argmin}_{\mathbf{x} \in \mathbf{X}} \|\mathbf{c}(\mathbf{x}) - \mathbf{y}_k\|$ where \mathbf{y}_k is obtained from the elementwise multiplication $\mathbf{y}_k = \bar{\mathbf{y}}_k \mathbf{y}$.
3. Evaluate $\mathbf{f}(\mathbf{x}_k)$ and the error residuals $\varepsilon_1 = \frac{\|\mathbf{f}(\mathbf{x}_k) - \mathbf{y}\|}{\|\mathbf{y}\|}$ and $\varepsilon_2 = \frac{\|\mathbf{f}(\mathbf{x}_{k-1}) - \mathbf{f}(\mathbf{x}_k)\|}{\|\mathbf{f}(\mathbf{x}_{k-1})\|}$.
4. Stop and set $\mathbf{x}_{aosm}^* = \mathbf{x}_k$ if $\varepsilon_1 \leq \varepsilon_{10}$ and $\varepsilon_2 \leq \varepsilon_{20}$.
5. If $k = 1$ skip this step, otherwise update \mathbf{B}_k :

$$\mathbf{B}_k = \mathbf{B}_{k-1} + \frac{\mathbf{d}_{k-1} - \mathbf{B}_{k-1} \mathbf{h}_{k-1}}{\mathbf{h}_{k-1}^T \mathbf{h}_{k-1}} \mathbf{h}_{k-1}^T$$

with $\mathbf{d}_{k-1} = \bar{\mathbf{c}}(\mathbf{x}_k) - \bar{\mathbf{c}}(\mathbf{x}_{k-1})$ and $\mathbf{h}_{k-1} = \bar{\mathbf{f}}(\mathbf{x}_k) - \bar{\mathbf{f}}(\mathbf{x}_{k-1})$, where $\bar{\mathbf{c}}$ and $\bar{\mathbf{f}}$ are the normalized coarse and fine responses with respect to the specification \mathbf{y} .

6. Set $\bar{\mathbf{y}}_{k+1} = \bar{\mathbf{c}}(\mathbf{x}_k) + \mathbf{B}_k(\bar{\mathbf{y}}_1 - \bar{\mathbf{f}}(\mathbf{x}_k))$, $k = k + 1$ and go to step 2.

The AOSM can be also denoted as *inverse* OSM considering that in the latter algorithm a linear mapping which interpolates at the current point is defined as $\mathbf{o} : \mathbf{c}(\mathbf{X}) \rightarrow \mathbf{f}(\mathbf{X})$, and the same type of mapping is defined in AOSM as $\mathbf{t} : \mathbf{f}(\mathbf{X}) \rightarrow \mathbf{c}(\mathbf{X})$.

Further, from (3.76), (3.77) and (3.79) it can be deduced that AOSM is a special case of GMM. The mapping is calculated in GMM as $\bar{s}_k = \mathbf{J}_f(\mathbf{x}_k) \mathbf{J}_c^{-1}(\mathbf{x}_k)$, whereas AOSM estimates it directly from the available coarse and fine model responses by means of Broyden's formula without explicitly computing \mathbf{J}_f or \mathbf{J}_c , with the resulting \mathbf{B}_k matrix having the following property:

$$\mathbf{B}_k \simeq \mathbf{J}_c(\mathbf{x}_k) \mathbf{J}_f^{-1}(\mathbf{x}_k). \quad (3.80)$$

Generally speaking, (3.80) may also reveal a possible drawback of AOSM: since \mathbf{B}_k is an approximation of \bar{s}_k^{-1} from (3.76), a similar solution accuracy can be expected only if \mathbf{B}_k converges to $\mathbf{J}_c \mathbf{J}_f^{-1}$ when approaching \mathbf{x}^* . The algorithm has been tested in [66] and [67] and is employed in Chapters 4 and 5.

3.8 Numerical examples

The SM technique was introduced and thoroughly validated as an efficient optimization approach in the design field of microwave and radio-frequency devices [38], where also an extended list of references is available in [38]. Giving

its success, the SM application area has extended also to other fields like structural design [50] and vehicle crashworthiness [68]. The first application of SM optimization for electromagnetic systems is found in [24] where ASM is tested on two examples: a C-shaped magnetic circuit and an interior PM machine. Within the research framework of this thesis, SM has been tested on several specific electromagnetic design cases, characterized by different levels of complexity. The performance of the SM-based routines was compared with that of several zero- and first-order standard optimization algorithms in order to emphasize its computational efficiency.

An overview of these electromagnetic design optimization studies is given in Table 3.1. The electromagnetic devices considered are: a simple C-shaped magnetic circuit, an axial-symmetric coreless actuator (CA) that can be considered in applications like valve actuation, a cylindrical and a rectangular voice coil actuator (CVCA, RVCA), found in vibration compensation or lens focusing applications, a tubular PM actuator (TPMA) that is considered in this thesis for automotive electromagnetic active suspension, and a long-stroke constant force actuator (CFA) that can provide constant force independent of the linear displacement for applications like vibration compensation or pick-and-place machines. The complexity of the optimization problems varies from unconstrained (uc) to linearly and nonlinearly constrained (lc, nc) problems, and for the TPMA and CFA cases, coupled (cpl) electromagnetic-thermal design is considered. Several standard optimization routines are chosen for performance comparison: the Nelder-Mead simplex (NMS), the DIRECT algorithm [69], a quasi-Newton method (qN) [70], the penalty method (PeM) [71], and the method of moving asymptotes (MMA) [71]. In some of the cases, the SM solution is only locally validated (lv) by means of a standard algorithm, i.e., the SM solution is given as a starting point. All the obtained results indicate the applicability and efficiency of the SM techniques for the design of electromagnetic devices and support the choice of this optimization approach as a design tool in Chapters 4 and 5 of this thesis.

3.9 SM-based design flow

An analysis and design flow chart build around the SM optimization routine is proposed in this section. Classical electrical machine design is based on well known simplified analytical formulas which include certain empirical correction factors. However, the design of novel electromagnetic devices also requires the development of new models. There are two initial options: the implementation

Table 3.1: Numerical examples.

Alg.	Elmag. device	Probl. type	Comp. with	Ref.
ASM	C-shape	uc	NMS, DIRECT, qN	[70]
	CA	uc	NMS	[72]
		lc	PeM, MMA, NMS, DIRECT, SQP	[70]
	CVCA	lc, nc	SQP (lv)	[73]
TRSSM	CVCA	lc, nc	SQP (lv)	[51]
		lc, nc	MM, SQP	[74]
	RVCA	lc, nc	MM, OPSM	[75]
	TPMA	lc, nc	-	[76, 77]
		lc, nc	MM, OPSM	[75]
OPSM	TPMA	lc, nc	TRSSM, MM	[75]
		lc, nc, cpl	-	[78]
AOSM	TPMA	lc, nc, cpl	MM, OPSM	[66]
	CFA	lc, nc, cpl	-	[67]

of a complex numerical model or of a simplified model which could provide a rather coarse estimation of the performance and characteristics of the concerned device. Examples which emphasize the large discrepancies between these modeling choices can be found in [79] for rotary machines and in [22] for linear machines. A significant effort is typically invested in the generation of analytical or reluctance network model with increased accuracy. Even though this can be, in principle, achieved for a given configuration or a reduced search domain, it is quite difficult to maintain a high accuracy across an extended search space [79].

As already stated in this thesis, SM exploits the advantages both complex and simplified models and combines them into an automated, time-efficient design routine. The principal idea is to concentrate the design and optimization effort onto this simplified model in order to obtain solutions with a reasonable accuracy which can be then further improved by means of accurate numerical analysis, i.e., FE analysis in most cases. Nevertheless, several iterations, implying the modification and re-optimization of the simplified model and the evaluation of the complex numerical model, are necessary. Furthermore, in general, these iterations are not integrated in an automated process. It can be observed that the classical design flow resembles very closely the main idea of the SM optimization. Therefore, it can be stated that SM provides the automation of the classical design process and brings several additional advantages: firstly, a highly accurate analytical or equivalent circuit model is not necessary, and, secondly and most important, the output of the optimization loop is an accurate result guaranteed by the included fine model. As an additional result of this chapter, the SM based design flow chart for electromagnetic actuators shown in Fig. 3.6 is proposed. Besides the main design flow path, several alternative and return paths are indicated. The alternative paths can be considered to skip steps which are not applicable or necessary for a given case. There are two types of return paths, i.e., outside and within the optimization loop. A return path from the preliminary sizing or post-processing step to the qualitative assessment step is necessary if a design solution based on the initial actuator configuration cannot be obtained and therefore an alternative choice must be taken. The return path from the post-processing step to the optimization loop is indicated for cases where the definition of the optimization problem needs to be adjusted in order to improve the convergence rate or to re-direct the routine to a different solution. In some cases, the definition of the coarse and fine models may need adjustment in order to assure the convergence of the SM routine or to improve the obtained solution, hence a return path from the SM optimization routine to the coarse and fine models block is also indicated.

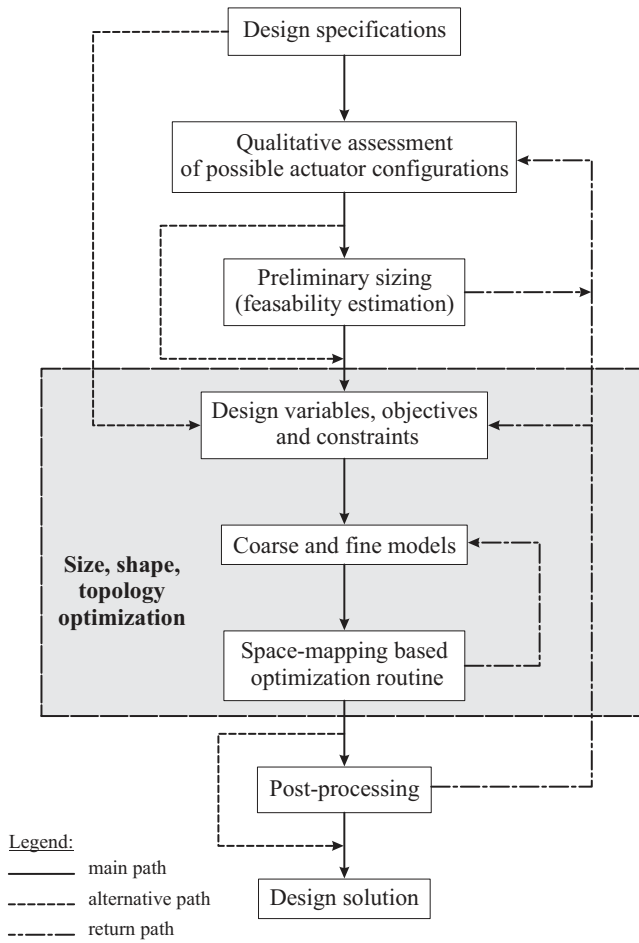


Figure 3.6: Generalized flow-chart of an SM-based analysis and design approach.

3.10 Conclusions and remarks

Fundamental aspects of SM optimization together with an overview of the existing techniques and design examples are presented in this chapter. A new algorithm variant is proposed, i.e., the AOSM which is introduced as an inverse OSM formulation. The numerical examples investigated within the framework of this thesis have illustrate the efficiency of SM optimization when compared with various standard optimization algorithms and support the choice of an SM-based algorithm as a design tool in this thesis. The AOSM is employed in Chapter 4 to determine a series of pre-design solutions for the tubular PM actuator. In Chapter 5 the AOSM is implemented to solve a shape optimization problem for a new actuator topology, where no information is available about the possible solution(s). The obtained result identifies a novel actuator design for active suspension, which is the main contribution of this thesis.

4

Case I: Tubular linear actuator for active suspension

4.1 Introduction

This chapter investigates the first of the two topologies proposed in Section 1.3.2, i.e., a brushless tubular PM actuator, which in an active suspension strut would be implemented in parallel with a mechanical spring as a replacement of the passive damper. The purpose is not to identify a final actuator design, but to indicate that this actuator solution can satisfy the required design specifications and to show how SM optimization can speed-up the exploration and identification of optimal design solutions. Tubular PM actuators are characterized by high force density, especially compared with their linear flat counterparts, reduced losses and power consumption [21]. Detailed design considerations and characteristics of tubular actuators can be found in literature [80, 81]. The fundamental topological characteristics which describe any type of brushless linear PM actuator are:

- stator configuration: slotted or slotless, internal or external, AC or DC excitation;

- translator configuration: PMs with radial, axial or Halbach magnetization patterns;
- number of pole-pairs and phases.
- AC or DC excitation.

Various topological configuration are possible and each of them presents several advantages and disadvantages compared to the other topologies. Therefore, an extended study should include several actuator configurations, however this is out of the scope of this thesis. Considering the high achievable force density and the ease of manufacturing, a tubular actuator having a slotted stator with concentrated windings and full-pitched, radially magnetized translator PMs is chosen in this chapter. An axial cross-section of the corresponding topology is given in Fig. 4.1 and a detailed view of an actuator pole-pair is detailed in the same figure, where the constitutive parts (iron cores, non-magnetic shaft, coils and PMs) are indicated next to the winding arrangement and geometrical parameters. The shown pole-pair is the smallest constitutive part which can be used to predict the behavior of the complete actuator.

Preliminary design considerations for the chosen actuator topology, considering an idealized approach which utilizes the concepts of magnetic and electric loading, are given in Section 4.2. Several pre-design solutions are derived in Section 4.3 by means of size optimization exploiting the AOSM algorithm, where, based on the simplifying assumptions given in Section 2.5, only static magnetic and thermal models are employed in the optimization process. Even though these results can be considered as intermediate steps towards a rigorous design solution, the required calculation time is even more reduced and an overview of different solutions become seamlessly available. As a result of this section, several pre-design configurations that satisfy the considered design requirements can be identified and one of them is chosen for further analysis.

The quasi-rectangular electromotive force (EMF) distribution, associated with the full-pitched PM configuration, indicates that DC current excitation is the proper choice in order to obtain a constant force response. However, if skewing is to be considered, at the cost of a reduced force output, the EMF waveform will tend to a sinusoidal profile and, therefore, AC sinusoidal current excitation may become more adequate. This aspect together with several dynamic effects are discussed in Section 4.4 for the chosen pre-design configuration.

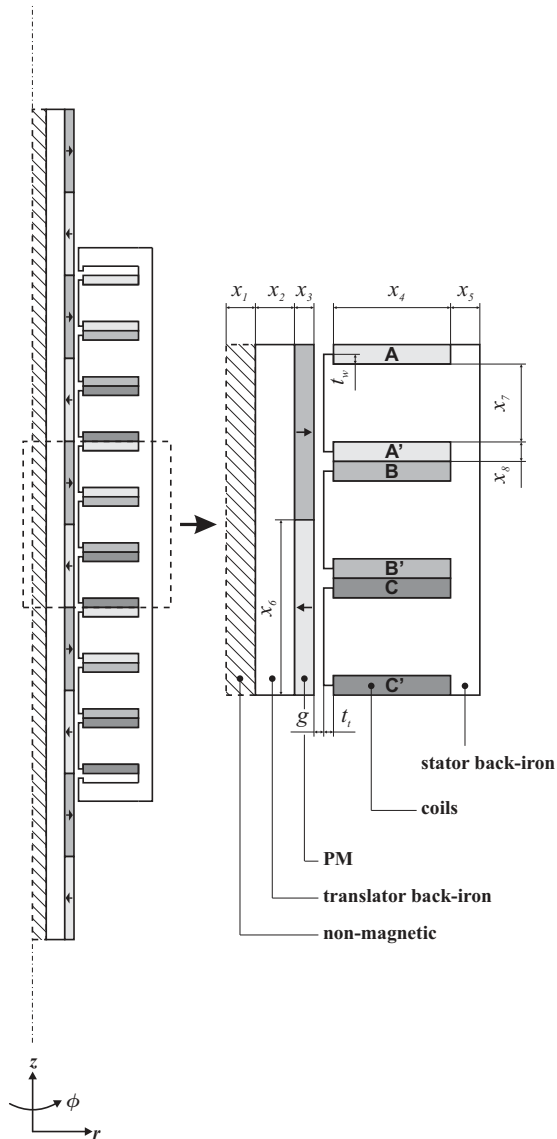


Figure 4.1: The selected slotted, radially magnetized, brushless DC tubular PM actuator topology: a complete view and a detailed view of one pole-pair, where the design variables are indicated.

4.2 Preliminary design considerations

As a first step in the design process, it is possible to determine the main dimensions by means of a simplified or idealized approach. Such an approach is proposed in [82] for rotary machines, and it can be easily adopted for this case with the purpose of estimating the feasibility of a solution considering a linear electromagnetic actuator. In particular, it is important to determine if the specified nominal force (Table 2.8) can be attained within the given volumetric envelope and which values of electric and magnetic loading are required.

The so-called static *output relation* [82] which can be applied to all tubular linear actuators relates the force per translator volume, F_{tv} , to the magnetic loading B and the electric loading Q , where B is the average airgap flux density and Q is defined as the linear current density along the length of the stator (Fig. 4.2), i.e., the number of ampere-conductors per meter in axial direction along the stator surface which faces the airgap (the airgap is assumed to be very small compared to the translator radius, thus no distinction is made between the translator outer radius and the stator inner radius):

$$Q = \frac{\text{Total ampere-conductors}}{\text{airgap axial length}} = \frac{n_z I}{L_{st}}. \quad (4.1)$$

For a tubular actuator, the output relation ratio is given by:

$$F_{tv} = \frac{F}{V_{tr}}, \quad (4.2)$$

and it can be intuitively derived starting from a simplified form of the Lorentz force, i.e.,

$$F = B n_z I 2\pi r_g, \quad (4.3)$$

where n_z is the number of conductors and r_g is the airgap radius, where F , B and I can be the RMS values of force, magnetic flux density and electric current. Alternatively, the force can be expressed as:

$$F = \sigma 2\pi r_g L_{st}, \quad (4.4)$$

where σ is denoted as the *airgap shear stress* (Fig. 4.2), i.e., the axial force per unit stator surface (Fig. 4.2), and it is measured in N/m^2 . Further, from (4.1), (4.3) and (4.4), the output force can be derived in terms of the corresponding densities, i.e.,

$$\sigma = BQ, \quad (4.5)$$

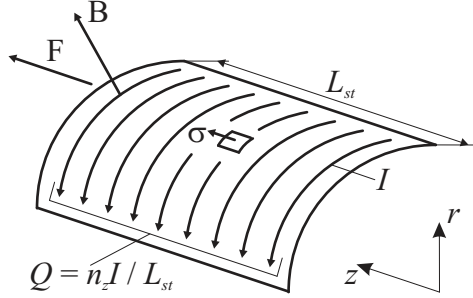


Figure 4.2: The airgap shear stress.

and, with $V_{tr} = \pi r_g^2 L_{st}$ in (4.2), the F_{tv} can be written as:

$$F_{tv} = \frac{2}{r_g} \sigma = \frac{2}{r_g} BQ. \quad (4.6)$$

In the case of rotary machines [82], the output relation refers to the torque per rotor volume and can be simplified to $T_{rv} = 2BQ$. However, for the linear tubular actuator, the force per translator volume, F_{tv} , is also a function of the airgap radius r_g .

These basic equations can be utilized to predict the electric and magnetic loading values which are necessary to provide the require thrust force within the allowed geometrical envelope. For this purpose, a reduced number of design specifications and parameters are selected in Table 4.1 from the extended list of Chapter 2.

From the data given in Table 4.1, it can be determined that for the maximum active volume, $V_s = \pi r_t^2 L_{st} = 0.008646\text{m}^3$, a volume force density of at least 231.33kN/m^3 is necessary for the actuator to provide a mean force of 2kN . The necessary electric loading can be obtained as a function of the mean force, the magnetic loading and the airgap radius by substituting $V_{tr} = \pi r_g^2 L_{st}$ into (4.6) to obtain:

$$Q = \frac{F}{2\pi r_g L_{st} B}, \quad (4.7)$$

where the electric loading is graphically represented in Fig. 4.3 as a function of typical magnetic loading values and airgap radius normalized to the maximum actuator radius. However, this graphical representation does not provide enough information since it cannot show if the respective values of electric loading are

Table 4.1: Design requirements and parameters.

Electromagnetic requirement	
Nominal static force	$F = 2\text{kN}$
Geometric parameters	
Actuator length	$L_a = L_t = 0.6\text{m}$
Actuator outer radius	$r_a = r_t = 0.08\text{m}$
Stroke	$s = 0.17\text{m}$
Stator axial length	$L_{st} = L_t - s = 0.43\text{m}$

achievable. More parameters have to be introduced in order to determine the corresponding coil current densities. A coil filling factor, $k_f = 0.5$, is defined, the coil width, x_8 , is fixed to half the tooth width, x_7 , i.e., $x_8 = 0.5x_7$, and consequently the coil width is given by

$$x_8 = \frac{L_{st}}{12n_{pp}}, \quad (4.8)$$

where n_{pp} is the number of pole-pairs. In addition, the coil height, x_4 , is defined as

$$x_4 = 0.8(r_a - r_g). \quad (4.9)$$

These choices are of course arbitrary and for more insight one should consider the dependency of the current density and other electromagnetic quantities on the variation of these geometrical parameters. However, at this point it suffices to obtain at least one feasible result within the context of such a simplified analysis. Further, a total equivalent current per pole-pair can be determined from

$$I_{n_{pp}}^{eq} = \frac{QL_{st}}{n_{pp}} \quad (4.10)$$

and considering only one turn per coil (choice which does not affect the final result), with two coils per phase, the peak current for a stator-translator alignment as in Fig. 4.1 is given by

$$I_p = \frac{I_{n_{pp}}^{eq}}{4}, \quad (4.11)$$

which is valid for both DC and AC current excitation since in the former case one phase is not excited while the other two are at peak current, i.e., a total

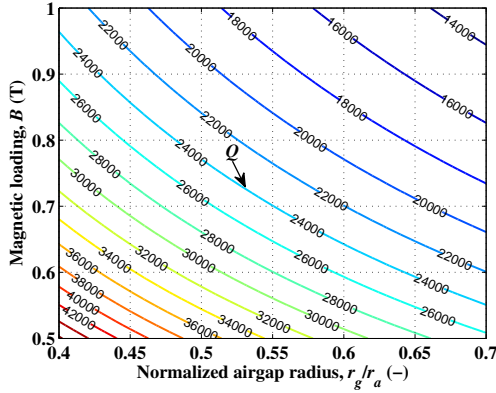


Figure 4.3: Isolines representing the electric loading, Q (A/m), as a function of the magnetic loading, B (T), and the normalized airgap radius, r_g/r_a .

of four coils are at peak current, and in the latter case one phase is at peak current and two phases are at half current which is also equivalent to four coils at peak current. Following from (4.8), (4.9), (4.10) and (4.11), the coil peak current density can be derived as

$$J_p = \frac{I_p}{x_4 x_8 k_f} = \frac{3Q}{0.8(r_a - r_g)k_f}, \quad (4.12)$$

which turns out to be a function independent on the number of pole-pairs, thus no information about the appropriate actuator configuration from this point of view can be extracted. The obtained peak current density is graphically represented in Fig. 4.4 as a function of the magnetic loading and the normalized airgap radius and a first conclusion could be stated at this point: Fig. 4.4 indicates that, for the design specifications from Table 4.1, a feasible design solution may be found within the encircled region defined by $B \in [0.85, 1]$ T and $r_g/r_a \in [0.45, 0.6]$ for a peak current density $J_p \in [3.5, 4]$ A/mm².

The quantities shown in Fig. 4.3 and Fig. 4.4 are functions of the magnetic loading which is calculated under open-circuit conditions. Consequently, it is of interest to estimate the magnet length, x_3 , which would correspond to the chosen range of magnetic loading. This can be achieved with the help of a simplified MEC model for a single pole-pair, derived based on the fundamental relations given in [83], where the translator back-iron and stator teeth and back-

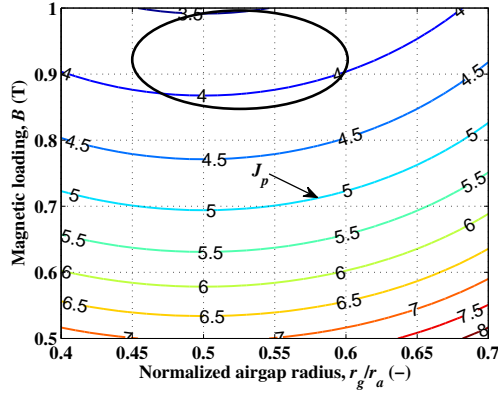


Figure 4.4: Isolines representing the peak current density, J_p (A/mm^2), as a function of the magnetic loading, B (T), and the normalized airgap radius, r_g/r_a .

iron are included as linear ferromagnetic materials. As shown in Fig. 4.5, only one main flux path which closes through the exterior stator teeth is considered. For the open-circuit case, the only flux passing through the middle stator tooth is the PM leakage flux which closes through the tooth tip, where this flux path is disregarded. Thus, the airgap magnetic flux density or magnetic loading can be expressed as a function of the reluctances corresponding to the translator back-iron, magnets, airgap, stator teeth and back-iron:

$$B = \frac{2f_m}{S_g (\mathcal{R}_1 + 2\mathcal{R}_2 + 2\mathcal{R}_3 + 2\mathcal{R}_4 + \mathcal{R}_5)}, \quad (4.13)$$

where the material properties are indicated in Table 4.2 the expressions of the reluctance elements and the MMF source are given in Appendix B.1. For this simple model, an airgap length, g , of 0.001m is considered and the translator shaft and the teeth pole-shoes are disregarded. The magnetic loading can be now graphically represented as in Fig. 4.6, from where it can be concluded that any magnet length in the interval $[0.003; 0.020]$ m could provide the necessary airgap magnetic flux. However, the magnet length is not determined only by the specified magnetic loading but also by its demagnetization withstand capability. A shorter magnet, i.e., in the direction of magnetization, although reducing the material costs, would also be relatively easily demagnetized. On the contrary,

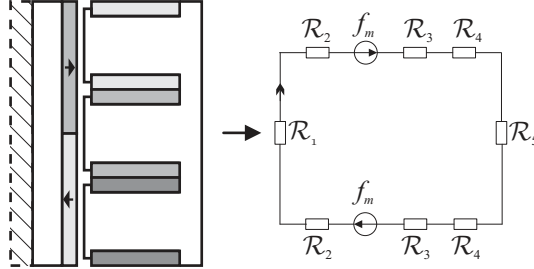
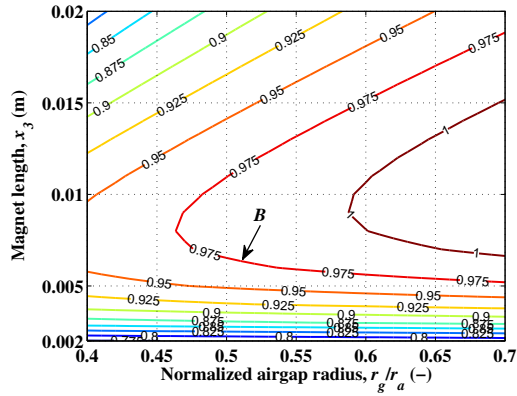


Figure 4.5: Simplified MEC model for the actuator pole-pair shown in Fig. 4.1 of the tubular actuator.

a long magnet would have good demagnetization withstand characteristics but it may also cause an increase in cogging force. Ideally, a magnet should be designed to have a working point at its maximum energy product, thus a minimum material volume would be used, however this principle is not straightforward applicable in electrical machine design due to the fact that the primary windings can generate very strong demagnetizing electromagnetic fields under fault conditions. Therefore, the magnets should be designed to work at high permeance coefficients in open-circuit conditions in order to preserve enough coercive force to resist the maximum demagnetizing fields. Further information could be extracted from this simple model, i.e., the magnitude of the magnetic flux density in the magnets and the iron core can be calculated, thus obtaining initial estimates for the magnets' working point and the possible magnetic saturation of the iron core. Therefore, having calculated the airgap flux density, the main magnetic flux, Φ_m , can be determined and with the cross-section expressions, given as denominators of the reluctance elements in Appendix B.1, the magnet and iron flux densities are obtained. The results are presented in Figs. 4.7-4.10 as follows: magnets, stator teeth, stator back-iron and translator back-iron, respectively. These figures indicate that, as expected, a compromise has to be made since a longer magnet provides a higher permeance coefficient (the magnet flux density approaches the value of the remanent flux), nevertheless this causes an increase in iron flux-density which would lead to saturation. The latter effect would be also caused by a larger airgap radius. Actually, these results confirm the previous conclusion that a feasible design solution may be found in the region defined by $r_g/r_t \in [0.45, 0.6]$, and in addition they indicate that the magnet length should not be larger than 0.010m.

Table 4.2: Material properties and design parameters.

Material properties	
PM recoil permeability	$\mu_{rc} = 1$
PM remanent flux density	$B_r = 1.23\text{T}$
Iron relative permeability	$\mu_r = 1000$
Other parameters	
Airgap length	$g = 0.001\text{m}$

Figure 4.6: Isolines representing the magnetic loading, B (T), as a function of the magnet length, x_3 (m), and the normalized airgap radius, r_g/r_a .

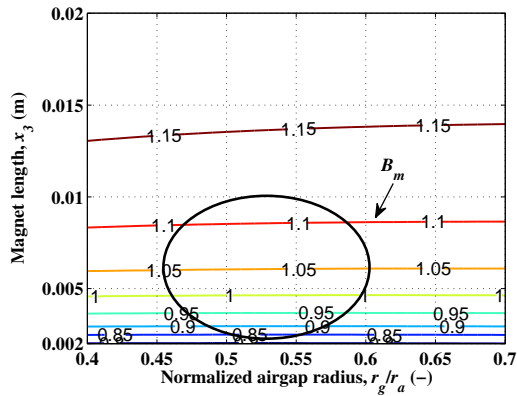


Figure 4.7: Isolines representing the PM flux density, B_m (T), as a function of the magnet length, x_3 (m), and the normalized airgap radius, r_g/r_a .

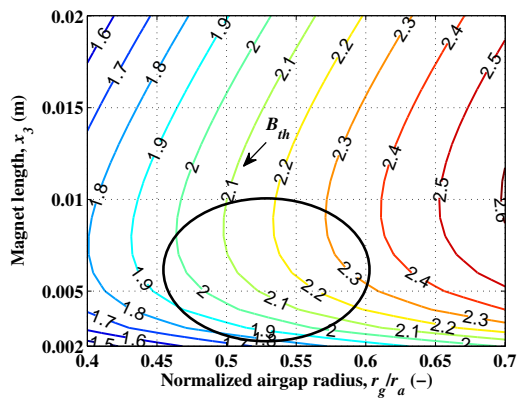


Figure 4.8: Isolines representing the stator tooth flux density, B_{th} (T), as a function of the magnet length, x_3 (m), and the normalized airgap radius, r_g/r_a .

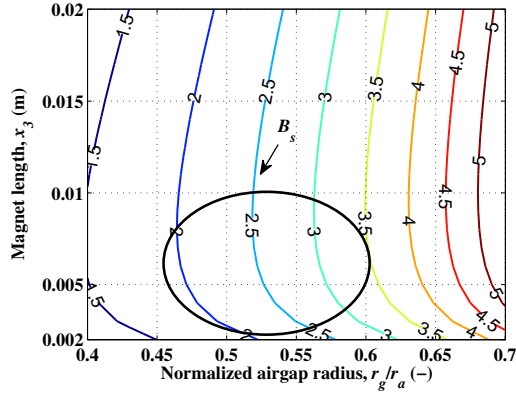


Figure 4.9: Isolines representing the stator back-iron flux density, B_s (T), as a function of the magnet length, x_3 (m), and the normalized airgap radius, r_g/r_a .

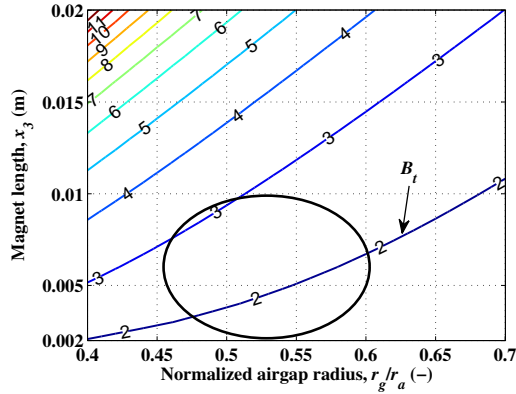


Figure 4.10: Isolines representing the translator back-iron flux density, B_t (T), as a function of the magnet length, x_3 (m), and the normalized airgap radius, r_g/r_a .

Considering that the material nonlinearities are disregarded, the flux distribution is greatly simplified, the slot, tooth and back-iron dimensions are arbitrarily defined, the eddy currents effects and thermal phenomena have not been included, it is expected for the results of a detailed analysis to have deviations, maybe significant in some cases, however the above analysis provides a fast estimation for the applicability of the chosen solution. The results suggest that current density values which are typical for standard electrical machines, i.e., $J_p \in [3.5, 4]\text{A/mm}^2$, can provide the required nominal mean force within the specified geometrical constraints. Furthermore, the values for the normalized airgap radius are in agreement with published results [81] where, following a more detailed analysis, it is shown that a maximum force density for a tubular slotted machine it is expected for an airgap to total radius ratio in the 0.5 – 0.6 range.

The calculation of the actuator sizes is undertaken in the following section, where also the influence of the number of pole-pairs on the resulting outer dimensions is studied in correlation with the geometric, electromagnetic and thermal design requirements.

4.3 AOSM size optimization of the tubular actuator

In contrast to the previous section, accurate modeling of the electromagnetic and thermal phenomena is considered in this section in order to determine the actuator sizes. Given the complex and nonlinear nature of these phenomena, a direct determination of the design variables is not possible if either analytical or numerical models are considered. Therefore, as specified in Chapter 1, optimization is chosen as a design tool. Namely, the AOSM routine, introduced in Section 3.7, is employed to solve a series of size optimization problems which are differentiated by the imposed number pole-pairs.

4.3.1 Design specifications and problem formulation

The main objective of these optimization problems is the minimization of the actuator mass with respect to a number of constraints imposed on the outer dimensions, the force output, the magnetic saturation of the iron parts and the maximum temperature level. Several design assumptions, regarding the requirements on the force response and thermal behaviour, have been introduced in Section 2.4 and are restated here:

- a nominal actuator force of 2kN, with a peak of 4kN (Table 2.8), is suffi-

Table 4.3: Design requirements.

Electromagnetic	
Nominal static force	$F_n = F_0 = 2\text{kN}$
Flux density	$B_i^{avg} \leq B_0 \in \{1.0, 1.3, 1.6\}\text{T}$
Thermal	
Maximum temperature	$T_p \leq T_0 = 130^\circ\text{C}$
Geometric	
Stator axial length	$L_{st} \leq l_t - s = 0.43\text{m}$
Actuator outer radius	$r_a \leq r_t = 0.08\text{m}$
Design domain	$x_{low} = 0.002\text{m}, x_{up} = 0.200\text{m}$

cient to cover both typical anti-roll and damping requirements;

- natural cooling and an ambient temperature of 25°C for nominal thrust force are defined as design parameters;
- static electromagnetic and thermal models are considered to be sufficient to predict an optimum design solution.

The considered design requirements which are subsequently transformed into the optimization constraints and objective are listed in Table 4.3. Two of the constraints given in Table 4.3 are formulated and implemented in a relaxed form which decreases the difficulty of the problem without affecting the result. Firstly, the specification on the output force design is relaxed from an equality constraint to the inequality constraint:

$$F_n(\mathbf{x}) \geq F_0 \quad (4.14)$$

based on the fact that the mass minimization for an electromagnetic actuator leads, in a limit sense, to the decrease of its force output, i.e., $\lim_{M_t \rightarrow 0} F_n = 0$. In other words, it is expected for the constraint from (4.14) to become active as a result of the mass minimization and thus the respective specification to be satisfied. The benefit of this formulation is the elimination of an equality constraint which typically is more difficult to solve [32]. Secondly, the upper limit on the outer radius is eliminated and the actuator radius is added to the main objective with a large associated weighting factor. These two objectives are

not conflicting, thus the problem does not become a multi-objective one. This choice is determined by the following reasons: (1) a rather high force density for a naturally cooled actuator is required, therefore hard limits on the space-envelope are expected to play a critical role in the feasibility of the optimal solution, and (2) the limit imposed on the axial length is strict, however the radial limit may allow for some tolerance because of the usually available space around the suspension strut in a typical car. Therefore, this upper constraint is transformed into a component of the objective function and, consequently, the problem's objective becomes the minimization of the total actuator mass and its outer-radius, with an emphasis on the latter one by means of a large associated weighting factor:

$$\mathcal{F}(\mathbf{x}) = M_t(\mathbf{x}) + wr_a(\mathbf{x}). \quad (4.15)$$

It can be arguably stated that the inclusion of the mass in the objective function becomes somehow redundant, since the actuator mass is proportional to the square of the outer radius, however the minimization of the radius leads to the reduction of the total volume which does not imply the minimization of the total mass because the involved materials are characterized by different mass densities.

The number of design variables, x_i , is reduced from eight, shown in Fig. 4.1, to seven because only two out of three dimensional variables in the axial direction are independent, thus the coil width, x_8 , can be expressed as a function of the magnet and slot width:

$$x_8 = \frac{1}{3}x_6 - \frac{1}{2}x_7. \quad (4.16)$$

Furthermore, the stator axial length, L_{st} , is defined by the summation of the lengths of the pole-pairs and the stator-ends (Fig. 4.1), where the length of a stator-end is defined as

$$L_{se} = \frac{1}{2}x_7 + x_8, \quad (4.17)$$

and, by including (4.16), the stator length becomes

$$L_{st} = 2(n_{pp} + \frac{1}{3})x_6. \quad (4.18)$$

Consequently, with the objective function defined by (4.15), the optimization problem is formulated as follows

$$\begin{aligned} & \text{minimize} && \mathcal{F}(\mathbf{x}), \mathbf{x} \in \mathbf{X} \subseteq \mathbb{R}^7, \\ & \text{subject to} && g_i(\mathbf{x}) \leq 0, i = 1, \dots, 4, \\ & && \mathbf{A} \cdot \mathbf{x} \leq \mathbf{b}, \end{aligned} \quad (4.19)$$

where the design domain is

$$\mathbf{X} = \{\mathbf{x} \mid x_{low} \leq x_i \leq x_{up}\}, \quad (4.20)$$

the nonlinear constraints are

$$g_i = \begin{cases} B_i^{avg} - B_0, & i = \{1, 2, 3\} \\ F_0 - F_n, & i = 4 \\ T_p - T_0, & i = 5 \end{cases} \quad (4.21)$$

and the linear constraints are determined by

$$A = \begin{pmatrix} 0 & 0 & 0 & 0 & 0 & 2n_{pp} + \frac{1}{3} & 0 \\ 0 & 0 & 0 & 0 & 0 & -\frac{1}{3} & \frac{1}{2} \end{pmatrix}, \quad (4.22)$$

and

$$b = \begin{pmatrix} l_t - s \\ -x_{low} \end{pmatrix}. \quad (4.23)$$

The average flux densities, B_i^{avg} , are estimated in the translator back-iron and the stator upper tooth and back-iron. The manner in which these values in addition to the force and peak temperature are calculated is specified in the following section where the respective coarse and fine models are presented. The material properties and other design parameters that are considered for the implementation of the models are given in Table 4.4.

4.3.2 Coarse and fine models

As presented in Chapter 3, any SM based technique requires (at least) two models of the studied physical device or phenomenon: a fine model which assures the accuracy of the solution and a coarse model which forms the base for a fast surrogate. The coarse and fine models chosen here are a MEC model and an FE model, respectively. Both are static models for which a fixed translator-stator relative position as in Fig. 4.1 is chosen based on the fact that this theoretically

Table 4.4: Material properties and design parameters.

Material properties	
PM mass density	$\rho_m = 7700\text{kg/m}^3$
Copper mass density	$\rho_{Cu} = 8900\text{kg/m}^3$
Iron mass density	$\rho_{Fe} = 7650\text{kg/m}^3$
Other parameters	
Peak current density	$J_p = 5\text{A/mm}^2$
Coil filling factor	$k_f = 0.5$
Airgap length	$g = 0.001\text{m}$
Tooth-tip parameters	$t_t = 2g, t_w = 0.7x_s$
Heat convection coefficient	$h_c = 30\text{W}/(\text{m}^2\text{K})$
Ambient temperature	$T_a = 25^\circ\text{C}$

corresponds to the position of zero cogging force and thus the mean output force of the actuator can be accurately predicted. Furthermore, the temperature level can be predicted with satisfactory accuracy by analytical means, i.e., especially for a fixed displacement, thus an FE thermal model is not considered in the optimization. Thermal FE analysis is carried out for the chosen solution in Section 4.4.

Coarse model

The coarse model is an extended version of the MEC model introduced in Section 4.2. This model is used to calculate the approximate flux densities for both open-circuit and nominal load conditions, therefore it includes the winding excitation and additional magnetic flux paths. The model is still restricted to a pole-pair since this proves to be sufficient, however it needs mentioning that the magnetic flux tube which occurs between adjacent pole-pairs is disregarded, still this does not impede the success of the solution. The resulting MEC model is presented next to the geometry of a pole-pair in Fig. 4.11. The following simplifying assumptions are included: the iron core and PM materials are considered linear, with a relative magnetic permeability and a relative recoil permeability as indicated in Table 4.4, and the magnetic fringing effects are neglected. Nonetheless, the slot leakage and magnet leakage fluxes are modeled in simple

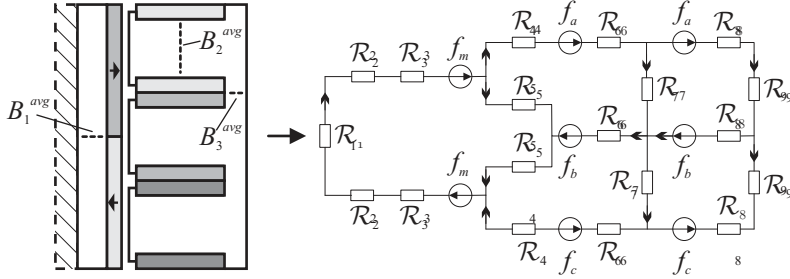


Figure 4.11: Extended MEC model for one pole-pair (the three cross-sections where the flux density values are calculated during the optimization are indicated in the left figure).

manner. Similarly to the theory of electric circuits, a system of linear equations,

$$\mathbf{R} \cdot \Phi = \mathbf{f}, \quad (4.24)$$

is derived from Kirchhoff's laws. The system matrix, source vector and the expressions of the reluctance elements and MMF sources, as functions of the design variables, are given in Appendix B.2. It must be mentioned that sinusoidal excitation is considered, therefore all three phases are conducting and a peak MMF for phase B corresponds to the specified translator position. The vector of magnetic fluxes, Φ , is determined as the solution of the system (4.24). Hence, the values of flux densities within the defined magnetic paths can be determined and the static force and peak temperature can also be calculated. Firstly, the iron flux densities in the translator back-iron, stator upper tooth and back-iron are obtained by dividing the value of the magnetic fluxes which are passing through the reluctance elements \mathcal{R}_1 , \mathcal{R}_4 and \mathcal{R}_7 to their respective cross-sections. Secondly, the force is approximated by

$$F = n_{pp} B_g N i L_g, \quad (4.25)$$

where B_g is the airgap flux density calculated in open-circuit, Ni represent the total number of Amperé-turns, which equals two times the total excitation MMF, and $L_g = 2\pi(x_1 + x_2 + x_3 + 0.5g)$ is the airgap circumference. Finally, it is assumed that at steady state the temperature is evenly distributed within the volume of the actuator and heat flow occurs only through the outer surface of the stator by means of thermal convection (the entire surface of the stator is

considered, not only one pole-pair). Therefore, the surface temperature is equal to the peak temperature and it can be calculated with [82]

$$T_p = \frac{P_{Cu}}{h_c S_a} + T_a, \quad (4.26)$$

where P_{Cu} is the total copper loss, S_a is the outer stator surface, h_c is the convection coefficient and T_a represents the ambient temperature. For a better approximation, the total copper loss is calculated with the value of the copper resistivity that corresponds to a temperature of 130°C.

Fine model

Given the actuator's axial-symmetry, a simplified FE representation is possible, hence a magnetostatic, axial-symmetric, nonlinear FE model is implemented for each actuator configuration (dependent on the number of stator pole-pairs) using the MAXWELL 2D software package [84]. Fundamental elements of the FE analysis method can be found in [85, 86]. A magnetic vector potential formulation

$$\nabla \times \left(\frac{1}{\mu_0 \mu_r} (\nabla \times A_\varphi(r, z)) \right) = J_\varphi(r, z), \quad (4.27)$$

is implemented on second order, adaptively refined elements, where the mesh density varies between 15000 and 20000 triangular elements for a typical solution.

As previously mentioned, a thermal FE model is not considered at this stage, consequently a misalignment between the coarse and the fine model appears only in terms of the magnetic flux density and force value and hence mappings are defined only for the first four nonlinear constraints from (4.21). The flux densities, B_i^{avg} , are calculated as the average magnitude along the three lines indicated in Fig. 4.11 which cross the translator back-iron and the stator upper tooth and back-iron, respectively. The next sections details the results obtained with the AOSM technique for several actuator configurations.

4.3.3 Comparison of obtained results

A number of fifteen optimization problems are solved, where each problem is identified by the number of imposed number of stator pole-pairs and the constraint imposed on the average iron flux densities, i.e., $n_{pp} \in \{4, 5, 6, 7, 8\}$ and $B_0 \in \{1.0, 1.3, 1.6\}$ T. The same coarse model is employed for all the studied cases, whilst different fine models have to be defined for each n_{pp} configuration. The

results obtained for design specifications given in Section 4.3.1 are presented in Tables 4.5, 4.6 and 4.7. The values for the force density and specific force are calculated based on the active cylindrical volume and active mass (not indicated in the tables), i.e., the volume and mass determined by the stator length. For a clear comparison, the force density, actuator outer radius, normalized airgap radius, magnet length, translator and total actuator mass for all fifteen problems are shown in Figs. 4.12, 4.13, 4.14, 4.15, 4.16 and 4.17, respectively. A notation convention is introduced here for a seamless discussion of the results: each design will be identified hereafter by the pair $\{n_{pp}, B_0\}$.

All results obtained for $B_0 = 1.6\text{T}$ and the results obtained for the higher pole-pair number configurations, i.e., $n_{pp} \in \{6, 7, 8\}$, and $B_0 = 1.3\text{T}$ satisfy the outer radius constraint, $r_a \leq 80\text{mm}$, (Fig. 4.13). Moreover, the first set of designs is characterized by values of the normalized airgap radius in the interval $[0.45, 0.6]$, as predicted in Section 4.2, while from the second set only the low pole-pair number designs have this property. Nevertheless, the magnet length, x_3 , has values lower than 10mm for all fifteen solutions.

It is visible from Fig. 4.12 that the design $\{6, 1.6\}$ offers the highest force density and hence the lowest active volume. The design $\{7, 1.6\}$ presents the lowest total mass, still the difference between these two solutions in terms of mass is less than 1kg, therefore negligible. Concerning the translator mass, which adds to the unsprung mass, the design $\{6, 1.6\}$ is not characterized by the lowest value. The configurations with higher number of pole-pairs present a lower translator mass. However, this cannot be stated as a conclusion since the minimization of solely the translator mass was not the objective of the optimization.

The copper loss, P_{Cu} , for the given translator-stator relative position and the required output force, is also indicated in the respective tables. The values range from 450W to 560W and they are used as input in (4.26) to calculate the peak temperature for the coarse model. It can be observed that the temperature constraint does not become active for any of the optimization solutions and, as expected, the designs with a lower outer radius are characterized by a higher temperature due to the smaller outer surface available for heat removal.

The numerical or computational result that has to be mentioned is given by the number of performed AOSM iterations. Namely, all solutions are obtained within ten algorithm iterations, which implies that a reduced number of FE simulations, i.e., one FE solution per algorithm iteration, are necessary to obtain the solutions presented in Tables 4.5, 4.6 and 4.7. Therefore, considering that the time required for the evaluation and optimization of the coarse model is negligible, the total computational effort for fifteen solutions is small.

Table 4.5: AOSM results obtained for 4, 5, 6, 7, 8 pole-pairs and the design constraint $B_0 = 1.0\text{T}$.

$B_0 = 1.0\text{T}$					
n_{pp}	4	5	6	7	8
$x_1(\text{mm})$	2.00	2.00	2.00	2.00	2.00
$x_2(\text{mm})$	40.75	34.54	30.38	27.64	25.47
$x_3(\text{mm})$	2.89	3.41	4.03	4.69	5.51
$x_4(\text{mm})$	47.87	47.31	48.58	50.03	51.66
$x_5(\text{mm})$	7.36	5.66	4.75	4.22	3.90
$x_6(\text{mm})$	49.62	40.31	33.95	29.32	25.80
$x_7(\text{mm})$	20.54	15.99	13.30	11.43	10.07
$x_8(\text{mm})$	6.26	5.44	4.67	4.59	3.56
$L_{st}(\text{mm})$	43.00	43.00	43.00	43.00	43.00
$r_a(\text{mm})$	103.9	95.92	92.74	91.58	91.54
r_g/r_a	0.444	0.422	0.398	0.380	0.365
Force density(kN/m^3)	137.2	151.5	163.5	168.8	169.9
Specific force(N/kg)	20.93	24.85	26.70	27.45	27.49
$P_{Cu}(\text{W})$	488.3	480.8	485.8	497.0	510.5
$T_p(^{\circ}\text{C})(\text{coarse model})$	80.68	84.17	86.39	88.16	89.46
Translator mass(kg)	28.36	21.95	18.36	16.42	15.21
Total mass(kg)	104.0	87.02	80.29	77.66	77.21
Iterations	8	8	7	8	8

Table 4.6: AOSM results obtained for 4, 5, 6, 7, 8 pole-pairs and the design constraint $B_0 = 1.3T$.

$B_0 = 1.3T$					
n_{pp}	4	5	6	7	8
x_1 (mm)	2.00	2.00	2.00	2.00	2.00
x_2 (mm)	36.22	31.53	28.11	25.42	23.36
x_3 (mm)	4.09	4.62	5.15	6.04	6.99
x_4 (mm)	36.09	36.80	37.37	38.49	39.66
x_5 (mm)	5.10	4.15	3.46	2.97	2.63
x_6 (mm)	49.62	40.31	33.95	29.32	25.80
x_7 (mm)	14.88	11.94	9.99	8.52	7.43
x_8 (mm)	9.10	7.47	6.32	5.51	4.89
L_{st} (mm)	43.00	43.00	43.00	43.00	43.00
r_a (mm)	86.50	82.10	79.09	77.91	77.65
r_g/r_a	0.494	0.470	0.452	0.436	0.423
Force density(kN/m ³)	183.9	206.8	225.6	233.8	236.4
Specific force(N/kg)	32.31	36.04	39.09	40.46	40.85
P_{Cu} (W)	466.8	458.8	452.5	464.0	480.0
T_p (°C)(coarse model)	91.42	93.08	94.21	96.53	98.78
Translator mass(kg)	24.36	20.02	17.22	15.58	14.65
Total mass(kg)	69.26	61.48	56.40	54.11	53.29
Iterations	9	8	10	7	7

Table 4.7: AOSM results obtained for 4, 5, 6, 7, 8 pole-pairs and the design constraint $B_0 = 1.6\text{T}$.

$B_0 = 1.6\text{T}$					
n_{pp}	4	5	6	7	8
$x_1(\text{mm})$	2.00	2.00	2.00	6.47	13.67
$x_2(\text{mm})$	32.34	28.86	25.94	20.38	15.50
$x_3(\text{mm})$	5.33	6.07	7.14	8.01	8.32
$x_4(\text{mm})$	32.86	34.19	35.67	37.20	35.84
$x_5(\text{mm})$	3.90	3.17	2.58	2.16	2.00
$x_6(\text{mm})$	49.62	40.31	33.95	29.32	25.80
$x_7(\text{mm})$	10.62	8.68	7.17	6.02	5.49
$x_8(\text{mm})$	11.23	9.09	7.73	6.76	5.85
$L_{st}(\text{mm})$	43.00	43.00	43.00	43.00	43.00
$r_a(\text{mm})$	79.43	77.29	76.34	77.20	78.34
r_g/r_a	0.506	0.484	0.466	0.457	0.485
Force density(kN/m^3)	234.8	247.7	253.8	248.0	241.6
Specific force(N/kg)	40.58	42.92	44.29	43.88	43.44
$P_{Cu}(\text{W})$	489.2	497.3	518.8	557.2	549.9
$T_p(^{\circ}\text{C})(\text{coarse model})$	101.8	104.2	107.8	112.1	109.5
Translator mass(kg)	21.43	21.12	18.06	16.56	16.67
Total mass(kg)	55.74	54.49	51.13	50.46	50.65
Iterations	9	8	8	8	9

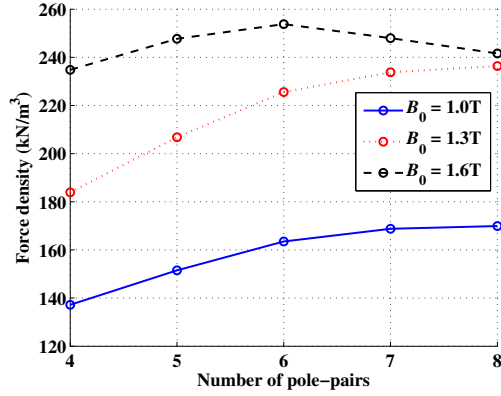


Figure 4.12: Force density as a function of the number of pole-pairs and the imposed B_0 constraints.

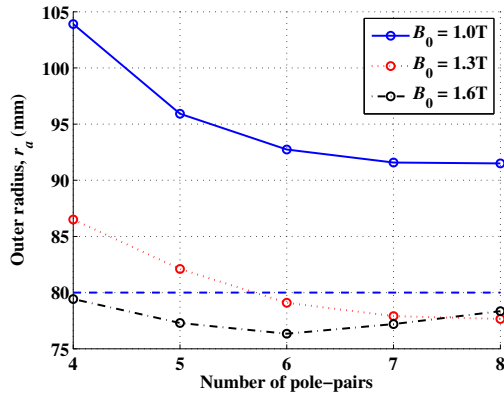


Figure 4.13: Actuator outer radius, r_a (mm), as a function of the number of pole-pairs and the imposed B_0 constraint.

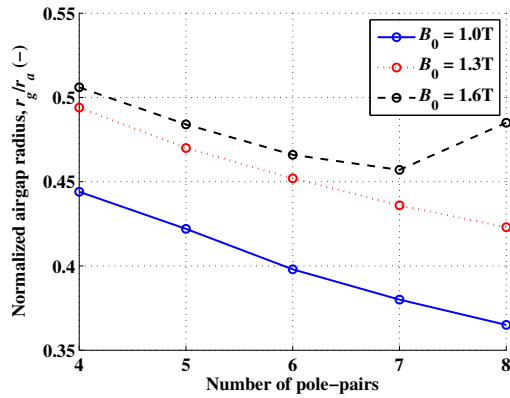


Figure 4.14: Normalized airgap radius, r_g/r_a , as a function of the number of pole-pairs and the imposed B_0 constraint.

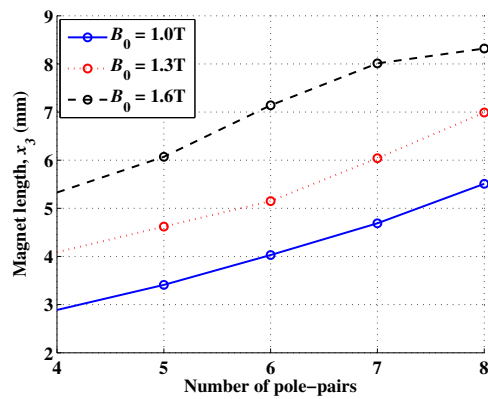


Figure 4.15: PM length, x_3 (mm), as a function of the number of pole-pairs and the imposed B_0 constraint.

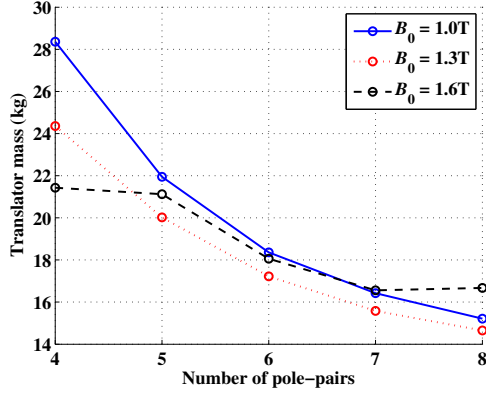


Figure 4.16: Translator mass as a function of the number of pole-pairs and the imposed B_0 constraint.

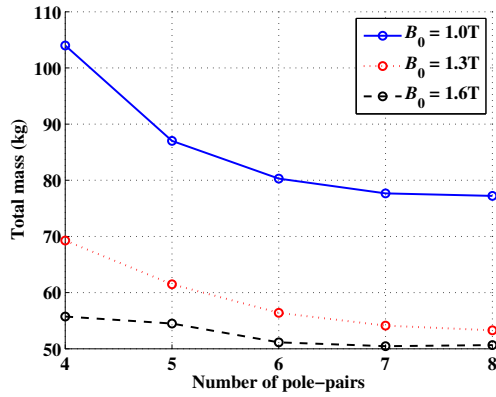


Figure 4.17: Total actuator mass as a function of the number of pole-pairs and the imposed B_0 constraint.

The design with the highest force density, i.e., $\{6, 1.6\}$, is chosen for further analysis. Characteristics like the associated cogging force, the static force versus displacement output, the static temperature distribution and transient behavior are investigated in Section 4.4.

4.4 Solution post-processing

The actuator solution with six stator pole-pairs obtained for $B_0 = 1.6\text{T}$ is analyzed in this section. Firstly, the static force versus displacement responses and the eddy-current damping are analyzed. Secondly, the minimization of the cogging force by means of translator skewing and its effects on the back-EMF are discussed, and thirdly, the temperature rise and distribution are estimated by means of FE analysis.

4.4.1 Force response

The total force output in an electromagnetic actuator can be divided into three components:

- the main component is the mutual alignment force which is given by the interaction between the magnetic field associated with the translator magnets and the stator currents;
- the reluctance component is due to winding self-inductance variations which are a function of the translator position; this force component generates so-called preferred translator-stator relative positions which correspond to the positions of maximum coil inductance;
- the cogging component appears due to the interaction between the translator magnets and the slotted stator structure, i.e., the attraction of the permanent magnets to the salient portions of the stator iron; it also introduces preferred translator-stator alignment positions which correspond to the positions of minimum magnetic reluctance.

In most actuator types the reluctance and cogging forces are unwanted effects since they produce force ripples which, if not eliminated through design, need to be compensated by means of the control strategy. Nonetheless, in the case of the switched reluctance machines or any short-stroke reluctance actuator, the reluctance force represents the principle of operation. The same applies for the cogging force, i.e., it is generally an undesired phenomenon in the long-stroke

machines but it can be a very important force component in various short-stroke actuators (Chapter 5). These two force components are very similar in nature since, in the calculation of the reluctance force, the positions of maximum coil inductance correspond to the positions of minimum magnetic reluctance, and hence the name of this force component. Furthermore, if the magnets would be replaced by equivalent coils, the cogging force would be then calculated as a reluctance force.

The cogging force is calculated for a translator displacement equal to one pole-pair length, i.e., 360 electrical degrees, considering the FE model employed as a fine model in the previous section, with no stator excitation. Using the same static model with a position dependent sinusoidal excitation, the total actuator static force is calculated. The obtained results are shown in Figs. 4.18 and 4.19, respectively. As mentioned above, for both linear and rotary actuators the cogging force is caused by the interaction of the translator magnets with the slotted stator. However, due to the finite stator length of a tubular actuator, a second source of cogging force appears, i.e., the interaction between the field of the permanent magnets and the stator-ends. The sum of these two components is shown in Fig. 4.18. If the total cogging is subtracted from the total output force, the mutual alignment force is obtained (Fig. 4.19). The mean value of the total force has a value of 2260N, i.e., 11.5% higher than the given design specification, $F_0 = 2000\text{N}$. Nevertheless, the design specification is satisfied for the initial position which is considered in the definition of the optimization problems. The peak cogging force 445N represents almost 20% of the mean output force and, therefore, it introduces very high ripples. As it can be seen in Fig. 4.19, the mutual force component is itself characterized by high ripples with maximum values of 350N, i.e., 15.5% of the mean value.

Force ripples are present in any long-stroke electromagnetic actuator. They represent a disturbance on the system in which the actuator is integrated and an environmental noise pollution due to the associated vibrations. Ideally, they can be eliminated through design and control strategy, however, in practice, these effects are only minimized to an acceptable level.

The cause of the high cogging force is the magnet length, x_3 , which is, for example, almost double compared to the magnet length obtained for the actuator configuration $\{6, 1.0\}$. In order to illustrate this, the actuator solution $\{6, 1.0\}$ is analyzed. The cogging force response for the design $\{6, 1.0\}$, given in Fig. 4.22, has an amplitude of less than half of the value obtained for the $\{6, 1.6\}$ configuration. Furthermore, for comparison, the flux density distribution for the actuator solutions $\{6, 1.0\}$ and $\{6, 1.6\}$ is given in Figs. 4.20 and 4.21, respectively. Consequently, it can be concluded that the design $\{6, 1.0\}$

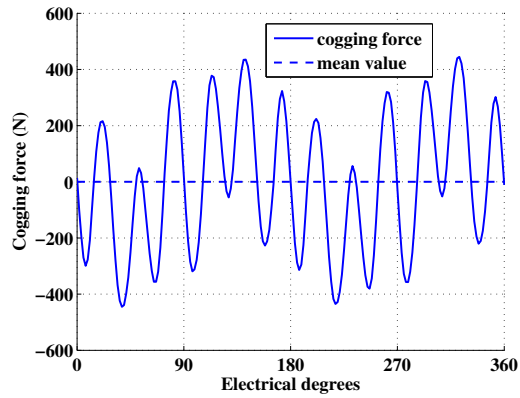


Figure 4.18: Cogging force for the actuator configuration $\{6, 1.6\}$.

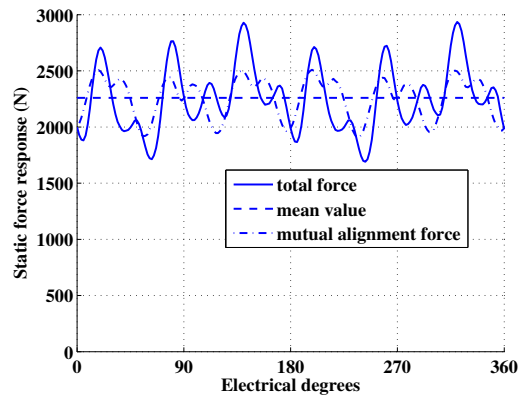


Figure 4.19: Static force response for the actuator configuration $\{6, 1.6\}$, where the mutual alignment force is obtained by subtracting the cogging force, shown in Fig. 4.18, from the total force response.

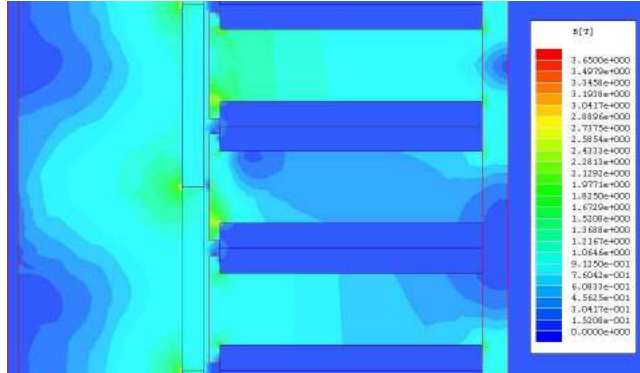


Figure 4.20: Flux density distribution for the actuator configuration $\{6, 1.0\}$.

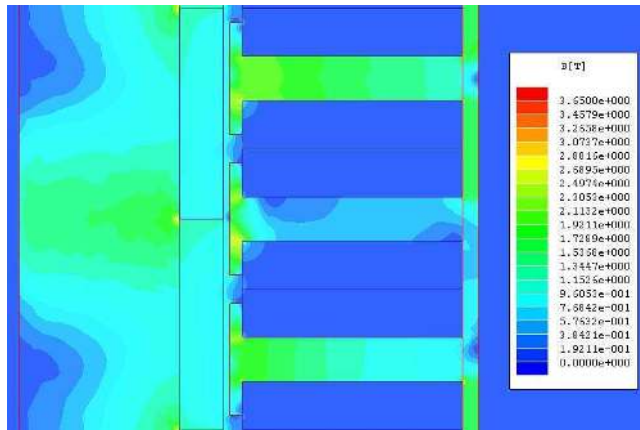


Figure 4.21: Flux density distribution for the actuator configuration $\{6, 1.6\}$.

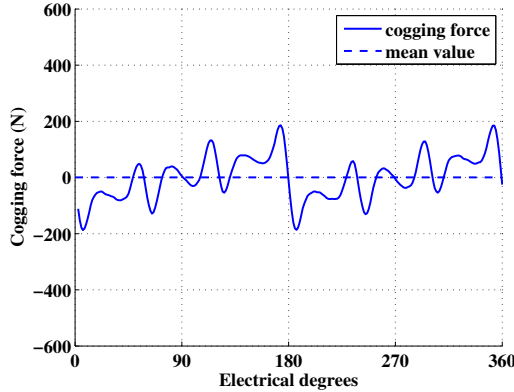


Figure 4.22: Cogging force for the actuator configuration $\{6, 1.0\}$.

offers an improved force output in terms of cogging, however it is characterized by a significantly lower force density and it does not satisfy the geometrical constraints. Therefore, if needed, a compromise may be found, for example, in the intermediate design solution $\{6, 1.3\}$.

Further, the translator displacement causes a variation of the magnetic flux density within both stator and translator. According to Faraday's law of electromagnetic induction, electromotive forces are induced by a varying magnetic flux, which leads to the appearance of closed-loop currents, or eddy-currents, within the conductive materials, i.e., iron-core and magnets. The direction of the eddy-currents is such that the generated magnetic field opposes the change of the original field. Consequently, the interaction of the two magnetic fields generates a repulsion force which opposes to the translator movement. The amplitude of the repulsion force is dependent on the speed of movement of the translator, which resembles a damping force characteristic. No lamination has been considered, thus the contribution of the eddy-currents damping is expected to be significant. The effects of this phenomenon can be predicted only by means of time-dependent, transient analysis. Two sets of results are given in Fig. 4.23, i.e., a translator displacement along 360 electrical degrees for a speed of 0.5m/s and 1m/s, respectively, in open-circuit conditions. The cogging force component can be recognized in both characteristics, however displaced into the negative half-plane, which indicates the presence of a damping force that opposes the translator movement and is dependent on its speed. The mean values of the

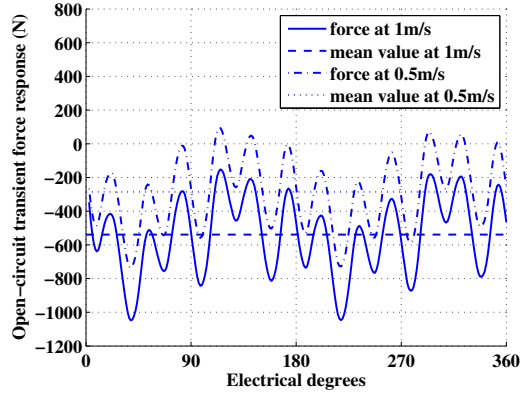


Figure 4.23: Transient force response under open-circuit conditions for a translator speed of 0.5m/s and 1m/s; the mean value of the force response is shifted because of the damping force component caused by eddy-currents.

force responses are displaced by 285N and 540N for 0.5m/s and 1m/s, respectively. For most applications, the eddy current damping would be minimized by laminating the iron core. However, this approach is particularly difficult for tubular actuators. In order to maximize the performance of the machine, a tubular structure should be laminated in the axial direction with a radial distribution of the lamination layers. However, as such it is not possible to obtain laminations of constant thickness, since the lamination thickness would increase along the actuator radius. Another option would be to perform lamination in the radial plane, but this would result in lamination layers being perpendicular on the magnetic flux path in the stator and translator back-iron, thus increasing the effective airgap and reducing the airgap flux density. A mixed laminated structure, with both radial and axial layers according to the orientation of the magnetic flux paths is theoretically possible, nonetheless it would be probably the most expensive option and would still affect the performance of the actuator.

On the contrary, considering the nature of the automotive application, eddy-current damping is a rather desired feature and the lamination of the iron core may not be required. The eddy current damping can be considered as the electromagnetic equivalent of the classical hydraulic damping especially if combined with regenerative damping. However, a compromise has to be made for an active suspension system considering the following: on one hand, eddy current

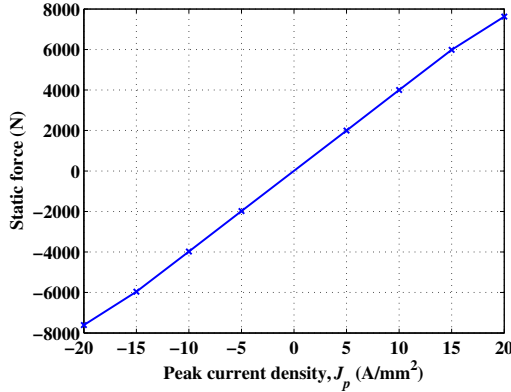


Figure 4.24: Static actuator force for zero displacement as a function of the coil peak current density, J_p , where the negative values are used to indicate the reversed direction of the current.

damping is viewed as a possible safety system when a failure of the electrical components of the electromagnetic active suspension occurs. On the other hand, this damping component cannot be switched on and off (it can be compensated at the expense of power consumption) and a high damping component would reduce the bandwidth of the entire suspension system, therefore, compromising one of the major advantages of a fully active electromagnetic suspension. As such, a certain contribution of the eddy-current damping is indeed necessary for fault conditions but not as the main damping force component. The mean damping force values obtained for this actuator configuration provide about 25% of the necessary damping force. Hence a rather reduced damping force would be available in case of an actuator or system failure.

Two other aspects that need investigation are: what current density value is required to achieve the specified peak forces and the associated potential demagnetization of the translator magnets. For this purpose, the force for the initial stroke position is calculated as a function of the stator coil current density. The results are depicted in Fig. 4.24 and they show a quasi-linear current-force dependency. An output force of 4kN is achievable for a current density of 10A/mm² and the safety peak force of 7.54kN (anti-roll + rebound damping) requires a current density of 20A/mm², hence two and four times the nominal peak current density, respectively. For the highest current density value, i.e.,

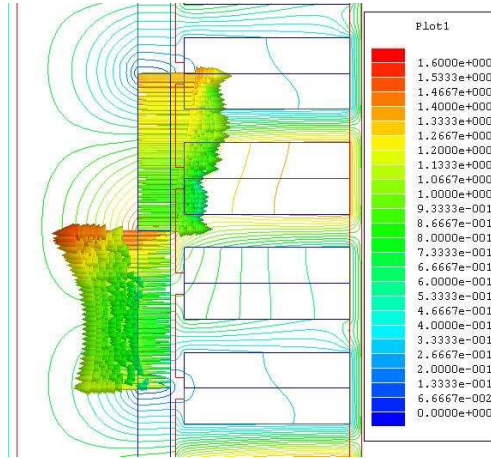


Figure 4.25: Magnet radial flux density at a peak current density of $10\text{A}/\text{mm}^2$

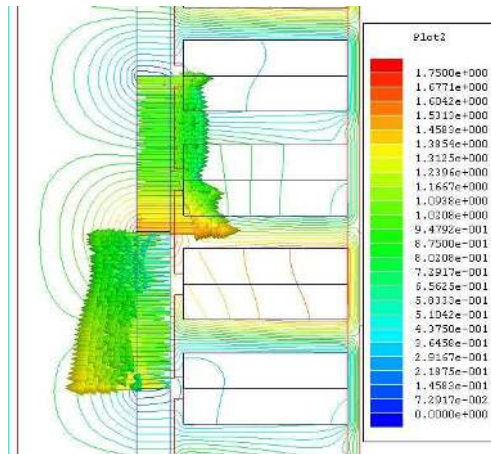


Figure 4.26: Magnet radial flux density at a peak current density of $20\text{A}/\text{mm}^2$.

20A/mm², Figs. 4.25 and 4.26 depict the distribution of the radial flux density vector over the magnet longitudinal cross-section for two adjacent translator magnets and for positive and negative peak current. In both cases the total radial field has a direction identical to the polarization of the magnets and the minimum flux density value is 0.4T approximately, which, for modern PM materials as the one suggested in Appendix C, stands well within the second quadrant of the PM demagnetization curve with a sufficient reserve of coercive force.

Returning to the actuator force versus displacement response which is severely affected by ripples, the following section discusses in more detail the minimization of the cogging force by means of skewing.

4.4.2 Translator skewing

The cogging force and the force ripples due to the winding distribution and the harmonics of the magnetic field can be minimized by means of stator or translator skewing, which reduces the high gradients in the change of the flux linkage as a function of translator position. However, at the same time, the flux linkage is reduced and thereby the back-EMF and the mean output force are affected due to skewing. An optimal skewed configuration is in fact a compromise between a minimized cogging force and ripples and a minimal loss of the back-EMF amplitude. The back-EMF shown in Fig. 4.27 is calculated in a transient FE simulation for a translator speed of 1m/s and one turn per stator coil (six turns correspond to one phase).

A schematic representation of stator and translator linear skewing next to a non-skewed topology are shown in Fig. 4.28 where, for a simpler two dimensional representation, the tubular actuator is shown unrolled. The force vectors which act on the stator coils are also depicted in the figure in order to reveal the fundamental difference between the two options. With stator skewing, the stator coils are not anymore perpendicular on the direction of movement, hence the angle of the force vector is modified and the axial force component decreases while a radial component appears and introduces a torque around the actuator axis of symmetry. The radial forces can be canceled by means of symmetric skewing, however the amplitude of the axial force can be significantly reduced with the increase of the skew angle. Furthermore, stator skewing brings technological difficulties since the manufacturing of a skewed stator part is more complicated and the also winding of the stator coils becomes rather difficult. In contrast, skewing the translator magnets does not modify the angle of the force vector since the direction of the flux density vector remains unchanged. The

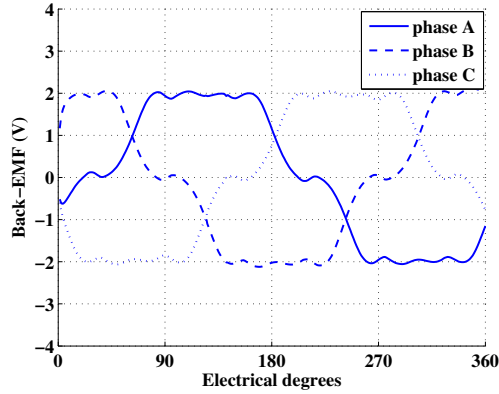


Figure 4.27: Back-EMF for a translator speed of 1m/s.

manufacturing of skewed full translator magnets increases the manufacturing costs, however, especially with surface mounted magnets, a piecewise skewed topology realized with arc shaped magnets is a cheaper but viable alternative.

Two skewed topologies are investigated in this section, i.e., triangular and sinusoidal. A tubular skewing topology has to be periodical in order to cancel out all force components other than axial, which due to the tubular structure may introduce torques in both radial and axial planes. This is achieved by utilizing periodical skewing profiles with at least two circumferential periods [87]. The resulting triangular and sinusoidal patterns with minimum number of circumferential periods are shown in Fig. 4.29a and b. An accurate calculation of the resulting tubular actuator topologies would require 3D FE analysis which suffers from rather high computational demands. A semi-analytical approach, verified in [87], is also adopted here. It consists of a shift and add method starting from a single 2D FE axial-symmetric solution, e.g., the cogging response given in Figs. 4.18. The translator surface is divided into longitudinal layers which are shifted in axial direction according to the given skewing profiles (Fig. 4.29c and d), therefore resulting in a discrete approximation of the ideal pattern. Each layer has an associated shifted response waveform with an amplitude given by a fraction of the original waveform. The total skewed response curve is then

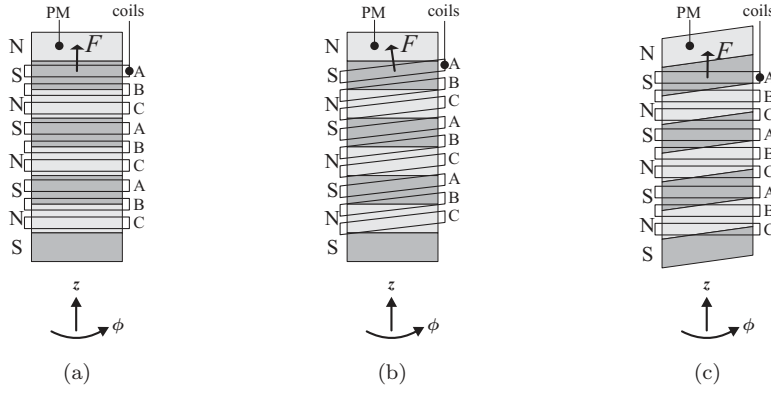


Figure 4.28: Schematic representation of stator and translator skewing: (a) no skewing, (b) stator skewing and (c) translator skewing.

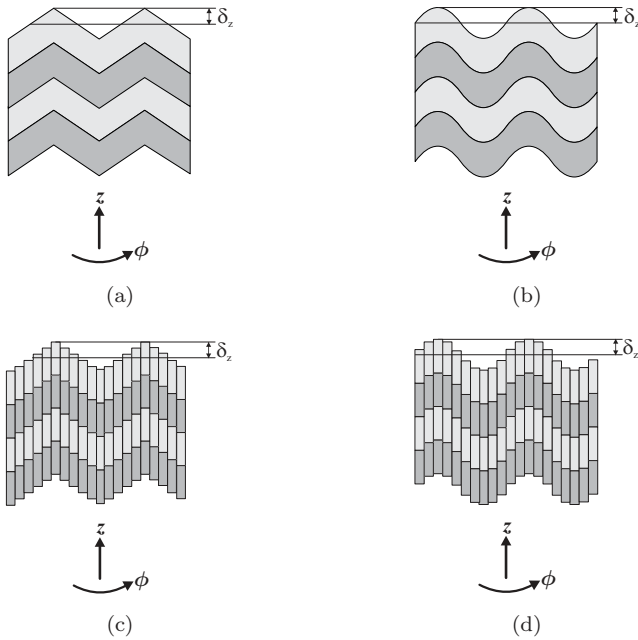


Figure 4.29: Skewing patterns: (a) ideal triangular, (b) ideal sinusoidal, (c) discrete triangular and (d) discrete sinusoidal.

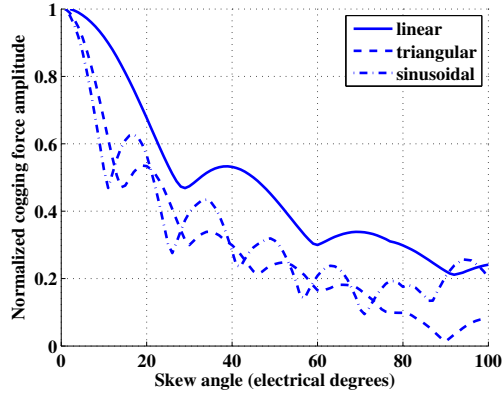


Figure 4.30: Normalized cogging force amplitude as a function of the skew angle.

obtained as the sum of shifted fractional waveforms, i.e.,

$$y_{sk}(\delta_z) = \frac{1}{n_l} \sum_{k=1}^{n_l} y_{usk}(T_{sk}(\delta_z, k)), \quad (4.28)$$

where y_{sk} and y_{usk} are the skewed and unskewed waveforms, respectively, δ_z is the skew angle, n_l is the number of layers and T_{sk} represents the skew transformation.

The effects of translator skewing on the cogging force amplitude and RMS and THD values of back-EMF are studied for a skew angle range up to 100 electrical degrees. The results are shown in Figs. 4.30, 4.31 and 4.32 where also a linear skewing pattern is presented for comparison purposes. It can be observed that the sinusoidal skewing provides the fastest drop for all three considered quantities, i.e., sinusoidal skewing requires a smaller skew angle to obtain the same result as the other two patterns. Nevertheless, the triangular pattern provides very similar results. Figure 4.31 shows that a 10% reduction in the RMS back-EMF is attained at $\delta_z = 38$ electrical degrees. If then only the lower skew angles are considered, there are two points within which may be considered (quasi-)optimal, i.e., for $\delta_z = 26$ and $\delta_z = 36$ electrical degrees. In the first case, a lower cogging amplitude is given by the sinusoidal pattern, while in the second case, an improved THD value is provided by the triangular pattern. The differences are rather small, however the difference for the THD value than for

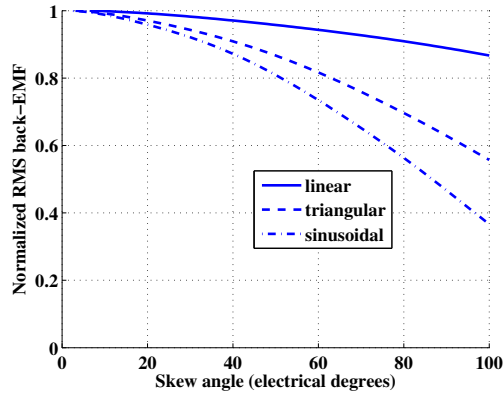


Figure 4.31: Normalized RMS back-EMF as a function of the skew angle.

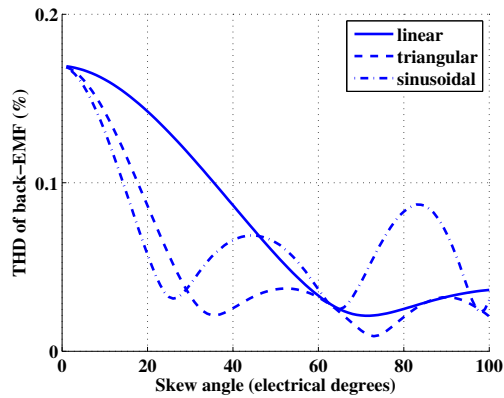


Figure 4.32: THD of back-EMF as a function of the skew angle.

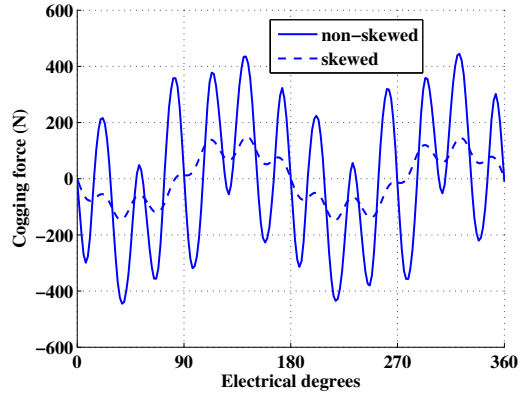


Figure 4.33: Cogging force comparison between the non-skewed and skewed topologies, where the triangular pattern with a skewing angle, δ_z , of 36 electrical degrees is considered.

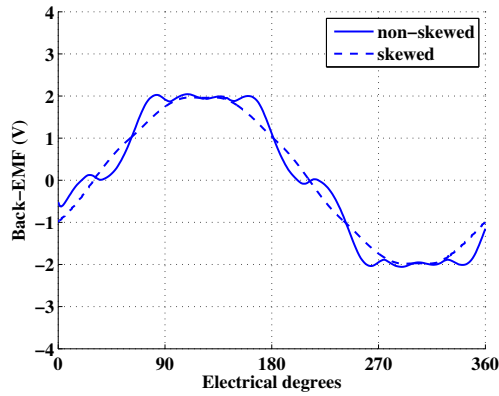


Figure 4.34: Back-EMF comparison between the non-skewed and skewed topologies, where the triangular pattern with a skewing angle, δ_z , of 36 electrical degrees is considered.

the cogging force. The resulting skewed cogging force and back-EMF waveforms for an angle $\delta_z = 36$ electrical degrees are given in Fig. 4.33 and 4.34. A cogging force reduction of 66.5% is achieved, which means that the cogging amplitude is now 149N or 6.6% from the total mean force. The RMS back-EMF has been reduced by 7.8%, however the THD has been minimized by 88% and is now only 2.1%, hence, the back-EMF presents an almost sinusoidal profile. Consequently, the mutual force ripples caused by the sinusoidal excitation and the original trapezoidal back-EMF will be also significantly attenuated. Different skewing angles for the stator teeth and the stator ends, therefore independent minimization of tooth-cogging and end-cogging, are also possible. It is shown in [87] how such an option can provide an improved reduction of the total cogging force. As a last remark, a 3D FE analysis is necessary in order to study the effects which cannot be projected in a 2D model, such as the three-dimensional distribution of the magnet flux leakage since this can affect the total flux linkage and hence the output force.

4.4.3 Temperature rise and distribution

The most critical aspect which can affect the performance of the actuator is the internal temperature distribution and the heat dissipation. High temperature levels can cause the degradation of the permanent magnets leading to irreversible demagnetization or the destruction of the coil insulation with a potential safety hazard. The prediction of the temperature distribution is a necessary step in the design of an electromagnetic actuator. However, compared with magnetic field simulations, more care is necessary when performing thermal simulations due to the fact that several critical model parameters, e.g., conduction, convection and radiation coefficients, which depend on geometrical properties and material distribution, are rather difficult to estimate without actual measurements.

A thermal design constraint has been included only in the optimization of the coarse model. The statement about the sufficient accuracy of the simplified temperature prediction given by (4.26) can be confirmed by static thermal FE analysis, nevertheless a simplifying assumption is necessary. In order to introduce (4.26) it was assumed that the temperature distribution within the actuator volume is uniform where this should be expected for component materials with high thermal conductivities. However, due to the coil insulation and slot lining material, the equivalent winding thermal conductivity drops to values, i.e., 1 - 10 W/mK, which are considerably lower than the one for the surrounding stator iron, i.e., 45W/mK. Consequently, two static simulations are

Table 4.8: Thermal material properties.

	Thermal conductivity (W/mK)	Specific heat (J/kgK)
Air	0.026	1007
NdFeb magnet	9	440
Copper	400	385
Iron	45	448
Aluminum	237.5	951

considered: firstly, coil insulation or stator lining are not considered, hence, the thermal conductivity of the winding region is set to the generic value for solid copper, i.e., 400W/mK, and secondly, a thermal conductivity of 4.5W/mK is attributed to this region, where this value is reported in the literature as a result of measurements [88] (thermal properties of the involved materials are listed in Table 4.8). Furthermore, in the first case, the convection boundary is defined only on the stator outer surface (as in the coarse model), whilst in the second case the boundary is defined over the entire outer actuator surface. The resulting temperature distributions for the two cases are shown in Fig. 4.35. The peak temperature in the first case is 101.4°C, i.e., 2.7°C higher than the coarse model value, and the temperature is indeed almost evenly distributed, hence it can be concluded that a good agreement exists between the two models. In the second case, which depicts the more realistic situation, the peak temperature is, rather coincidentally, very close to the value from the first case, i.e., 104.1°C, however, due to the extended convection boundary and the lower thermal conductivity of the winding region, a clear temperature gradient is visible. In this case, the temperature of the magnet region is at least 15°C lower than the peak value. It needs mentioning that the value of the copper resistivity is, as with the coarse model, defined for a temperature of 130°C. The resulting peak temperature is less than this reference value, thus a simple iterative loop can be implemented to adjust the copper loss to the actual temperature and obtain a more accurate result. A reduction in copper loss and peak temperature of approximately 10% would then be obtained.

It should be noted that the performance of modern magnetic and insulation materials allows for rather high operating temperatures. For example, synthetic insulation materials are capable of continuous operation at temperatures up to

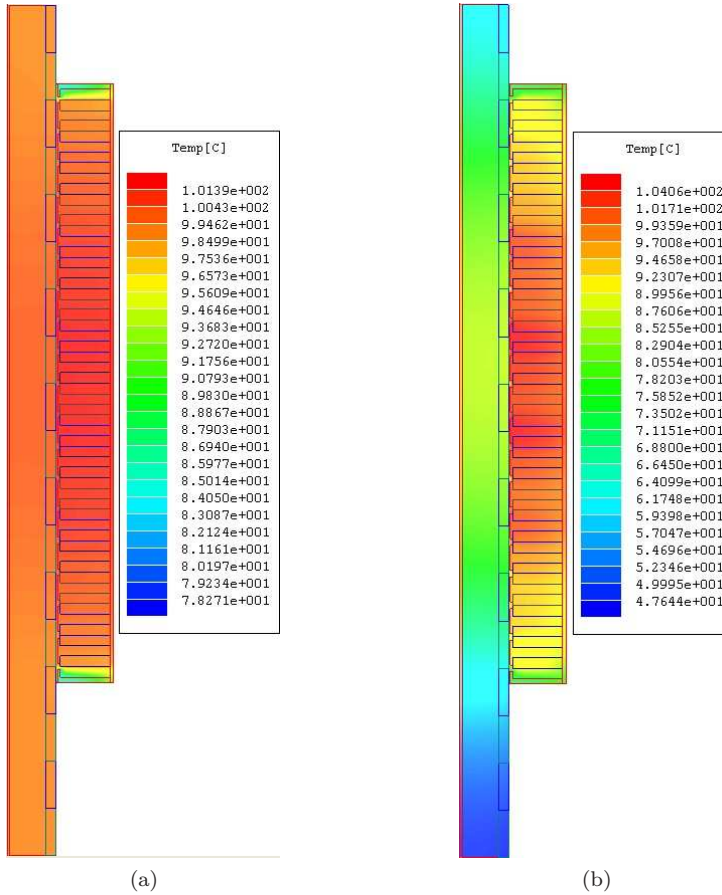


Figure 4.35: Temperature distribution: (a) a thermal conductivity of 400W/mK for the slot region and no slot insulation is considered, and (b) a reduced thermal conductivity of 4.5W/mK is considered for the slot region region, where this value is reported in the literature as a result of measurements [88].

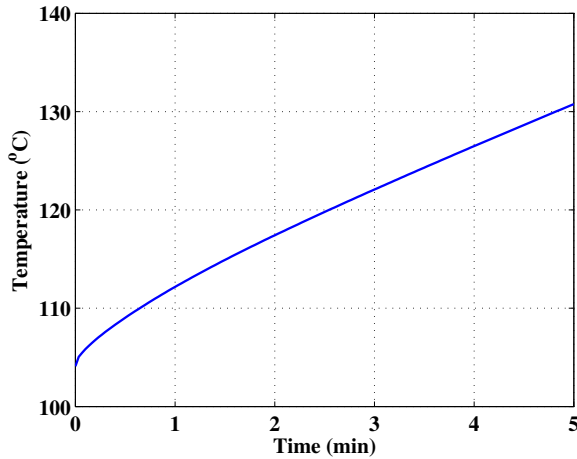


Figure 4.36: FE simulated peak temperature rise time from an initial temperature of 130°C.

250° [89] and different types of neodymium sintered magnets permit operating temperatures of up to 180° [90], with good demagnetization withstand capabilities. Hence, the temperature levels shown in Fig. 4.35b are within acceptable margins and should even allow for an increased current density that would lead to a rise in force density.

Both thermal and magnetic design should be viewed more at a system level. If a current vehicle model is considered, the tubular actuator would be integrated in a rather unsuited environment since the available power supplies and thermal management are not necessarily designed to integrate a high force density electromagnetic actuator. For sustained force output higher than the nominal and at the same time for safety reasons, force cooling should be integrated or direct air cooling should be improved by means of aerodynamic design of the car-body. The classical option of heat-sinks and fans mounted on the stator could be adopted, nonetheless it would lead to an unwanted increase in actuator volume. Independent heat-sinks connected to the actuator through high conductivity heat pipes and forced cooled by fans or free airflow may represent a better solution. Water cooling may be considered in a similar arrangement. Furthermore, thermal isolation between the engine compartment and the suspension struts is recommended.

As specified in Chapter 2, a peak force of 4000N is required for a maximum duration of one minute. Hence, it is necessary to estimate the temperature rise within one minute starting from the nominal steady-state value of 104.1°C. A transient thermal FE model is implemented with a peak excitation current of 10A/mm² and the copper loss calculated as before for the reference temperature of 130°C. From the time-dependent temperature response indicated in Fig. 4.36 it can be estimated that a negligible temperature rise, i.e., 8°C, is obtained after one minute and hence the peak anti-roll force may be attainable even without forced cooling.

A final observation needs to be mentioned, i.e., given the specific low voltage requirements of the automotive application, a winding configuration with a low number of turns has to be considered. Two options, with influence on both electromagnetic and thermal properties, are possible: several parallel strands of thin wire per coil turn or solid thick wires can be considered. A higher packing factor, virtually zero AC resistance and reduced thermal conductivity along the wire length are the characteristics of the first option, whilst a lower packing factor (can be improved by utilizing rectangularly shaped wires), an increased AC resistance due to skin-effects and higher thermal conductivity along the wire length are the properties of the second option. Considering the actuator cooling, the last property associated with thick wires may be favorable, since heat flow would occur also along the wire length. The study of this phenomenon is not possible with axial-symmetric FE models since heat flow occurs only in the circumferential direction, consequently, 3D FE analysis is required.

Several static and dynamic characteristics of the design solution chosen in Section 4.3.3 are investigated in this section in an attempt to give insight into further necessary design steps. The general conclusions about the considered SM based approach and viability of the proposed technological solution are summarized in the final section of this chapter.

4.5 Conclusions and remarks

Preliminary design considerations and a number of size optimization problems for a tubular PM actuator configuration are discussed and solved in this chapter. The obtained results indicate that a high force density actuator is required for the electromagnetic active suspension and, furthermore, that the considered slotted tubular PM actuator can fulfill the requirements defined in Section 2.5, namely, a nominal static force of 2kN within the available space envelope. Pre-design actuator configurations have been obtained by means of

AOSM optimization, i.e., fundamental sizes and stator configuration in terms of number of pole-pairs. It needs to be mentioned that all obtained solutions have to be interpreted as having only local optimality. Static and dynamic characteristics, e.g., total and cogging force response, damping force caused by eddy-currents, are investigated and the positive and negative effects of two skewing topologies are studied.

Comparison of the optimization results indicates that a design solution must be a compromise between high force/power density and reduced parasitic effects, e.g., force ripples. Several of the obtained solutions satisfy the imposed constraints and can be further considered for an extended electromagnetic and mechanical design procedure. Furthermore, the design of the power supply, the control system and the thermal management system is necessary.

The tubular PM actuator is integrated in a hybrid active suspension solution where the mass of the vehicle is sustained by mechanical springs. A large power consumption would be associated with a tubular actuator designed to, additionally, take over the function of the mechanical spring. Furthermore, no existing type of electromagnetic actuator can provide the spring characteristic without power consumption and additional control forces for the damping requirements. Therefore, a new type of electromagnetic actuator is synthesized and dimensioned by means of AOSM-based shape optimization in Chapter 5.

5

Case II: Novel electromagnetic spring for active suspension

5.1 Introduction

A novel configuration of electromagnetic actuator, with a potential application in automotive active suspension, is proposed and investigated in this chapter. In addition to the functions discussed in Chapter 4, i.e., anti-roll and damping, this actuator should also provide the support force for the vehicle mass without power consumption, therefore, eliminating the necessity of incorporating a mechanical spring in the suspension strut. Furthermore, this so-called passive response should present the same linear force characteristic as the mechanical spring. Considering the large force required to support the vehicle mass and the fact that electromagnetic actuators are generally characterized by non-linear responses, the mentioned design requirements lead to a rather challenging design problem.

As discussed in the previous chapter, a cogging component is present in the force response of linear PM actuators. This force component is caused by the interaction between the stator slots/ends and the translator permanent

magnets, i.e., the stator and translator attempt to align in such a way that minimal magnetic reluctance is achieved, hence, maximum stored magnetic energy. Therefore, when moving the translator through a slotted stator, with no winding excitation, the cogging force acts either forward or backward relative to the direction of motion. As this force is purely caused by the interaction between the magnets and the stator iron, the cogging force is a zero-power force. In general, the cogging force is considered to be an undesired component because it introduces a periodical perturbation or ripple in the total force response. However, this force component can also be exploited in order to obtain a zero-power linear response for an electromagnetic spring (ELMASP). This idea has been investigated in [25] where a pre-prototype ELMASP has been modeled and build. Section 5.1.1 presents briefly the characteristics of this pre-prototype, denoted as the α -ELMASP, nevertheless an extension of this initial design is necessary because the provided force output is about ten times less than required and a redesign of the α -ELMASP leads in Section 5.3 to an unfeasible solution due to a very large size. Noting that the amplitude and shape of the zero-power response characteristic will be determined solely by the geometry of the actuator, the design problem will be approached in two steps. Firstly, a new actuator topology is proposed in Section 5.4 with the actual dimensions of the actuator being determined by means of AOSM optimization, having as design objective the passive force response which is defined in Section 5.2. The experimental validation of this actuator solution and its zero-power response is also presented in Section 5.4. Secondly, the design is extended in Section 5.6 by incorporating active elements, i.e., excitation coils, with a novel commutation scheme that provides the coverage of the response envelope defined in Section 5.2. The terms *passive* and *active* will be used to differentiate between the two design steps and operation principles.

The equation of motion for a suspension strut is given by:

$$m\ddot{z} = kz + d\dot{z} + F_{act}, \quad (5.1)$$

where m is the mass, k is the spring stiffness, d is the damping coefficient, F_{act} is the actuator force and z , \dot{z} and \ddot{z} , are the position, velocity and acceleration respectively. If the mechanical spring and hydraulic damper are removed and actuator force is divided into subcomponents, the above equation can be written as:

$$m\ddot{z} = [k_m + k_i(i)]z + [d_{iron} + d_i(i)]\dot{z}, \quad (5.2)$$

where k_m and d_{iron} are the passive electromagnetic spring stiffness and damping coefficient and $k_i(i)$ and $d_i(i)$ are the active electromagnetic spring stiffness and

damping coefficient. These coefficients indicate the possible force production mechanisms in the ELMASP:

1. k_m - cogging force,
2. k_i and d_i - mutual alignment and reluctance force in actuator mode,
3. d_{iron} - (passive) reaction force due to the eddy currents induced in the iron core,
4. k_i and d_i - (controllable) reaction force in generator mode.

The design approach in this thesis concentrates on the first two terms, k_m and k_i . The damping properties will only be checked as a post-processing step. The above definition of the coefficients is not necessarily unique and might be even confusing considering that they cannot be unequivocally related to their mechanical counterparts. Supposing that d_{iron} and d_i are zero, an electromagnetic actuator can very well provide 'damping forces' due to its (controllable) active force response represented here by $k_i z$. Therefore, from electromagnetic point of view, it makes more sense to talk about the envelope of the force response, as introduced in Section 5.2) because this covers both spring (needed for the vehicle mass support and roll compensation) and damping responses (needed for vibration compensation). Nonetheless, the damping force generated by the induced eddy currents could significantly affect the performance of the actuator and it should be included in the investigation.

5.1.1 A pre-prototype: the α -ELMASP

An ELMASP pre-prototype, hereafter referred to as the α -ELMASP, has been investigated in [25] where simulated data has been verified by means of measurements. This tubular electromagnetic spring was built for verification purposes using commercially available components, therefore it is not an optimized design. A coil is incorporated in the translator slot, which allows for variation of the spring stiffness by means of an excitation current. The α -ELMASP has an axial-symmetric configuration which allows for reduced 2D representation and modeling. Figure 5.1 shows the configuration of the actuator and the considered sizes. Aluminum is used for non-magnetic parts of the prototype. Standard mildsteel (1010 steel) is used as the soft-magnetic material, where the hard magnetic material is bonded NdFeB. The coil incorporates 105 turns, each having a cross-section of 2.65mm^2 , resulting in a copper filling factor of 0.56. Further details about the material properties and the measurements setup are given in [25].

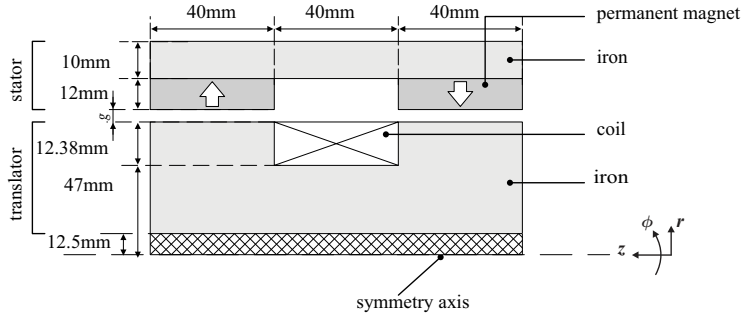


Figure 5.1: Geometrical configurations and dimensions of the α -ELMASP pre-prototype.

As shown in Fig. 5.2, the FE response, F_{fe} , and the measured force, F_{meas} , for the α -ELMASP prototype with no excitation current have a high correlation. The active response is also given in Fig. 5.2, where the excitation current takes the values of -15.0A and 15.0A , respectively, which corresponds to a wire current density of $-5.67\text{A}/\text{mm}^2$ and $5.67\text{A}/\text{mm}^2$. All measured characteristics present two lines, due to the hysteresis effect occurring in the iron core because the magnitude of the field varies as a function of the displacement.

Even though the α -ELMASP is a reduced-scale and not optimized pre-prototype, it offers the fundamental concept for the design of an innovative full-size actuator. However it is shown in Section 5.4 that the topology given in Fig. 5.1 cannot satisfy the full-scale design requirements and thus a modified configuration is proposed in this chapter.

5.2 Design requirements: the output force envelope

The most relevant design requirement for the ELMASP is a linear passive force output with a stiffness, k_s , of $30\text{kN}/\text{m}$, as obtained in Chapter 2 from the measurements of the mechanical spring. The force amplitude at the middle of its stroke range must be equal to the static nominal force given in Table 2.7, i.e., 4.41kN . Following from the data shown in Chapter 2, Fig. 2.11 and Table 2.5, the stroke range can be approximated to $0.14\text{--}0.16\text{m}$. Consequently, a linear passive force response as given in Fig. 5.3 is obtained. It can be observed that, if extrapolated, this characteristic would not cross the origin. It is expected that the actuator will have a nonlinear response with a rapidly increasing force value

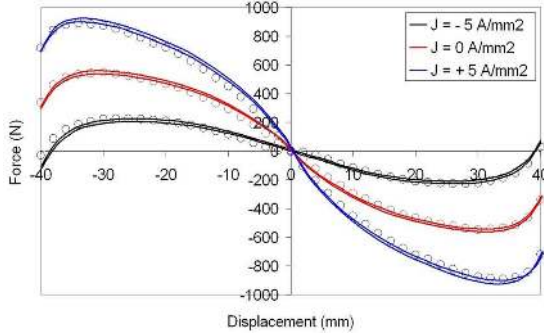


Figure 5.2: Measured (lines) and calculated (circles) response characteristics for the α -ELMASP.

at the beginning of the stroke and enter the desired linear region at a displacement value of 0.01m. If the passive linear response would start from the origin, the initial value of 1.7kN would be reached at a displacement of 0.056m, therefore resulting in an unnecessary increase of the total stroke by approximately 25% which will also requires an increased actuator length. Fig. 5.3 indicates the lower and upper boundaries of the actuator force envelope. These boundary values are determined following the same reasoning as in Section 4.3.1, i.e., a force output of 4kN should be sufficient to cover both typical anti-roll and damping requirements. However, the anti-roll component of the output force is required for the upper region of the stroke because anti-roll forces have to be provided by the actuators placed on the side of the vehicle found on the outer-side of a curve and these forces will be added to the passive response. Therefore, the force envelope can be reduced in the lower stroke region in order to account mostly for the damping requirements.

As an extra remark, if the anti-roll and damping are viewed as independently occurring regimes, they can be represented in Fig. 5.3 as vertical and horizontal trajectories, respectively. In an ideal anti-roll regime, the vehicle body-roll is zero which means that the actuator displacement has to be zero and thus the actuator force will follow a vertical trajectory around the passive equilibrium point. In an ideal damping regime, no vibrations should be transmitted from the road to the sprung mass, through the unsprung mass, which means that the actuator force has to remain constant and the displacement will follow a horizontal trajectory around the passive equilibrium point.

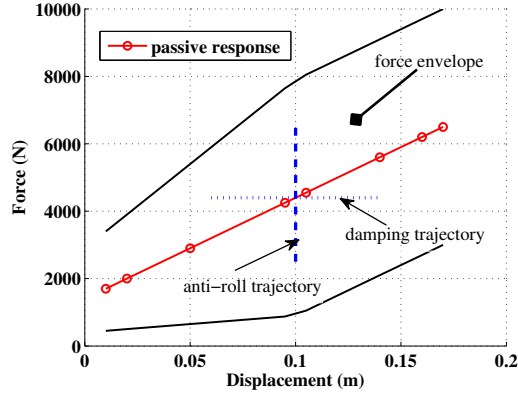


Figure 5.3: ELMASP required passive response and total force envelope.

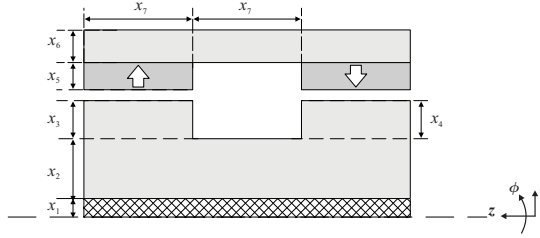
The force envelope defined by the lower and upper boundaries in Fig. 5.3 is not a strict design requirement. The main focus in this chapter is on the passive response which will be considered in the definition of the design optimization problem in the following section.

5.3 AOSM size optimization of the α -ELMASP

The α -ELMASP pre-prototype, presented in Section 5.1.1, provides a maximum passive force response of almost 600N, while the full scale requirement indicated in Fig. 5.3 is 6.5kN. The first step in the design of a full scale prototype is to investigate if the α -ELMASP configuration can fulfill the design requirements. For this purpose, the AOSM technique is implemented to solve a size optimization problem considering the most relevant design specifications, i.e., to determine if the α -ELMASP concept can provide linear passive response as defined in Section 5.2 while satisfying the physical constraints imposed by the available volumetric envelope.

5.3.1 Design specifications and problem formulation

Considering the actuator configuration from Fig. 5.1, a set of seven design variables is introduced (the translator excitation coil is disregarded), as shown in Fig. 5.4. The volumetric envelope is defined by the geometrical parameters

Figure 5.4: α -ELMASP design variables.

introduced for the tubular actuator in Table 4.1, i.e., a maximum axial length $L_a \leq L_t = 0.6\text{m}$ and a maximum radius $r_a \leq r_t = 0.08\text{m}$. The optimization problem is implemented in a relaxed form in order to facilitate a solution. A design requirement for the force response is imposed explicitly for the maximum value of 6.5kN , not for the entire characteristic, thus only one equality constraint is introduced. Noting that the actuator length is defined by $L_a = 3x_7$, its corresponding geometrical constraint could be imposed by means of the upper bound constraint for the variable x_7 . However, in the α -ELMASP configuration there is intrinsic dependency between the stroke range and the axial length, i.e., $L_a \geq 3s$, and, as visible from Fig. 5.3, the total stroke range of the actuator will be at least 0.170m . Thus, the respective constraint will be violated and the upper bounds on the variable x_7 is used to limit the violation margin. The requirement related to the maximum radius is introduced in the form of the objective function, i.e., the minimization of the outer actuator radius. As shown in Fig. 5.4, two independent design variables are introduced to define the respective lengths of the two translator teeth. In this way, the degrees-of-freedom of the optimization problem are increased and a more unconventional design solution is possible. One of the factors which significantly influences the shape of the force characteristic is the magnetic flux density amplitude in the iron core. Therefore, two additional constraints on the amplitude of the flux density in the translator and stator back-iron are introduced. These constraints are imposed only in the coarse model because the exact fine model values are not significant, only their influence on the force response. No linear equality or inequality constraints are defined. Table 5.1 summarizes the mentioned design

Table 5.1: Design requirements.

Electromagnetic	
Maximum force	$F _{z=0.170} = F_0 = 6.5\text{kN}$
Flux density	$B_i^{coarse} \leq B_0 = 0.3\text{T}$
Geometric	
Outer radius	$r_a \leq r_t = 0.08\text{m}$
Design domain	$x_{low} = [0.001, 0.001, 0.001, 0.001, 0.001, 0.001, 0.175]\text{m}$ $x_{up} = [0.200, 0.400, 0.200, 0.200, 0.200, 0.200, 0.185]\text{m}$

requirements and the optimization problem can be formulated as follows:

$$\begin{aligned}
 & \text{minimize} \quad \mathcal{F}(\mathbf{x}), \quad \mathbf{x} \in \mathbf{X} \subseteq \mathbb{R}^7, \\
 & \text{subject to} \quad g_i(\mathbf{x}) \leq 0, \quad i = 1, \dots, 2, \\
 & \quad \quad \quad h_j(\mathbf{x}) = 0, \quad j = 1,
 \end{aligned} \tag{5.3}$$

where the nonlinear constraints are

$$g_i = B_i^{coarse} - B_0, \quad i = \{1, 2\} \tag{5.4}$$

and

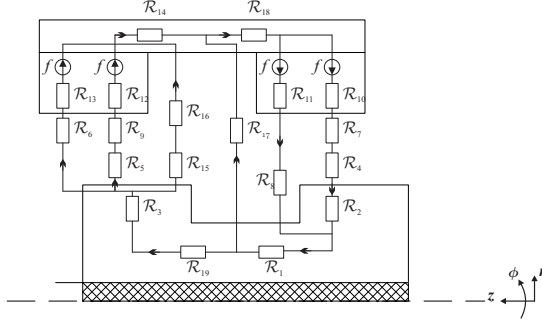
$$h_i = F_j - F_0, \quad j = 1. \tag{5.5}$$

5.3.2 Coarse and fine models

Similar to the approach from the Chapter 4, the coarse and fine models chosen are a MEC model and an FE model, respectively.

Coarse model

Even though the force response for only one position is required, the considered MEC model can provide the entire force versus displacement response, i.e., the reluctance elements are position dependent. The following simplifying assumptions are included: the iron core and PM materials are considered linear, with a relative magnetic permeability and a relative recoil permeability as indicated in Table 4.2. In contrast to the case of the tubular actuator where the airgap fringing flux can be neglected, the α -ELMASP force response is significantly

Figure 5.5: α -ELMASP MEC model.

influenced by the air flux paths and fringing end-effects since the α -ELMASP cogging force is in fact end-cogging. The MEC model is depicted in Fig. 5.5 and the system matrix and source vector for the resulting system of equations, together with the expressions of the reluctance elements and MMF sources, as functions of the design variables, are given in Appendix B.3.

After solving the system $\mathbf{R} \cdot \Phi = \mathbf{f}$, the flux density values within the defined magnetic paths can be determined. Further, the total magnetic co-energy can be approximated by

$$W' = \frac{1}{2} \sum_{i=1}^n \frac{B_i^2}{\mu_i} V_i \quad (5.6)$$

where B_i , μ_i and V_i are the flux density, magnetic permeability and volume corresponding to the reluctance element \mathcal{R}_i , with $n = 19$. Consequently, the force is determined from

$$F = - \left. \frac{\partial W'}{\partial z} \right|_{I=const.}, \quad (5.7)$$

where I represent the magnet MMF in this case.

Fine model

A reduced FE model of the actuator is possible due to its axial-symmetry and is implemented using the magnetostatic solver of the MAXWELL 2D software package [84].

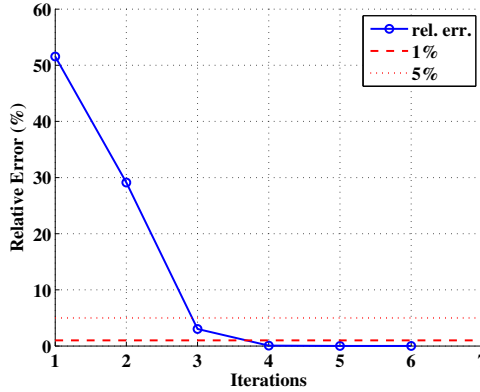


Figure 5.6: AOSM convergence history for the α -ELMASP solution, i.e., the convergence of the fine model force response.

5.3.3 Results

Five iterations were sufficient for the AOSM routine to converge to the solution $x = [0.001, 0.185, 0.001, 0.001, 0.007, 0.075, 0.175]$ and reach the force specification within the pre-defined precision of 1%. The convergence history is shown in Fig. 5.6, i.e., the convergence of the fine model force response. The actuator force response for this design solution, shown in Fig. 5.7 together with the passive specification, approximates the required passive characteristic. However, the actuator outer radius is 0.27m, which is a value much larger than the required 0.08m. Several trials, with different values of the constraint imposed on the back-iron flux density, have been performed and similar results have been obtained. This indicates that a design solution based on the α -ELMASP configuration is rather improbable. Consequently, a modified actuator topology is necessary and a possible solution is proposed in the next section.

5.4 Novel ELMASP topology

Many possible actuator configurations which could satisfy the specified design requirements may exist. However, it is beyond the scope of this thesis to identify several possible solutions. This chapter proposes and verifies a novel proof-of-concept ELMASP topology, which is derived from the α -ELMASP de-

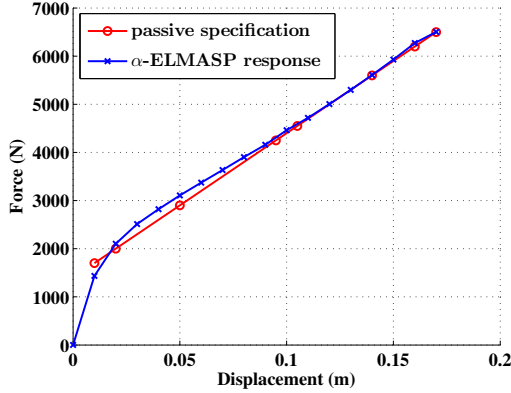


Figure 5.7: Force response of the AOSM α -ELMASP solution.

sign. An international patent [91] related to the ELMASP concept has been issued. As already mentioned, the focus is oriented on the passive response specification. The active elements are considered at a later stage as an addition to the passive solution. A linear active force versus displacement response would be desired, however, it is not strictly required because the active regime would be in general a dynamic regime with rather random trajectories in the force versus displacement plane.

There are two main design goals, in addition to the linear force output, which have to be undertaken, i.e., an increased force density in order to reduce the actuator volume and the minimization of the translator mass (the unsprung mass). Therefore, the following design modifications are introduced:

- the stator is extended with one pole pitch, which is defined by x_7 in the case of the α -ELMASP, in order to increase the effective airgap volume;
- to provide for a reduced translator mass, a double stator (double airgap) configuration is chosen and the translator back-iron is eliminated;
- the new translator is composed from two PMs interconnected by an iron-core element;
- in order to assure the structural strength of the translator, a non-magnetic back-plate has to be considered; this plate will increase the effective airgap length and its thickness is considered as a design variable;

- the stator magnets are shifted by one pole-pitch and stator iron teeth are introduced.

These design choices lead to a rather different actuator configuration which is shown in Fig. 5.8. In the initial position, as shown in the Fig. 5.8, there are two preferred magnetic flux paths flowing in the axial plane: the first closes through the lower translator magnet, the lower stator teeth and back-iron, the lower stator magnets and translator iron core, and the second closes through the upper translator magnet, the upper stator teeth and back-iron, the lower stator magnets and translator iron core. Very little flux will link the upper stator magnets. At this position the main flux paths are the shortest, therefore a maximum flux linkage is achieved and, thus, this is the preferred aligned translator position. If the translator is displaced in the positive z -direction, a negative force will be exerted on the translator which will tend to move it back in the aligned position. In contrast to the α -ELMASP, two force components can be identified:

- a cogging force component given by the interaction between the translator magnets and the slotted iron structure of the stator;
- a mutual repulsion force (the equivalent of the mutual alignment force defined in Section 4.4) exerted between the stator and translator magnets due to their opposite magnetization.

Noting that when the translator is displaced in the positive axial direction, the translator and stator magnets will partially overlap and due to their opposite magnetization there is a risk of demagnetization. This aspect has to be taken into account in the design process. The design procedure for the passive response characteristic is undertaken in the following section.

5.5 Passive design: AOSM shape-optimization

Compared to the previously discussed optimization problems, i.e., the tubular actuator in Section 4.3 and the α -ELMASP in Section 5.3, the ELMASP design problem has a significantly increased difficulty level due to the higher number of design variables and constraints. As shown in Fig. 5.8, the number of design variables has increased to eighteen. Furthermore, two design variables are assigned to each stator teeth and, therefore, sloped-face teeth are allowed as a possible solution. This also defines the optimization problem as a shape optimization problem.

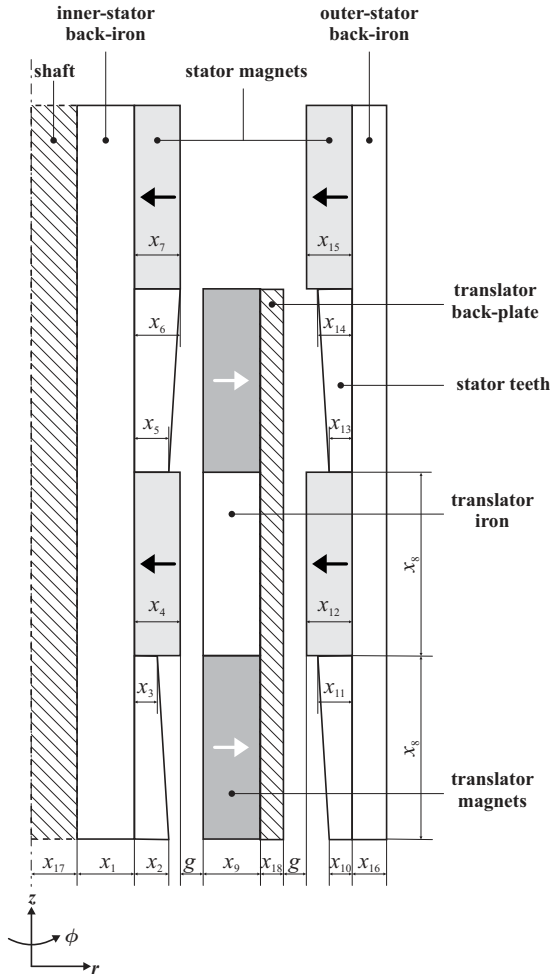


Figure 5.8: Novel ELMASP topology and the corresponding design variables.

5.5.1 Design specifications and problem statement

There are three main design goals which have to be formulated into an optimal design problem, i.e.,

- a linear force versus displacement response with a force stiffness $k_s = 30\text{kN/m}$;
- a reduced outer actuator radius;
- the minimization of the translator mass.

An additional geometric requirement is related to the actuator axial length, however, as with the α -ELMASP, there is an intrinsic dependency between the stroke range and the actuator axial length. The actuator pole-pitch, x_8 , has a lower bound given by the maximum stroke and noting the axial length of the actuator is $L_a = 4x_8$ it becomes clear that the violation of this geometrical constraint is even larger than in the α -ELMASP. It can be argued that a stroke range of up to 0.17m is not realistic because, in practice, the suspension travel is much smaller. Consequently, the actuator axial length can be reduced by specifying a shorter stroke range. Nevertheless, the scope of the thesis is to provide a proof-of-concept design and hence the total length of the actuator is not strictly imposed.

The linear profile is better constrained by choosing a large number of points at which the ELMASP force response should match the specifications. However, this also increases the number of FE simulations and, thus, the total calculation time. As less points as possible should be used. Noting that the design requirements specify that a constant force stiffness should be obtained and that the stiffness can be approximated by finite differences, pairs of neighboring points have been defined in Section 5.2 at the initial, middle and end stroke, i.e., at 0.01, 0.02, 0.095, 0.105, 0.16 and 0.17m. The actual calculation of the stiffness coefficient is not necessary. The force response constraints are reinforced with the addition of two extra points at 0.05 and 0.14m.

The ELMASP force response is constrained to the first six points defined on the passive specification from Fig. 5.3. As described in Chapter 2, the vehicle suspension strut includes a rubber bump-stop which introduces a very steep increases of the spring stiffness towards the maximum displacement. The linearity of the passive actuator response is not critical in this region due to the fact that the spring stiffness introduced by the bump-stop is dominant. The actuator outer radius, r_a , is limited by introducing the linear inequality

constraint

$$r_a = x_1 + \max(x_4, x_7) + 2g + x_9 + \max(x_{12}, x_{15}) + x_{17} + x_{18} \leq r_t, \quad (5.8)$$

where the additional linear constraints are defined to limit the length of the stator teeth to the maximum given by the length of stator magnets, i.e.,

$$\begin{aligned} x_2, x_3, x_5, x_6 &\leq \max(x_4, x_7), \\ x_{10}, x_{11}, x_{13}, x_{14} &\leq \max(x_{12}, x_{15}). \end{aligned} \quad (5.9)$$

These constraints are introduced with the scope of reducing the effective airgap length and limit the PM leakage flux through the adjacent stator teeth.

Additional geometrical constraints are considered in order to reduce the PM demagnetization risk, thus, the translator magnet thickness is constrained to be equal to the added thickness of the stator magnets:

$$\begin{aligned} x_9 &= x_4 + x_7, \\ x_9 &= x_{12} + x_{15}. \end{aligned} \quad (5.10)$$

In this manner, the resultant magnet MMF, when the stator and translator magnets are overlapping, is zero and there are no dominant magnets along a flux path. It is understood, that this is an idealized constraint and that its actual effectiveness will be verified in post-processing. Nevertheless, following from (5.10) two design variables become dependent variables and can be eliminated, hence, the variables x_{12} and x_{15} are disregarded and the total number of variables is reduced to sixteen.

Following the same reasoning as in Section 5.3, the back-iron flux densities are limited only in the coarse model. The translator mass is defined as the optimization objective, i.e.,

$$\mathcal{F}(\mathbf{x}) = M_{tr}(\mathbf{x}). \quad (5.11)$$

Therefore the resulting optimization problem is given by:

$$\begin{aligned} &\text{minimize } \mathcal{F}(\mathbf{x}), \mathbf{x} \in \mathbf{X} \subseteq \mathbb{R}^{16}, \\ &\text{subject to } g_i(\mathbf{x}) \leq 0, i = 1, \dots, 2, \\ &\quad h_j(\mathbf{x}) = 0, j = 1, \\ &\quad \mathbf{A} \cdot \mathbf{x} \leq \mathbf{b}, \end{aligned} \quad (5.12)$$

where the nonlinear constraints are

$$g_i = B_i^{coarse} - B_0, i = \{1, \dots, 9\} \quad (5.13)$$

Table 5.2: Design requirements.

Electromagnetic	
Force	$F_0 = [1.70, 2.00, 2.90, 4.25, 4.55, 5.60]\text{kN}$
Displacement	$z = [0.010, 0.020, 0.050, 0.095, 0.105, 0.140]\text{m}$
Flux density	$B_i^{coarse} \leq B_0 = 5\text{T}$
Geometric	
Outer radius	$r_a \leq r_t = 0.08\text{m}$
Design domain	$x_{low} = [0.001, 0.001, 0.001, 0.001, 0.001, 0.001, 0.001, 0.190, \dots$ $0.002, 0.001, 0.001, 0.001, 0.001, 0.001, 0.001, 0.001]\text{m}$ $x_{up} = [0.050, 0.050, 0.050, 0.050, 0.050, 0.050, 0.050, 0.210, \dots$ $0.050, 0.050, 0.050, 0.050, 0.050, 0.050, 0.050, 0.020]\text{m}$

Table 5.3: Material properties and design parameters.

Material properties	
PM mass density	$\rho_m = 7700\text{kg/m}^3$
Iron mass density	$\rho_{Fe} = 7650\text{kg/m}^3$
PM remanent flux density	$B_r = 1.15\text{T}$
Other parameters	
Airgap length	$g = 0.001\text{m}$

and

$$h_i = F_j - F_0, j = \{1, \dots, 6\} \quad (5.14)$$

with the corresponding design requirements being given in Table 5.2.

5.5.2 Coarse and fine models

The same model choice as in the previous sections is considered, i.e., a MEC model and an FE model. The material properties and other design parameters considered for the implementation of the models are given in Table 5.3.

Coarse model

The ELMASP MEC model is shown in Fig. 5.9. This model follows the same simplifying assumption as for the α -ELMASP and it provides a position dependent force response. However, because of the extended and double stator structure, the influence of the end-fringing flux is less significant. The length of the stator teeth is defined by two design variables, thus, it is also necessary to define variable reluctance elements which take into account the face-slope of the stator teeth, where this translates into position dependent airgap reluctances. The derivation of the reluctance elements and MMF sources is done in a similar manner as for the tubular PM actuator (Section 4.3.2) and the α -ELMASP (Section 5.3.2), however, due to a very large size, the system matrix and the expressions of the MMF sources and the reluctance elements are not detailed further in this thesis. The total magnetic co-energy is calculated using (5.6) and the force for each displacement value is determined from (5.7).

Fine model

The axial-symmetric geometrical configuration of the ELMASP allows for a 2D FE magnetostatic model [84] to be considered.

5.5.3 Results

For this design problem only a pseudo-convergence has been obtained. The force constraints have not been reached within a precision of 1%. As visible in Fig. 5.10, four of the constraints are reached within the required precision after ten iterations, one constraint is within 5% and the another has a divergent trend. It also needs noting that the constraint imposed on the outer actuator radius has been relaxed from 0.08m to 0.1m due to the fact that no solution has been obtained with the initial constraint value.

The causes for this convergence behavior can be explained by analyzing the results of the coarse model optimization performed at each AOSM iteration. In the case of the new ELMASP design, a rather poor success rate has been obtained with the coarse model optimization by means of the SQP routine, which has been used successfully in the case of the linear PM actuator and the α -ELMASP. Therefore, a different algorithm has been employed, i.e., the CONDOR optimization algorithm [92]. This algorithm proved to be better suited for this problem. One drawback of the version employed is that only nonlinear inequality constraints are supported. However, the force response constraint is an equality constraint which had to be included by augmentation

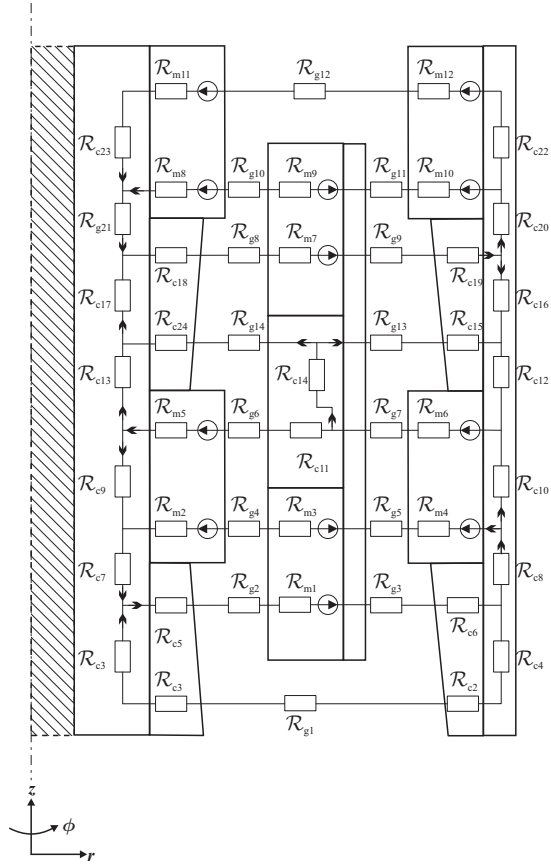


Figure 5.9: ELMASP MEC model.

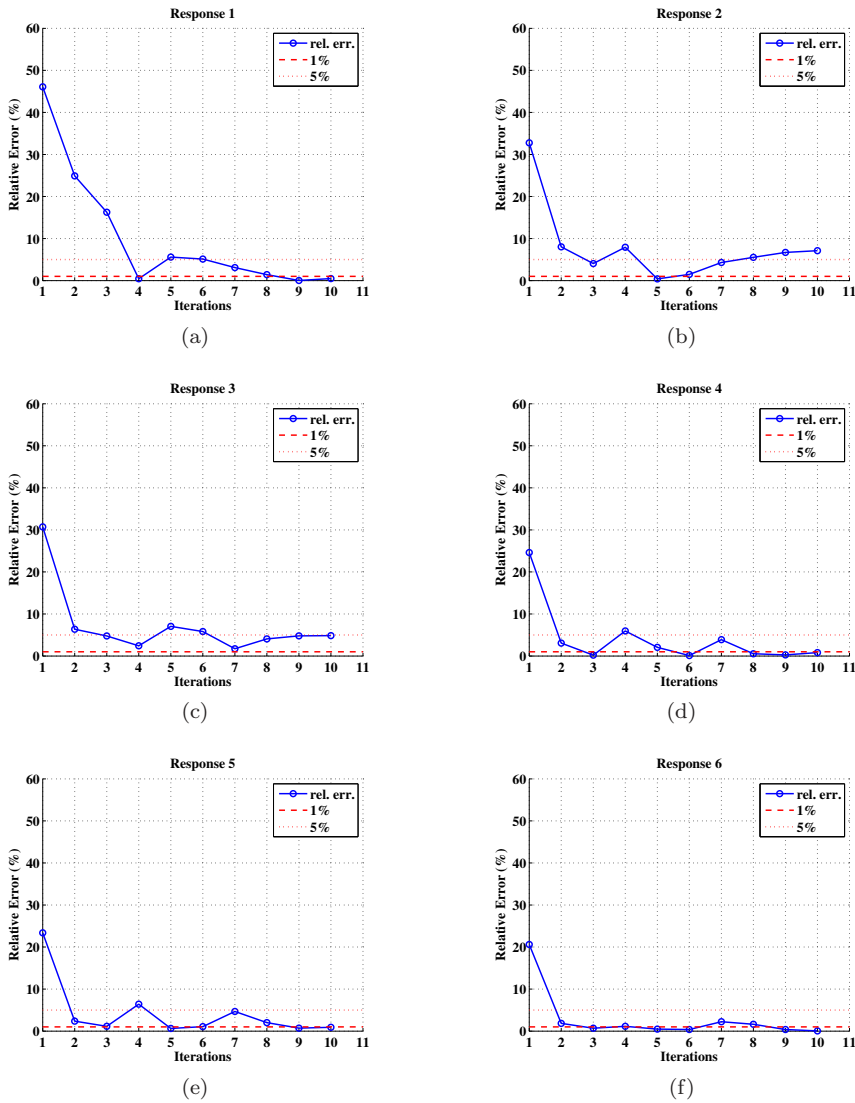


Figure 5.10: AOSM convergence history for the novel ELMASP solution, i.e., the convergence history of the fine model force respons for the six imposed values given in Table 5.2, where the sub-figures (a) to (f) correspond to the fine model responses 1 to 6, respectively.

of the original objective function. The l_1 penalty function approach, described in Section 3.2.6, is considered for this purpose. Consequently, the objective function from (5.11) becomes

$$\mathcal{F}(\mathbf{x}) = M_{tr}(\mathbf{x}) + \nu \sum_{k=1}^6 |h_k(\mathbf{x})|, \quad (5.15)$$

where h_k are given by (5.14). As discussed in Section 3.2.6, a lower accuracy can be expected from this type of implementation. Nevertheless, perhaps the dominant source of errors is the coarse model itself. This design example is useful in showing the limitations of the MEC models in optimization. The coarse model force response for the optimal solutions obtained at each iteration are showed in Fig. 5.11 and Fig. 5.12 together with the respective specification. It can be observed that the coarse model is not able to match the imposed specification for the first part of the stroke range. This error, present in the coarse model solution, affects the accuracy of the entire algorithm, a fact clearly observed in the fine model response which does not meet the design specification at the same displacement values. In general, MEC models can provide reasonable good approximations for given geometries and fixed dimensions. However, if position dependent responses are required, nonlinear material properties are dominant or significant size variations are performed, MEC models can become inefficient. This is also the case here. Although, the solution is closely approached, the required accuracy is not obtained.

The resulting design solution, actuator radius, translator mass and total actuator mass are given in Table 5.4. It can be observed that the translator mass, $M_{tr} = 24.38\text{kg}$, represents only 14.95% of the total actuator mass. However the total actuator mass, $M_t = 163.75\text{kg}$ is very large compared to the tubular actuator solutions obtained in Chapter 4, nevertheless, for a different force requirement. The force density and the specific force values are slightly higher than the values obtained in the previous chapter. However, these results are obtained by considering the force output for the largest displacement value of, i.e., $F|_{z=0.17} = 6.5\text{kN}$. If the force output for the middle translator position is considered, i.e., $F|_{z=0.10} = 4.4\text{kN}$, then a force density of 195.83kN/m^3 is obtained. The force versus displacement output is plotted in Fig. 5.13a. Further, by differentiating the force response with respect to the displacement, the force stiffness characteristic shown in Fig. 5.13b is obtained. Excluding the minimum and maximum displacement values, the stiffness coefficient presents deviations of more than 10% from the given specification of 30kN/m excluding the initial values.

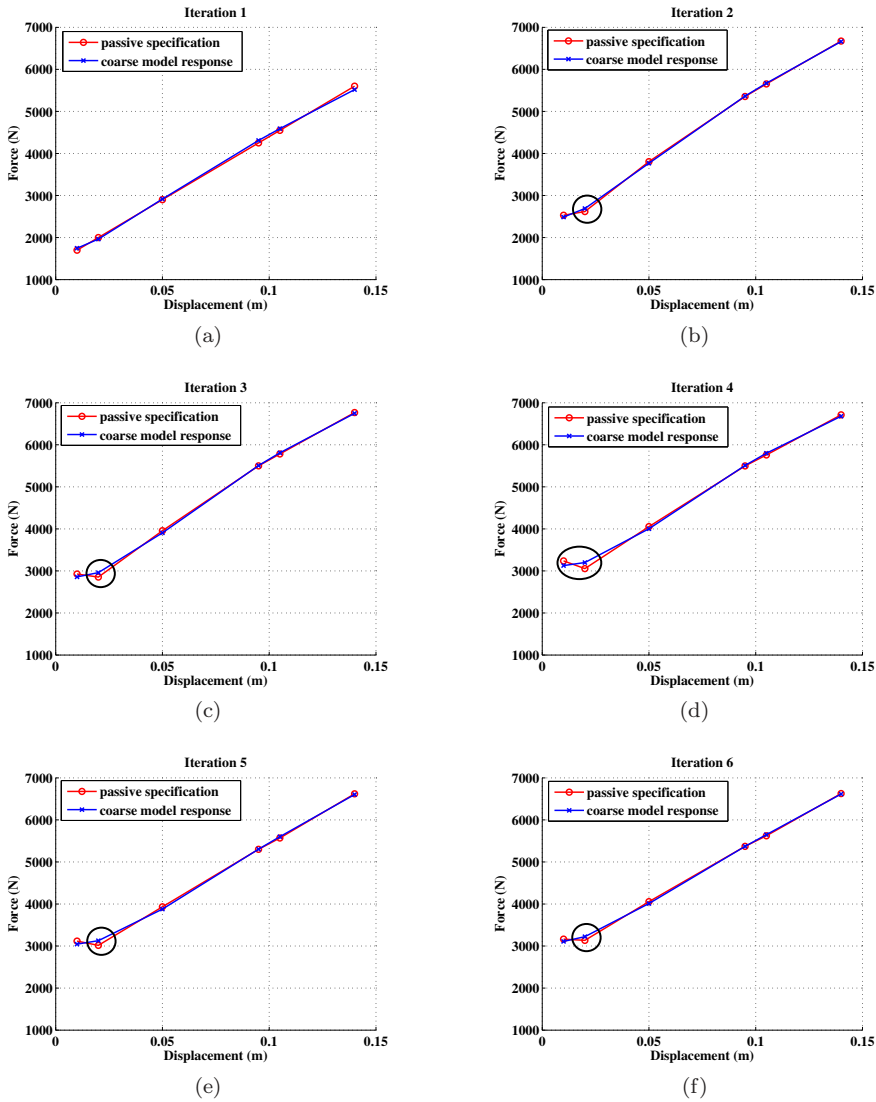


Figure 5.11: Coarse model force response compared to the coarse model specifications, where the points at which the coarse model does not match the specifications are encircled; the sub-figures (a) to (f) correspond to the coarse model force response for the AOSM iterations 1 to 6, respectively.

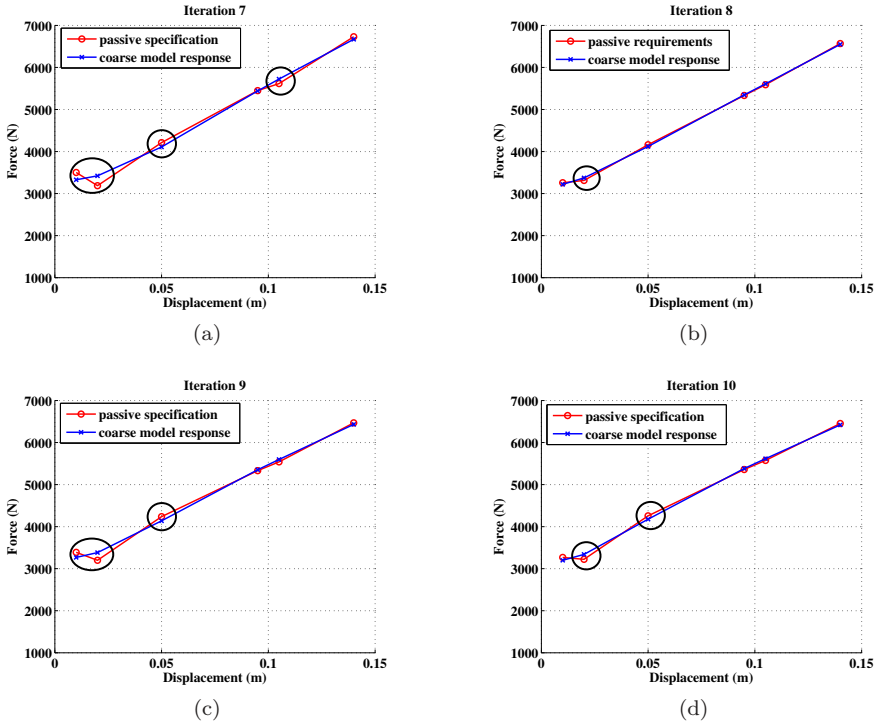


Figure 5.12: Coarse model force response compared to the coarse model specifications, where the points at which the coarse model does not match the specifications are encircled; the sub-figures (a) to (d) correspond to the coarse model force response for the AOSM iterations 7 to 10, respectively.

Table 5.4: Design variables and properties for the AOSM solution, i.e., the tenth iteration, and the result obtained at the second AOSM iteration which is chosen to derive the ELMASP prototype.

	ASOM solution	Iter. no. 2 \Rightarrow Prototype	
x_1 (mm)	41.49	39.24	36.0
x_2 (mm)	1.00	1.00	1.0
x_3 (mm)	8.23	9.91	9.9
x_4 (mm)	2.74	1.43	-
x_5 (mm)	7.29	7.99	8.0
x_6 (mm)	7.97	9.14	9.1
x_7 (mm)	8.23	9.91	-
x_8 (mm)	190.0	191.1	175.0
x_9 (mm)	12.29	13.17	13.2
x_{10} (mm)	1.00	3.66	5.2
x_{11} (mm)	9.57	11.73	13.2
x_{12} (mm)	9.56	11.73	13.2
x_{13} (mm)	2.32	5.11	6.6
x_{14} (mm)	9.56	11.73	13.2
x_{15} (mm)	4.07	3.26	13.2
x_{16} (mm)	14.09	12.54	12.5
x_{17} (mm)	8.11	8.39	12.0
x_{18} (mm)	1.22	2.85	2.9
L_a (mm)	760.0	764.3	700.0
r_a (mm)	97.10	99.85	101.7
Force density(kN/m ³)	289.3	271.5	313.9
Specific force(N/kg)	39.7	37.5	43.5
Translator mass(kg)	24.38	29.48	27.3
Total mass(kg)	163.7	173.3	164.2

An analysis of all the iterations performed reveals another set of design variables which, even though it is just an intermediate step, provides a very linear response characteristic. This set of design variables corresponds to the second iteration and the associated force response is shown in Fig. 5.13a together with the characteristic given by the AOSM solution. The force stiffness corresponding to this second response is shown in Fig. 5.13b. In spite of a characteristic which is slightly shifted down in comparison to the design specification and which is also deviated at the initial displacement point, this set of variables provides a stiffness coefficient with significantly smaller deviations for most of the stroke range.

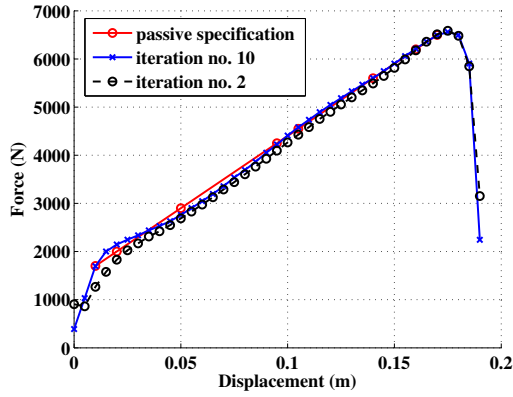
As mentioned before, a linear passive response is the primary design goal. Consequently, even though the result of the second iteration is not an optimal solution, this set of variables will be considered for further investigation instead of the actual solution. The variables and the design properties of the second iteration ELMASP configuration are given in Table 5.4. This design is used to derive the experimental prototype.

The experimental prototype is build to verify the passive response of the chosen ELMASP design. The implementation of the prototype and the results of the measurements are discussed in Section 5.5.4. Further, in Section 5.6, the design is extended by incorporating excitation coils and the active ELMASP response is investigated. Due to practical reasons related to the experimental setup and also the active design, several modifications of the passive design are introduced here.

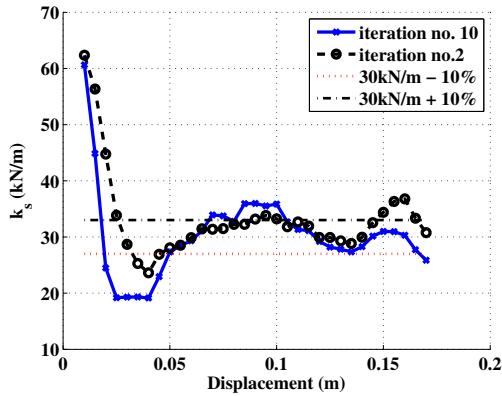
The results given in Table 5.4 show that for both lower and upper pairs of stator magnets, one of the two magnets is much shorter then the other. This may indicate that perhaps the inclusion of magnets on both inner and outer stator is not necessary. Therefore, the inner stator magnets are removed and their respective thicknesses are added to the outer stator magnets, i.e., $x_{12} = 11.73 + x_4 = 13.17\text{mm}$ and $x_{15} = 3.26 + x_7 = 13.17\text{mm}$. This design change serves two purposes:

- both stator and translator magnets have now the same thickness which allows an easier manufacturing process;
- the space made available on the inner stator will be used to implement the excitation coils for the active design in Section 5.6.

The increase of the outer stator magnet thickness leads to an increase in the outer airgap length and total radius. The distance between the stator back-iron and the mover back-plate is given by the airgap length, g , and the thicker stator



(a)



(b)

Figure 5.13: Force response (a) and force stiffness (b) comparisons between the ELMASP solutions corresponding to second and tenth AOSM iterations.

magnet. By increasing the magnet thickness, the stator teeth and back-iron are shifted by approximately 1.5mm, which leads to an increase in airgap length in the region facing the stator teeth. To compensate, the outer stator teeth length, x_{10} , x_{11} , x_{13} and x_{14} , is increased by 1.5mm.

In order to stabilize the concentric stator-translator alignment, a linear ball-bearing system is included in place of the shaft considered in the modeling of the actuator. Due to a standard dimension of the linear bearing, i.e., a radius of 12mm, the dimension of the inner stator back-iron is slightly reduced.

For ease of manufacturing, the translator back-plate has been moved to the inner side of the translator, therefore, allowing the attachment of the stator magnets on its outer surface.

A final design choice is made to reduce the total actuator length, based on the assumptions that, firstly, a smaller stroke range is necessary in practice and, secondly, the upper region of the force response will be dominated by the included bump-stop. Therefore, the pole-pitch is reduced from 191.1mm to 175mm.

The resulting prototype sizes are listed in Table 5.4. The effects of the proposed modifications are tested by means of FE analysis. Figure 5.14 shows the axial cross-section corresponding to the FE model of the prototype and the distribution of magnetic flux density for zero displacement. It can be observed that several regions of the iron core are deeply driven into magnetic saturation. The obtained force output, shown in Fig. 5.15a has shifted above the passive specification, but it still preserves its linear profile.

5.5.4 Experimental setup and measurements

A proof-of-concept prototype has been built using the set of design variables indicated in Table 5.4. The following materials have been used:

- standard mild steel for the stator and translator iron core;
- NdFeB magnets, with a remanent flux density of 1.15T;
- four sliding bearings have been manufactured to fit into the inner and outer airgaps in between the stator teeth and the translator;
- the rubber bump-stop from the BMW suspension strut analyzed in Chapter 2 has been fitted in the ELMASP.

The component parts of the prototype at different manufacturing stages are shown in Fig. 5.16. It can be observed from 5.16a and b that both stator and

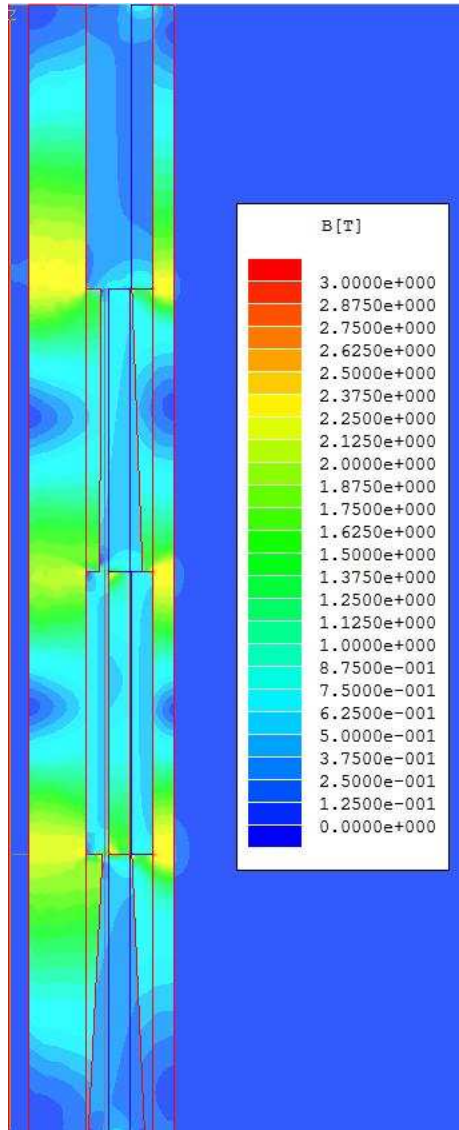
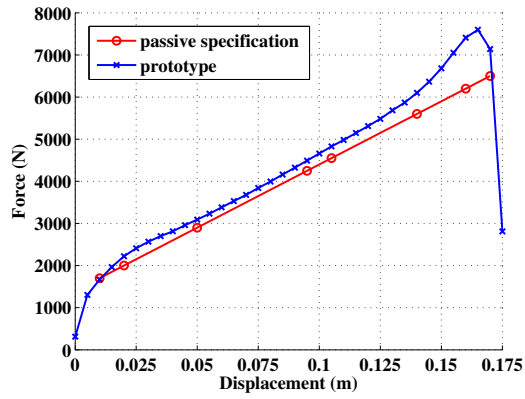
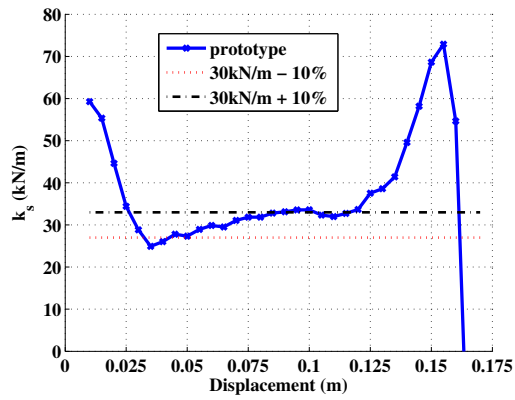


Figure 5.14: ELMASP prototype cross-section and distribution of magnetic flux density.



(a)



(b)

Figure 5.15: Simulated force response (a) and force stiffness (b) for the ELMASP prototype.

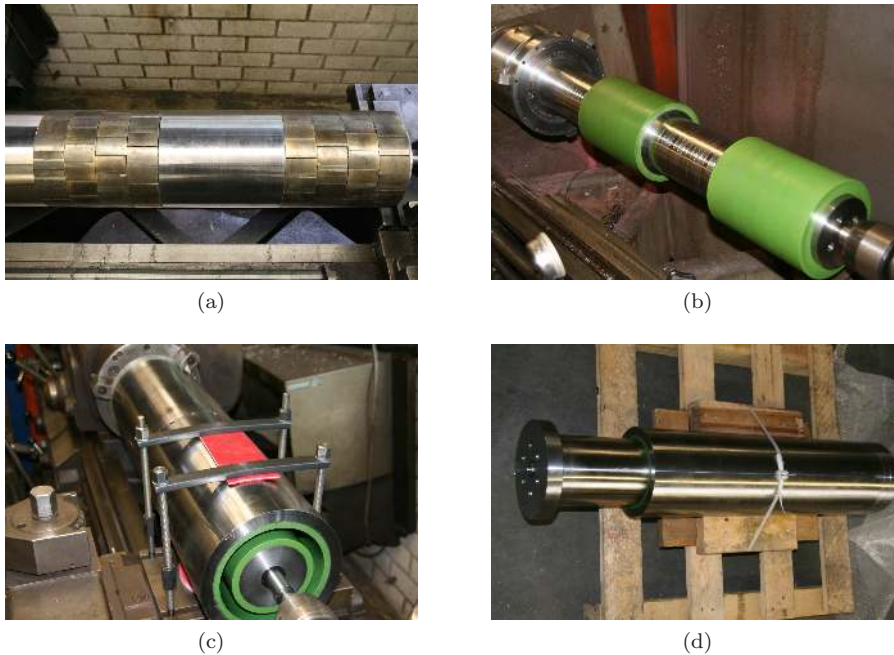


Figure 5.16: ELMASP prototype during the manufacturing process: (a) translator with segment magnets, (b) inner stator with sliding bearing, (c) assembled stator, and (d) assembled actuator.

translator magnets have been assembled from small magnet segments. This approach is based on the following considerations:

- high forces are exerted between the magnets and the iron core due the high strength magnetic material used;
- the relative high brittleness of the NdFeB material;
- difficult magnetization process of radially magnetized cylinder magnets.

The purpose of the measurements is to verify the static passive response of the ELMASP prototype. A 1-DOF force sensor, with a maximum load of 2000kg, is used in an experimental setup where the ELMASP translator is loaded with the help of a hydraulic piston (Fig. 5.17). Several measurement cycles,

i.e., from the aligned position to the maximum displacement and back, have been performed. The averages of the measured characteristics are shown in Fig. 5.18 together with the FE force response obtained in the previous section. Two significant deviations from the ideal FE curve can be observed:

- the up-stroke and down-stroke characteristics are shifted above and below, respectively, relative to the FE predicted response;
- large dips are present on both curves.

However, two expected results are also visible:

- the average of the up-stroke and down-stroke responses, given in Fig. 5.19 matches closely the simulated curve;
- excluding the large dips, the measured average presents the expected linear profile.

Furthermore, a nonlinear region at the end of the stroke appears due to the presence of the rubber bump-stop.

The causes for the above mentioned undesired effects can be identified. There are two causes which could lead to the almost symmetrical shift of the up-stroke and down-stroke responses, i.e., magnetic hysteresis and friction forces. The magnetic hysteresis has been observed also in the case of the α -ELMASP, in Section 5.1.1, nevertheless, with a very small influence on the total force output. It is more probable that the shifted responses are caused by very large friction forces in the sliding bearing. These forces can exist due to several reasons: manufacturing tolerances, a stator-translator axial or radial misalignment that causes large radial forces to appear or an unsuited bearing material or configuration, e.g., a longer a linear sliding bearing increases the probability that this occurs. This hysteresis effect, of both magnetic and mechanical nature, was a predictable occurrence, nevertheless, at a smaller scale.

The second observation, related to the large dips affecting the force response, is of higher interest because its cause can be identified in the magnetic design of the prototype. As previously mentioned, both stator and translator magnets are assembled from small magnet segments, as shown in Fig. 5.16a. Each magnet is composed of four rows of small segments, where, due to the manufacturing tolerances, a small gap is present in between these rows. Furthermore, a perturbation of the magnetization properties could be expected at the sides of the magnet segments. These two combined appear to have a significant influence on the prototype force response. It is visible in Fig. 5.18 that the force dips

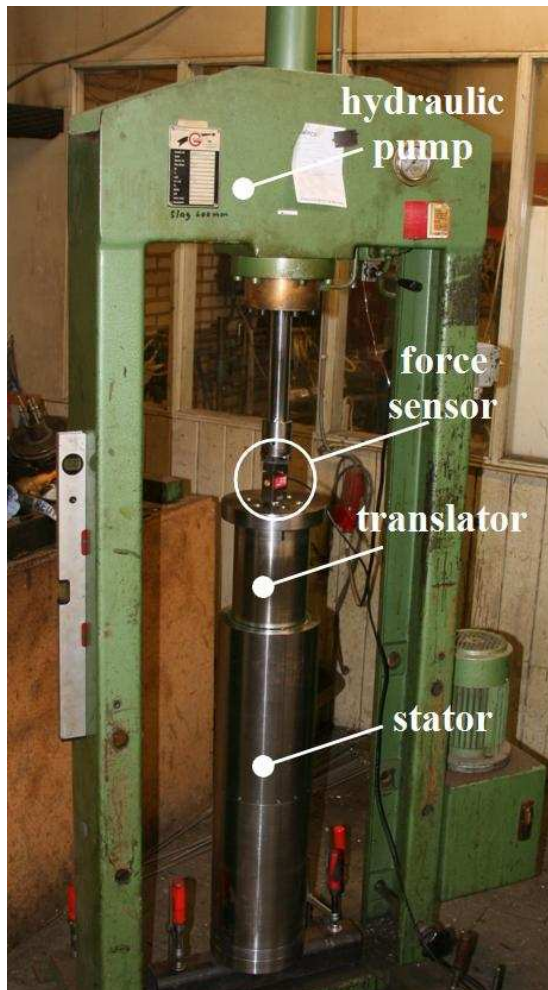


Figure 5.17: Measurements setup: a 2000kg force sensor is used to measure the ELMASP force response where a hydraulic pump provides translator load.

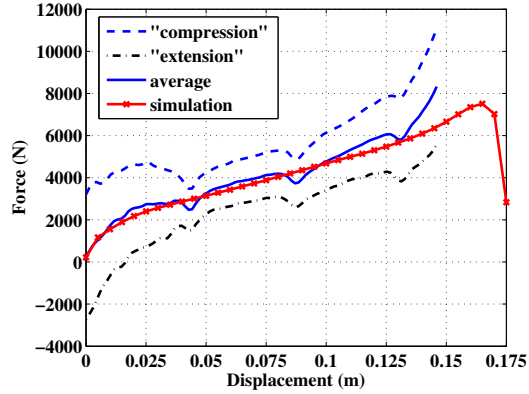


Figure 5.18: Experimental results: the up-stroke (compression), down-stroke (extension) and their average compared with the FE prototype response.

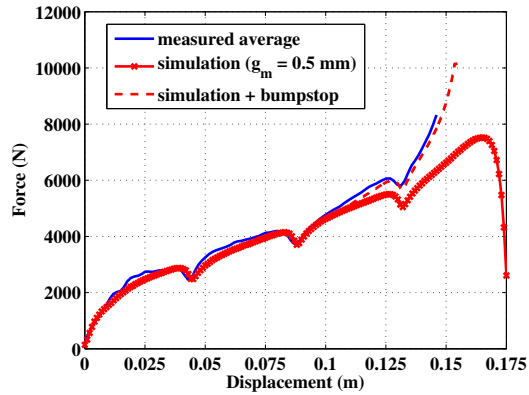


Figure 5.19: Experimental response compared to the FE response with segmented magnets and the FE response with the added bump-stop characteristic.

appear at intervals of 43.75mm which corresponds to the length of the magnet segments. In order to verify this hypothesis, the ELMASP FE model is modified to include four magnet rows separated by a gap of 0.5mm. The results obtained are shown in Fig. 5.19 and it confirms indeed the cause of the force dips. In the same figure the bump-stop characteristic is added to the FE response to obtain a closer comparison with the average of the experimental response. One possible solution to this undesired effect is the zig-zag arrangement of the magnets or any other pattern such as the skewing patterns used in linear machines. However, although these patterns will reduce the dips, it has to be verified by means of 3D FE modeling if the number of force dips, with a reduced amplitude, is not actually multiplied. Another option, and probably the preferred one, is to use only one row of long segment magnets. For this approach, a dedicated assembling equipment might be necessary due to the much higher chance for the magnets to be damaged.

Even though significant disturbances of the prototype force response have been observed, their causes can be identified and they can be eliminated in a future setup. Therefore, it can be concluded from this section that the experimental results confirm the predicted high passive force level and linear behavior of the ELMASP concept. Before advancing to the active design, a transient response of the passive design can be verified, i.e., the amplitude of the eddy-current damping.

5.5.5 Passive eddy-current damping

The translator displacement causes a variation of the magnetic flux density within both stator and translator. According to Faraday's law of electromagnetic induction, electromotive forces are induced by a varying magnetic flux, which leads to the appearance of closed-loop currents, or eddy-currents, within the conductive materials, i.e., iron-core and magnets. The direction of the eddy-currents is such that the generated magnetic field opposes the change of the original field. Consequently, the interaction of the two magnetic fields generates a repulsion force which opposes to the translator movement. The amplitude of the repulsion force is dependent on the speed of movement of the translator, which resembles a damping force characteristic.

The generation of damping forces due to the eddy-current phenomenon presents both advantages and disadvantages. An advantage is that a passive damping force is always present, even in the case of a power failure, and a disadvantage is the limitation of the dynamic performance of the actuator. To evaluate the eddy-current damping, two time-dependent FE simulations are per-

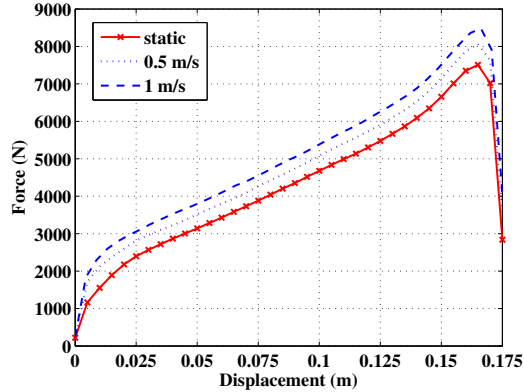


Figure 5.20: Damping forces caused by the eddy currents at 0.5m/s and 1m/s compared to the static force response.

formed for translator speeds of 0.5m/s and 1m/s. The results are shown in Fig. 5.20 together with the passive response for comparison. The actuator response is shifted by approximately 400N at 0.5m/s and 700N at 1m/s. The second value shows that about one third of the nominal damping force, i.e., 2000N at 1m/s, is passively provided and the remaining force range has to be actively provided.

5.6 Active design

The obtained passive design provides the spring characteristic necessary for the support of the vehicle weight and added load. Therefore, a design extension is necessary in order to incorporate excitation coils to provide an additional force component for active vibration and roll compensation. The coils can be integrated in the space available on the inner stator since the magnets have been removed in the prototype design. A detailed view of the lower inner stator slot is given in Fig. 5.21. Two coils, carrying an excitation currents with opposite orientations, are placed in the slot in order to add a positive or negative MMF contribution to the main flux paths, i.e., to strengthen or weaken the main magnetic flux, thus, varying the force output of the ELMASP.

A series of FE simulations obtained for a varying coil width, c_w , at a fixed

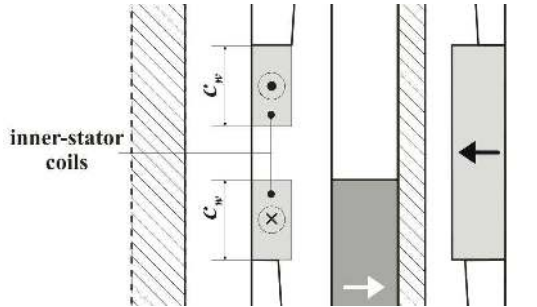


Figure 5.21: The inner-stator magnet is replaced by two excitation coils with fixed width.

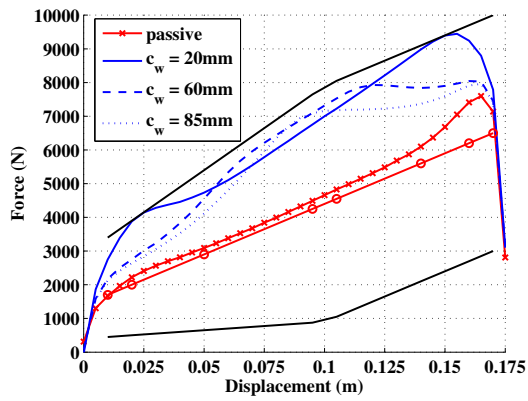


Figure 5.22: Influence of the coil width over the active force response.

current amplitude, are shown in Fig. 5.22. The figure clearly indicates that the ELMASP response can be shifted in both negative and positive directions. However, the active force response presents a very non-linear profile where the amplitude of the force response varies significantly. It could be concluded that, in order to obtain a constant shift of the force response as a function of displacement for a given coil width, a position dependent current amplitude should be used. Furthermore, the rather large amplitude variations of the active responses indicate that the amplitude of the excitation current, for a given curve, would be also characterized by large position dependent variations.

Nevertheless, an important additional observation can be extracted from Fig. 5.22, i.e., the peaks of the active force characteristics are directly dependent on the coil width and they occur at displacements values equal to the coil width. In other words, a maximum force value is achieved at a translator displacement value where the upper edge of the stator magnets 'intersect' the edges of the stator coils, as shown in Fig. 5.21. This effect is given by the fact that the highest field gradients exist at the coil and magnet edges and, therefore, the highest magnetic energy gradient as a function of translator position, which translates into a peak force, is found at this particular relative displacement. This observation suggests that a relatively constant shift of the force response could be obtained with a displacement dependent coil width.

5.6.1 Novel design of commutated coils for active ELMASP response

Following from the above observation, a novel design configuration of the excitation coils, for which an international patent [93] has been issued, is proposed in this section. As shown in Fig. 5.23a, the two coils are completely filling the stator slot and their are assigned complementary dimensions, i.e., $c_l + c_u = x_8$. Further, in the ideal case the width of the lower coil in the slot is equal to the translator displacement, i.e.,

$$\begin{aligned} c_l &= d, \\ c_u &= x_8 - d. \end{aligned} \tag{5.16}$$

This coil configuration is implemented in the ELMASP FE model and the corresponding simulation results, where the coil current density is varied between $-20\text{A}/\text{mm}^2$ and $+20\text{A}/\text{mm}^2$ and a slot filling factor of 0.5 is assumed, are shown in Fig. 5.24. Compared to the results from Fig. 5.22, the varying width coils provide a significantly improved active response considering that, especially for lower current densities, the active response presents a linear shift relative to the passive response. The nonlinear effects which affect the force output for higher current density values are caused by the nonlinear material properties of the

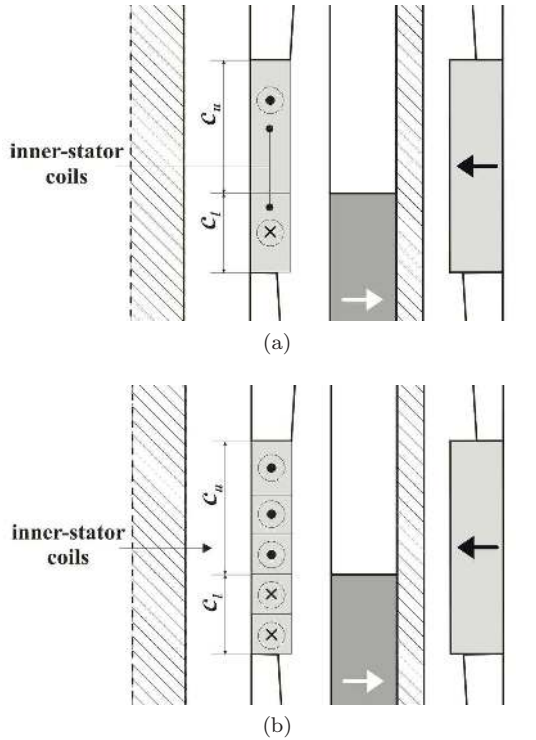
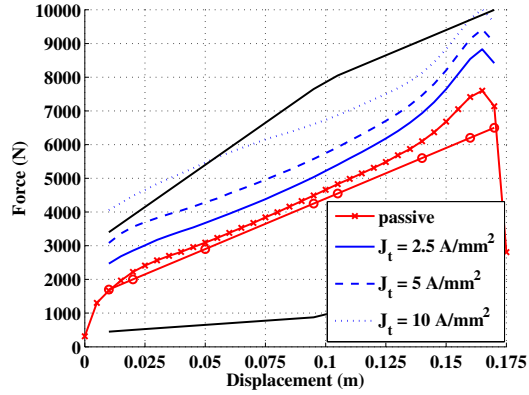


Figure 5.23: Novel coil geometry: (a) the ideal configuration in which the coil width varies continuously with the displacement, and (b) a commutated multi-coil configuration for the practical implementation.

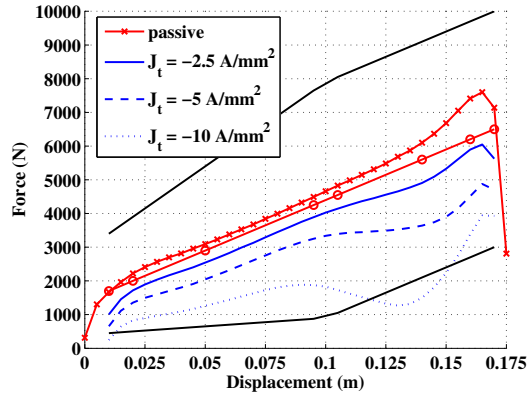
iron-core.

However, a continuously varying coil width is only an idealized solution. Therefore, for practical implementations, a multi-coil configuration with an associated commutation scheme is proposed. Such an arrangement is shown in Fig. 5.23b where a set of seventeen coils are proposed. The switch of the current direction is realized when the translator upper edge overlaps the upper edge of a coil. This multi-coil configuration introduces a saw-tooth ripple of the force output, as shown by Fig. 5.25. An increased number of coils leads to decreased ripple amplitude, but an increased ripple frequency.

Given the opposite magnetization direction of the stator and translator mag-

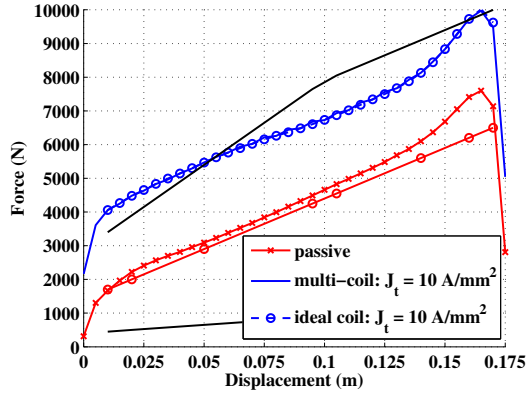


(a)

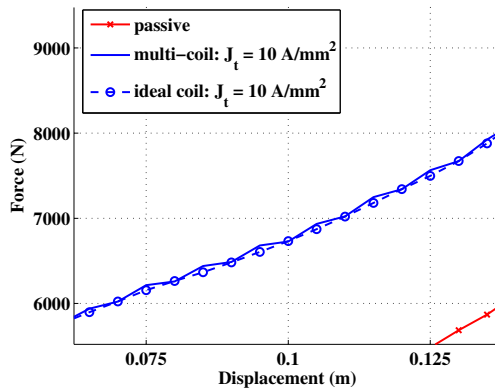


(b)

Figure 5.24: ELMASP force response for a continuously varying coil width configuration for (a) positive and (b) negative current excitation with different values of current density.



(a)



(b)

Figure 5.25: Comparison between the response for the ideal coil and the multi-coil configuration: (a) the force response for the entire displacement range, (b) detailed view in which the saw-tooth ripple, introduced by the multi-coil configuration, is visible.

nets, a potential risk of permanent demagnetization exist. The addition of excitation coils increases even further this risk. Therefore, by means of the ELMASP FE model the demagnetization risk is investigated in the following section.

5.6.2 Demagnetization verification

The risk of demagnetization is assessed by investigating the strength of the demagnetizing fields. Four situations are discussed, i.e., the demagnetizing field for partially and fully overlapped magnets is calculated for both the passive and active regimes. The distribution of field strength vector, for a pair of stator and translator magnets, for the passive regime in Fig. 5.26 and for the active regime in Fig. 5.27.

The BH-characteristic of the used NdFeB magnets, given in Appendix C, is used as a reference. At ambient temperature, irreversible demagnetization occurs if the amplitude of the demagnetizing field reaches -1390kA/m . This places the so-called knee of the BH-characteristic well within the third quadrant. In the passive regime, the overlapping magnets are canceling each other's fields. A value of the demagnetizing field of approximately -900A/m indicates that the magnetic flux density is zero. In the active regime, although a stronger demagnetizing field affects the stator magnet and the operating point is within the third quadrant, the values are still lower than the demagnetization threshold. However, due to a possible temperature rise in the active regime, the value of the demagnetization threshold can decrease significantly and irreversible demagnetization may occur. Therefore, a thorough investigation of thermal design and management for the ELMASP has to be undertaken. However, noting that the obtained design solution does not satisfy the geometrical constraints defined in Section 2.5, this investigation is not further considered in this thesis. An improvement of the obtained electromagnetic design, considering also topological modifications, for an even higher force density is necessary before addressing the issues related to the power supply requirements and thermal management.

5.7 Conclusions and remarks

A novel electromagnetic spring topology is introduced in this chapter. The proposed topology is based on a double airgap configuration and is characterized by both a passive response, which mimics the behavior of a mechanical spring, and an active regime necessary for vehicle body-roll control and vibration compensation.

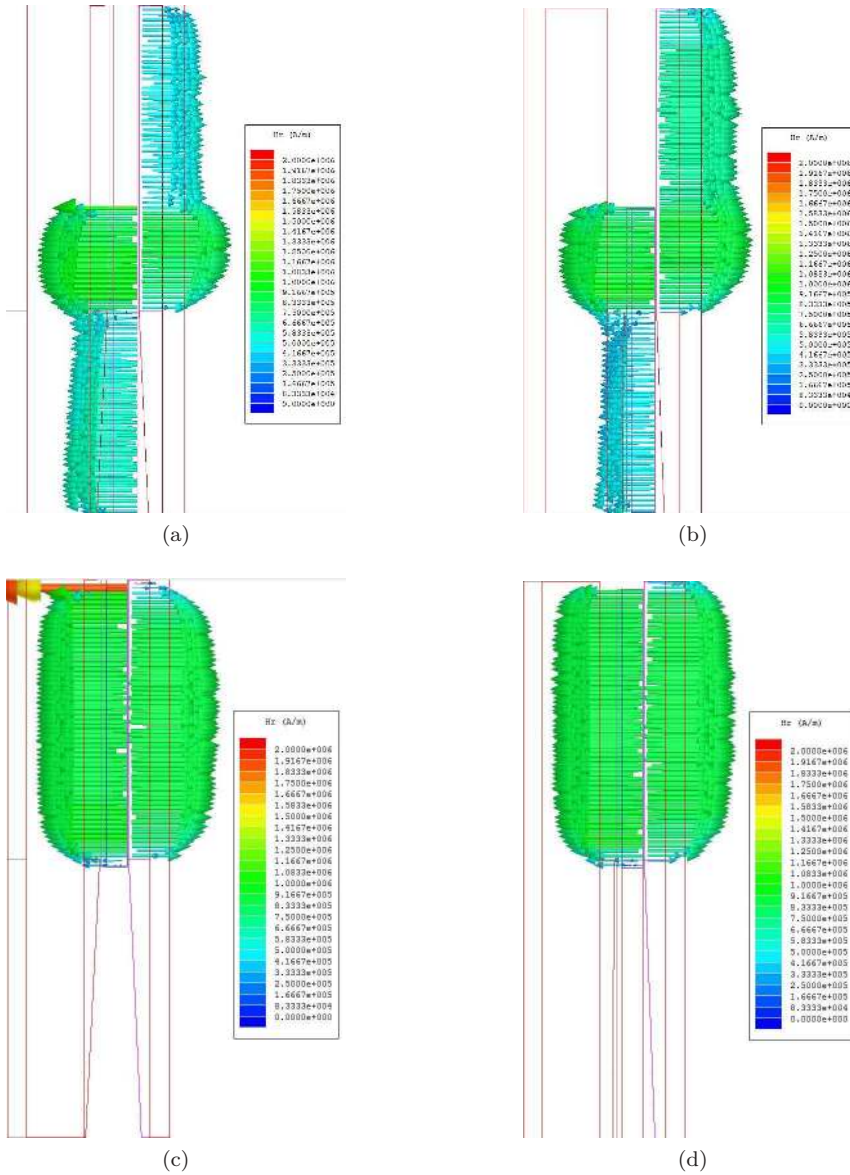


Figure 5.26: Demagnetizing field in the passive regime: (a) partially overlapping lower magnets, (b) partially overlapping upper magnets, (c) fully overlapping lower magnets, and (d) fully overlapping upper magnets.

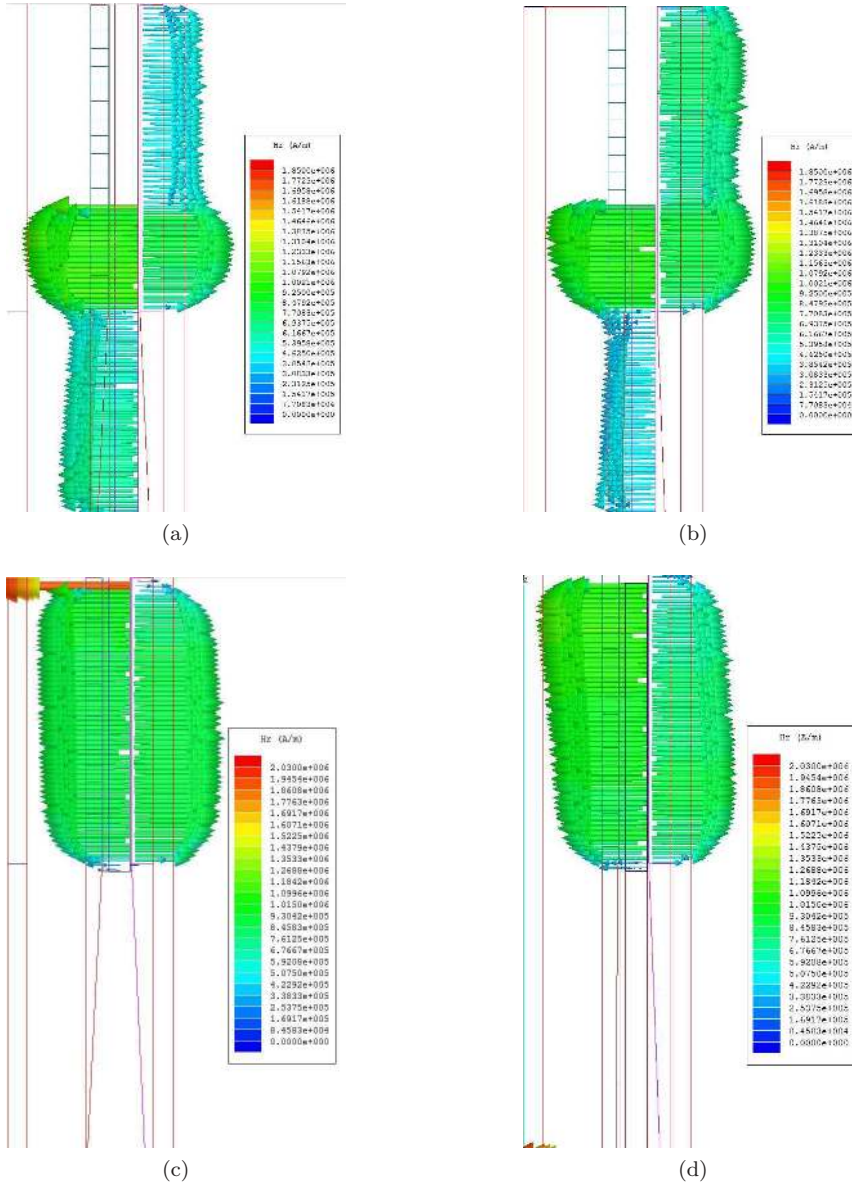


Figure 5.27: Demagnetizing field in the active regime: (a) partially overlapping lower magnets, (b) partially overlapping upper magnets, (c) fully overlapping lower magnets, and (d) fully overlapping upper magnets.

AOSM-based optimization has been employed to derive the passive design concept. However, the obtained design solution does not satisfy the geometrical requirements listed in Section 2.5. An experimental prototype has been built and the predicted passive linear response has been confirmed. Furthermore, a novel coil configuration that provides the required active response has been proposed.

The novelty of the proposed ELMASP is given by its non-repetitive geometrical configuration with sloped stator teeth, the linear passive response for a stroke range of 0.175m with a stiffness of 30kN/m and a peak force of 6.5kN, and the commutated coil which provides a constant shift of the force profile for a constant excitation current, independent of the translator position. Two international patents have been issued to cover the innovative passive and active design concepts.

6

Conclusions and recommendations

A novel actuator topology for a fully electromagnetic active suspension solution that can provide both a zero-power spring characteristic and actuation forces necessary for vibration damping and vehicle body-roll control has been proposed in this thesis. No other single actuator solution with these characteristics has been investigated in the literature up to this moment. The proposed electromagnetic spring (ELMASP) is aimed at replacing both spring and damper in a suspension strut. Two international patents have been issued to cover the innovative passive and active design concepts. A design solution for the new actuator topology was obtained by means of a multi-level optimization approach, i.e., space-mapping (SM). The predicted passive linear spring characteristic has been confirmed by means of an experimental prototype.

An alternative hybrid configuration, consisting of an existing type of tubular linear actuator connected in parallel with a mechanical spring has also been investigated. The obtained results indicate that the considered slotted tubular PM actuator can fulfill the specified requirements.

Prior to the work related to this thesis only one publication [24] has considered the SM technique for the design of an electromagnetic actuator, therefore, an overview of the SM optimization technique and publications resulted from the framework of this thesis has been presented.

The general conclusions and recommendations are organized according to the thesis objectives outlined in Section 1.5. Further developments of the design concept proposed in this thesis are suggested in the final recommendations.

6.1 Space-mapping optimization

The SM optimization techniques allow time-efficient optimization of complex physical models. This is achieved by replacing a time expensive model, denoted as a fine model, with a surrogate given by a mapped coarse model. A coarse model is a simplified physical model with a negligible evaluation time. An iteratively improved mapping function is introduced to correct for the misalignment between coarse and fine model responses. Fundamental aspects of SM optimization together with an overview of the existing techniques and design examples have been presented.

Parameter extraction is an essential subproblem of any input SM algorithm. It is used to align the surrogate with the fine model at each iteration, however, the failure of this step impedes the convergence of the algorithm. Implicit or output mappings, which can be derived from the available sets of coarse and fine model responses without the necessity for an additional parameter extraction subproblem, are recommended whenever possible. However, a parameter extraction step may be required in one of the following situations: (1) if the sets \mathbf{Z} and \mathbf{X} do not coincide, an additional input mapping, $\mathbf{p} : \mathbf{X} \rightarrow \mathbf{Z}$, can be introduced or (2) if a significant coarse-fine model misalignment impedes the convergence of an output mapping based algorithm then the coefficients of an additional input or implicit mapping can be determined through parameter extraction.

SM convergence is strongly conditioned by the properties of the chosen coarse model. If the nonlinearity of the fine model is reflected in the coarse model then the (input/output/implicit) mapping is expected to involve a reduced nonlinearity [39]. Hence, a good mapping approximation can be found within a reduced number of iterations. Moreover, this is why SM can exhibit a faster convergence than that of classical algorithms where, for example, linear or quadratical surrogates are employed to directly approximate the nonlinear fine model, hence necessitating an increased number of algorithm iterations. Consequently, a *good* coarse model is necessary to assure the convergence and efficiency of an SM algorithm. Mathematical guidelines for estimating the quality of a coarse model have been recently proposed in [94].

A new algorithm variant, i.e., the aggressive output space-mapping (AOSM),

is proposed in this thesis and has been verified in a number of publications. The AOSM is derived as an inverse OSM formulation. It employs a linear mapping constructed with an approximate Jacobian and can be categorized as a special case of GMM. The AOSM has been successfully employed for the design problems studied in this thesis. Furthermore, a general scheme for SM implementation has been proposed.

Several publications, which prove the efficiency of SM optimization compared with various standard optimization algorithms, have resulted in the framework of this thesis.

6.2 The tubular linear actuator solution

A tubular, slotted, radially magnetized, PM actuator is considered as being integrated in a hybrid active suspension solution where the mass of the vehicle is sustained by mechanical springs. Such configurations have been previously proposed in the literature. The Bose system [2] is supposed to have a similar configuration. However, no commercial solution exists up to this moment.

A number of actuator configurations have been obtained by means of AOSM optimization, i.e., fundamental sizes and stator configuration in terms of the number of pole-pairs. Several of these designs satisfy the imposed geometrical constraints and can fit into the same space as the current mechanical suspension. Static and dynamic characteristics, e.g. total and cogging force response, back-EMF and damping force caused by eddy-currents have been investigated. The cogging force reduction by means of magnet skewing techniques has been discussed.

However, because the obtained configurations are pre-design solutions, complete electromagnetic and mechanical design methodologies have to be undertaken. The outcome of this thesis helps to emphasize the advantages brought in by the SM-based optimization algorithm, i.e., a large number of (pre-)design solutions can be obtained with a reduced computational effort, and provides an assessment of the suitability of the tubular PM actuator solution.

6.3 The novel electromagnetic spring

The synthesis and design of a new actuator topology for a full electromagnetic suspension solution has been the main focus of this thesis. Such an actuator provides both a passive regime which mimics the behavior of a mechan-

ical spring, and an active regime necessary for vibration damping and vehicle body-roll control. The corresponding design requirements, e.g., linear passive response characteristic, high force output and volumetric constraints, lead to a very challenging design problem. The investigation of an existing pre-prototype concept showed that a redesign is necessary in order to obtain a significantly increased force density, thus, reducing the outer dimensions of the actuator. A novel design is derived in this thesis by considering the following:

- a double stator (double airgap) configuration with an extended stator length which includes both iron teeth and magnets;
- a translator composed of two magnets interconnected by an iron element.

Firstly, the passive design is undertaken by means of AOSM shape-optimization, where MEC and FE models are employed as coarse and fine models, respectively. The algorithm approached a design solution within the first iterations, however, the pre-defined accuracy criterion has not been entirely satisfied. The causes for this convergence behavior can be identified in the limitations of the chosen MEC model. Nevertheless, a sub-optimal solution which provides a linear passive response has been identified and used to obtain an experimental prototype. The experimental measurements have validated the predicted passive force response. The uniqueness of the proposed actuator topology is given by its non-repetitive geometrical configuration with sloped stator teeth, and the linear passive response for a stroke range of 0.175m with a stiffness of 30kN/m and a peak force of 6.5kN.

Secondly, the passive design has been extended with the inclusion of stator excitation coils. A novel commutated multi-coil configuration provides a constant shift of the force profile for a constant excitation current, independent of the translator position. Therefore, the force envelope, introduced as a design specification, can be fully covered.

6.4 Thesis contributions

The major contributions and output of this thesis can be summarized as follows:

- identification of the SM applicability to the design of electromagnetic actuators; prior to the work related to this thesis only one publication [24] has considered the SM technique for the design of an electromagnetic ac-

tuator; consequently, the list of publications resulted from the framework of this thesis brings a real contribution to the current state-of-art;

- a new algorithm variant and an SM implementation scheme for applications in electromagnetic design;
- SM-based size optimization of a known topology of tubular PM actuator as a solution for automotive active suspension;
- a novel short-stroke electromagnetic spring topology for automotive active suspension and experimental validation of the predicted passive force response;
- contribution and direct initiation of two international patents;
- seven peer-reviewed journal publications;
- sixteen conference publications.

6.5 Recommendations for future research

6.5.1 Space-mapping and coarse models

The coarse model is at the same time one of the key SM ingredients and a major cause for algorithm failure. All the numerical examples and design problems studied in the framework of this thesis, show that MEC models are a rather good coarse model choice when a static physical device, i.e., both from time and position point of view, is concerned. For such situations, the resulting MEC models are very simple and have a negligible evaluation time. However, MEC models provide only a locally restricted validity because of the designer pre-defined flux paths, which makes these models rather unsuited for optimization problems defined on a large domain that can lead to significant modifications of the geometrical configuration of the concerned physical device. Furthermore, MEC models become unsuited in situation where the nonlinear material properties, e.g., iron core magnetic permeability, have dominant effects. Therefore, it is advisable for other coarse model choices, e.g., analytical or semi-numerical, to be considered when available. In rather extreme situations, the time efficiency of an SM technique can be canceled by the time required to tune an unsuited coarse model.

6.5.2 Redesign of the electromagnetic spring

The electromagnetic spring design proposed in this thesis shows that it is possible to combine a linear passive characteristic and an active response within one electromechanical device. However, the obtained configuration is only a proof-of-concept and not a feasible alternative to the current active suspension solutions. An improvement of this concept is necessary. This can be achieved by considering different basic topologies, i.e., the material distribution and, perhaps, an unconventional ratio between the volume of soft- and hard- magnetic materials. In this respect, topology optimization, instead of shape optimization, could be considered as a design tool.

6.5.3 The future electric car

Given the imminent depletion of the oil resources, the continuous increase in oil prices and the ever increasing awareness regarding the alternative renewable energy sources, there is strong global trend nowadays towards the introduction of fully electric passenger vehicles. The electromagnetic active suspension should not be viewed anymore only as an option of current luxury vehicles, but as an intrinsic component of the future highly efficient electric vehicle. A vision of the not so far future, indicates that the electromagnetic active suspension will be fully integrated into the total car system, as both an active safety system and a component in the vehicle energy-recuperation system.

A

List of symbols and abbreviations

A.1 Symbols

<i>Symbol</i>	<i>Quantity</i>	<i>Unit</i>
α_k	step size	-
α_k, β_k	coefficients	-
γ	roll force distribution	-
δ_r	diameter of the trust-region	-
δ_z	skew angle	el. deg.
$\boldsymbol{\eta}_k$	preassigned model parameters	-
μ, ν	penalty multipliers	-
μ_0	magnetic permeability of vacuum	H/m
μ_{rc}	recoil magnetic permeability	-
ρ_k	quality coefficient for a trust-region step	-
ρ	mass density	kg/m ³
σ	airgap shear stress	N/m ²
φ	roll angle	rad
ϕ	auxiliary merit function	-
Φ_m	main magnetic flux	Wb

Φ	vector of unknowns in the MEC model	-
ψ_m	ratio of the body mass acting on the front axle	-
a	acceleration	m/s ²
A_φ	circumferential component of the magnetic vector potential	Wb/m
\mathbf{A}, \mathbf{b}	linear constraints	-
A, B, C, D, \dots	matrices for the state-space representation	-
X, Y, V		
B	magnetic loading	T
B	magnitude of the magnetic flux density	T
\mathbf{B}_k	Jacobian approximation	-
\mathbf{c}	coarse model	-
C	force ratio between the wheel mount and the actuator	-
c_w, c_l, c_u	coil width	m
d	displacement	m
d_k	search direction	-
d_p	power duty cycle	N
d_s	damper coefficient	Ns/m
\mathbf{f}	fine model	-
\mathbf{f}	source vector in the MEC model	-
f_m	permanent magnet MMF	-
\mathcal{F}	objective function	-
\mathcal{F}_{pen}	objective function augmented with penalty terms	-
F_{act}	actuator force	N
$F_{anti-roll_{max}}$	maximum anti-roll force	N
F_{bump}	damper bump force	N
F_{dyn}	dynamic vertical roll force	N
F_{max}	maximum force	N
F_{mean}	mean force	N
F_{ra}	force due to the rolling tendency of the sprung mass around the vehicle roll-axis	N
$F_{rebound}$	damper rebound force	N
F_{RMS}	RMS force	N
F_s	force due to the rolling tendency of the sprung mass around its own center of gravity	N
F_{stat}	static vehicle weight	N

f_u	resonant frequency of the unsprung mass	Hz
f_s	resonant frequency of the sprung mass	Hz
$F_{s_{nom}}$	nominal static force	N
F_{tv}	force per translator volume	N/m ³
F_u	force due to the rolling tendency of the unsprung mass around its own center of gravity	N
F_y	guiding force along y -axis	N
F_z	net force along z -axis	N
g	airgap length	m
g_i	nonlinear inequality constraints	-
h_c	convection coefficient	W/(m ² K)
H_{CoG}	height of the vehicle center of mass	m
H	Hessian matrix	-
h_k	step length	-
h_i	nonlinear equality constraints	-
H_u	height of the unsprung center of mass	m
H_s	height of the sprung center of mass	m
I	set of positive integers	-
I	RMS current	-
$I_{n_{pp}}^{eq}$	total equivalent current per pole-pair	A
I_p	peak current	A
J	Jacobian matrix	-
J_p	peak current density	A/m ²
\mathbf{k}_c	coarse model nonlinear equality and inequality constraints	-
\mathbf{k}_f	fine model nonlinear equality and inequality constraints	-
$k_{support}$	support spring stiffness	N/m
$k_{rebound}$	rebound spring stiffness	N/m
k_s	spring stiffness	N/m
k_u	tire stiffness	N/m
l_1, l_2	types of penalty functions	-
\mathbf{l}_k	linear approximation of the residual function \mathbf{r}	-
L_a	actuator length	m
L_{se}	length of stator ends	m
L_{st}	stator length	-
L_t	maximum actuator axial length	m

m_k	approximate model	-
m_s	total sprung mass	kg
m_{sq}	quarter-car sprung mass	kg
m_{tot}	total vehicle mass	kg
M_t	total actuator mass	kg
M_{tr}	translator mass	kg
m_u	total unsprung mass	kg
m_{uq}	quarter-car unsprung mass	kg
n_l	number of layers	-
n_{pp}	number of pole-pairs	-
n_z	number of conductors	-
Ni	ampere-turns	A·t
\mathbf{o}	output space-mapping function	-
p	positive integer	-
\mathbf{p}	input space-mapping function	-
\mathbf{P}	penalty function	-
P_{Cu}	copper loss	W
Q	electric loading	A/m
\mathbf{r}	residual function	-
\mathcal{R}	magnetic reluctance	H ⁻¹
r_a	actuator outer radius	m
r_g	airgap radius	m
r_t	maximum actuator outer radius	m
\mathbf{R}	system matrix for the MEC model	-
\mathbb{R}	set of real numbers	-
s	stroke	m
\mathbf{s}	manifold-mapping function	-
S_a	outer stator surface	m ²
\mathbf{t}	aggressive output space-mapping function	-
T	track width	m
T_a	ambient temperature	°C
T_p	peak temperature	°C
T_{rv}	torque per rotor volume	Nm/m ³
T_{sk}	skew transformation	-
u_i, v_j	Lagrange multipliers	-
v	velocity	m/s
V_s	active volume	m ³
V_{tr}	translator volume	m ³
w	road irregularities	m

w_k	weighting coefficients	-
W'	magnetic co-energy	J
x_{low}	lower boundary for the design variables	-
x_{up}	upper boundary for the design variables	-
\mathbf{x}	fine model design variables	-
\mathbf{x}^*	fine model solution	-
$\bar{\mathbf{X}}$	feasible region	-
$\bar{\mathbf{X}}_\varepsilon$	subset of the feasible region	-
\mathbf{x}_{aosm}^*	aggressive output space-mapping solution	-
\mathbf{x}_d^*	dual space-mapping solution	-
\mathbf{x}_p^*	primal space-mapping solution	-
\mathbf{x}_{osm}^*	output space-mapping optimal solution	-
\mathbf{x}_{sm}^*	input space-mapping optimal solution	-
x, y, z	cartesian coordinates	-
\mathbf{X}, \mathbf{Z}	compact subsets	-
\mathbf{y}	set of design specifications	-
y_{sk}	skewed waveform	-
y_{usk}	unskewed waveform	-
\mathbf{z}	coarse model design variables	-
\mathbf{z}^*	coarse model solution	-
z	displacement along z -axis	m
\dot{z}	speed along z -axis	m/s
\ddot{z}	acceleration along z -axis	m/s ²

A.2 Abbreviations

cpl	coupled problem
lc	linear constraints
lv	local validation
nc	nonlinear constraints
qN	quasi-Newton
uc	unconstrained
ABC	Active Body Control
ARC	Active Roll Control
ASM	aggressive space-mapping
AOSM	aggressive output space-mapping
BFGS	Broyden-Fletcher-Goldfarb-Shanno
CA	coreless actuator

CFA	constant force actuator
CVCA	cylindrical voice coil actuator
DHS	Dynamic System Handling
DOF	degree of freedom
ELMASP	electromagnetic spring
EMF	electromotive force
EPF	exterior penalty function
ER	electro-rheological
FE	finite element
GMM	generalized manifold-mapping
HASM	hybrid aggressive space-mapping
ISM	implicit space-mapping
KKT	Karush-Kuhn-Tucker
MEC	magnetic equivalent circuit
MM	manifold-mapping
MMA	method of moving asymptotes
MMF	magnetomotive force
MR	magneto-rheological
NMS	Nelder-Mead simplex
OMM	original manifold-mapping
OPSM	output polynomial space-mapping
OSM	output space-mapping
PE	parameter extraction
PeM	penalty method
PM	permanent magnet
RVCA	rectangular voice coil actuator
SLP	sequential linear programming
SM	space-mapping
SMIS	space-mapping interpolating surrogate
SQP	sequential quadratic programming
SUMT	sequential unconstrained minimization techniques
THD	total harmonic distortion
TPMA	tubular permanent magnet actuator
TR	trust-region
TRASM	trust-region aggressive space-mapping
TRMM	trust-region manifold-mapping
TRSSM	trust-region surrogate space-mapping
VDA	Verband Der Automobilindustrie
VIMS	visually induced motion sickness

B

Magnetic equivalent circuit models

B.1 MEC model from Section 4.2

The expressions of the reluctance elements and MMF sources are the following:

$$\mathcal{R}_1 = \frac{\frac{2}{3} \frac{L_{st}}{n_{pp}}}{\mu_0 \mu_r 2\pi 0.5 (r_g - x_3)^2},$$

$$\mathcal{R}_2 = \frac{x_3}{\mu_0 2\pi (r_g - 0.5x_3) \frac{L_{st}}{2n_{pp}}},$$

$$\mathcal{R}_3 = \frac{g}{\mu_0 2\pi r_g \frac{L_{st}}{2n_{pp}}},$$

$$\mathcal{R}_4 = \frac{0.8(r_a - r_g)}{\mu_0 \mu_r 2\pi (r_g + 0.5x_4) \frac{L_{st}}{6n_{pp}}},$$

$$\mathcal{R}_5 = \frac{\frac{2}{3} \frac{L_{st}}{n_{pp}}}{\mu_0 \mu_r 2\pi \left(r_a - \frac{0.2(r_a - r_g)}{2} \right) 0.2(r_a - r_g)},$$

$$f_m = x_3 \frac{B_r}{\mu_0}.$$

B.2 MEC model from Section 4.3.2

The following system matrix and source vector are associated to the MEC circuit from Fig. 4.11:

$$\mathbf{R} = \begin{pmatrix} 1 & -1 & -1 & 0 & 0 & 0 & 0 & 0 & 0 & 0 & 0 & 0 \\ 0 & 0 & 1 & 0 & 0 & 0 & 0 & 0 & 1 & 0 & -1 & \\ -1 & 0 & 0 & 0 & 0 & 0 & 0 & 0 & 0 & 1 & 1 & \\ 0 & 1 & 0 & -1 & -1 & 0 & 0 & 0 & 0 & 0 & 0 & 0 \\ 0 & 0 & 0 & 0 & 0 & 1 & 0 & -1 & -1 & 0 & 0 & \\ 0 & 0 & 0 & 0 & 0 & 0 & 1 & 1 & 0 & -1 & 0 & \\ \mathcal{R}_{e1} & 0 & \mathcal{R}_5 & 0 & 0 & 0 & 0 & 0 & 0 & 0 & 0 & \mathcal{R}_5 \\ 0 & \mathcal{R}_{e2} & -\mathcal{R}_5 & 0 & \mathcal{R}_7 & 0 & 0 & 0 & \mathcal{R}_6 & 0 & 0 & \\ 0 & 0 & 0 & 0 & 0 & 0 & 0 & -\mathcal{R}_7 & \mathcal{R}_6 & -\mathcal{R}_{e2} & \mathcal{R}_5 & \\ 0 & 0 & 0 & \mathcal{R}_{e3} & -\mathcal{R}_7 & \mathcal{R}_8 & 0 & 0 & 0 & 0 & 0 & \\ 0 & 0 & 0 & 0 & 0 & \mathcal{R}_8 & -\mathcal{R}_{e3} & \mathcal{R}_7 & 0 & 0 & 0 & \end{pmatrix}$$

and

$$\mathbf{f} = (0 \ 0 \ 0 \ 0 \ 0 \ 0 \ 0 \ f_1 \ f_2 \ f_3 \ f_2 \ f_3)$$

with the equivalent reluctances, \mathcal{R}_{ei} , and the source elements, f_{ei} , being given by

$$\mathcal{R}_{e1} = \mathcal{R}_1 + 2\mathcal{R}_2 + 2\mathcal{R}_3,$$

$$\mathcal{R}_{e2} = \mathcal{R}_4 + \mathcal{R}_6,$$

$$\mathcal{R}_{e3} = \mathcal{R}_8 + \mathcal{R}_9,$$

and

$$f_{e1} = 2f_m,$$

$$f_{e2} = f_a + f_b,$$

$$f_{e3} = f_b + f_c,$$

respectively. The expressions of the reluctance elements and MMF sources are the following:

$$\mathcal{R}_1 = \frac{\frac{4}{3}x_6}{\mu_0\mu_r x_2 2\pi(x_1 + 0.5x_2)},$$

$$\mathcal{R}_2 = \frac{0.5x_2}{\mu_0\mu_r x_6 2\pi(x_1 + 0.75x_2)},$$

$$\mathcal{R}_3 = \frac{x_3}{\mu_0 x_6 2\pi(x_1 + x_2 + 0.5x_3)},$$

$$\mathcal{R}_4 = \frac{g}{\mu_0 \frac{4}{3} x_6 2\pi(x_1 + x_2 + x_3 + 0.5g)},$$

$$\mathcal{R}_5 = \frac{g}{\mu_0 \frac{2}{3} x_6 2\pi(x_1 + x_2 + x_3 + 0.5g)},$$

$$\mathcal{R}_6 = \frac{t_t + 0.5x_4}{\mu_0\mu_r x_7 2\pi(x_1 + x_2 + x_3 + g + 0.5t_t + 0.25x_4)},$$

$$\mathcal{R}_7 = \frac{2x_8}{\mu_0 x_4 2\pi(x_1 + x_2 + x_3 + g + t_t + 0.5x_4)},$$

$$\mathcal{R}_8 = \frac{0.5(x_4 + x_5)}{\mu_0\mu_r x_7 2\pi(x_1 + x_2 + x_3 + g + t_t + 0.75x_4 + 0.5x_5)},$$

$$\mathcal{R}_9 = \frac{\frac{2}{3}x_6}{\mu_0\mu_r x_5 2\pi(x_1 + x_2 + x_3 + g + t_t + x_4 + 0.5x_5)},$$

$$f_m = x_3 \frac{B_r}{\mu_0},$$

$$f_{a,c} = \frac{1}{4} k_f x_4 x_8 J_p,$$

$$f_b = \frac{1}{2} k_f x_4 x_8 J_p.$$

B.3 MEC model from Section 5.3.2

The following system matrix and source vector are associated to the MEC circuit from Fig. 5.5:

$$\mathbf{R} = \begin{pmatrix} -1 & 1 & 1 & 0 & 0 & 0 & 0 & 0 & 0 & 0 \\ 1 & 0 & 0 & 0 & 0 & 0 & 0 & 0 & -1 & -1 \\ 0 & 0 & 0 & -1 & -1 & 0 & -1 & 0 & 0 & 1 \\ 0 & 0 & 0 & 0 & 0 & 1 & 0 & -1 & 1 & 0 \\ 0 & -1 & -1 & 0 & 0 & 0 & 0 & 1 & 0 & 0 \\ \mathcal{R}_{e1} & \mathcal{R}_{e2} & 0 & \mathcal{R}_{e4} & 0 & \mathcal{R}_{e6} & 0 & \mathcal{R}_{e8} & 0 & \mathcal{R}_{e10} \\ \mathcal{R}_{e1} & 0 & \mathcal{R}_{e3} & 0 & \mathcal{R}_{e5} & \mathcal{R}_{e6} & 0 & \mathcal{R}_{e8} & 0 & \mathcal{R}_{e10} \\ 0 & \mathcal{R}_{e2} & -\mathcal{R}_{e3} & 0 & 0 & 0 & 0 & 0 & 0 & 0 \\ 0 & 0 & 0 & \mathcal{R}_{e4} & 0 & 0 & -\mathcal{R}_{e7} & 0 & 0 & 0 \\ \mathcal{R}_{e1} & 0 & \mathcal{R}_{e3} & 0 & 0 & 0 & 0 & \mathcal{R}_{e8} & \mathcal{R}_{e9} & 0 \end{pmatrix}$$

and

$$\mathbf{f} = (0 \ 0 \ 0 \ 0 \ 0 \ 2f_m \ 2f_m \ 0 \ f_m \ f_m)$$

with the equivalent reluctances, \mathcal{R}_{ei} , and the source element, f_m , being given by

$$\begin{aligned} \mathcal{R}_{e1} &= \mathcal{R}_1 + \mathcal{R}_2, \\ \mathcal{R}_{e2} &= \mathcal{R}_4 + \mathcal{R}_7 + \mathcal{R}_{10}, \\ \mathcal{R}_{e3} &= \mathcal{R}_8 + \mathcal{R}_{11}, \\ \mathcal{R}_{e4} &= \mathcal{R}_5 + \mathcal{R}_9 + \mathcal{R}_{12}, \\ \mathcal{R}_{e5} &= \mathcal{R}_6 + \mathcal{R}_{13}, \\ \mathcal{R}_{e6} &= \mathcal{R}_{14}, \\ \mathcal{R}_{e7} &= \mathcal{R}_{15} + \mathcal{R}_{16}, \\ \mathcal{R}_{e8} &= \mathcal{R}_{18}, \\ \mathcal{R}_{e9} &= \mathcal{R}_{17}, \\ \mathcal{R}_{e10} &= \mathcal{R}_3 + \mathcal{R}_{19}, \end{aligned}$$

and

$$f_m = x_5 \frac{B_r}{\mu_0},$$

respectively. The expressions of the reluctance elements are the following:

$$\mathcal{R}_1 = \frac{x_7 + 0.5z}{\mu_0 \mu_r x_2 2\pi (x_1 + 0.5x_2)},$$

$$\begin{aligned}
\mathcal{R}_2 &= \frac{x_3}{\mu_0 \mu_r (x_7 - z) 2\pi (x_1 + x_2 + 0.5x_3)}, \\
\mathcal{R}_3 &= \frac{x_4}{\mu_0 \mu_r (x_7 - z) 2\pi (x_1 + x_2 + 0.5x_4)}, \\
\mathcal{R}_4 &= \frac{m_t - x_3}{\mu_0 (x_7 - z) 2\pi (x_1 + x_2 + 0.5(m_t + x_3))}, \\
\mathcal{R}_5 &= \frac{m_t - x_4}{\mu_0 (x_7 - z) 2\pi (x_1 + x_2 + 0.5(m_t + x_4))}, \\
\mathcal{R}_6 &= \frac{0.6r_2}{\mu_0 0.5(S_1 + S_2)}, \\
\mathcal{R}_7 &= \frac{g}{\mu_0 (x_7 - z) 2\pi (x_1 + x_2 + m_t + 0.5g)}, \\
\mathcal{R}_8 &= \frac{m_t + g}{\mu_0 z 2\pi (x_1 + x_2 + 0.5(m_t + g))}, \\
\mathcal{R}_9 &= \frac{g}{\mu_0 (x_7 - z) 2\pi (x_1 + x_2 + m_t + 0.5g)}, \\
\mathcal{R}_{10} &= \frac{x_5}{\mu_0 (x_7 - z) 2\pi (x_1 + x_2 + m_t + g + 0.5x_5)}, \\
\mathcal{R}_{11} &= \frac{x_5}{\mu_0 z 2\pi (x_1 + x_2 + m_t + g + 0.5x_5)}, \\
\mathcal{R}_{12} &= \frac{x_5}{\mu_0 (x_7 - z) 2\pi (x_1 + x_2 + m_t + g + 0.5x_5)}, \\
\mathcal{R}_{13} &= \frac{x_5}{\mu_0 z 2\pi (x_1 + x_2 + m_t + g + 0.5x_5)}, \\
\mathcal{R}_{14} &= \frac{x_7 - 0.5z}{\mu_0 \mu_r x_6 2\pi (x_1 + x_2 + m_t + g + x_5 + 0.5x_6)}, \\
\mathcal{R}_{15} &= \frac{m_t - x_4}{\mu_0 z 2\pi (x_1 + x_2 + 0.5(m_t + x_4))}, \\
\mathcal{R}_{16} &= \frac{g + x_5}{\mu_0 z 2\pi (x_1 + x_2 + m_t + 0.5(g + x_5))}, \\
\mathcal{R}_{17} &= \frac{m_t + g + x_5}{\mu_0 (x_7 - z) 2\pi (x_1 + x_2 + 0.5(m_t + g + x_5))}, \\
\mathcal{R}_{18} &= \frac{x_7 + 0.5z}{\mu_0 \mu_r x_6 2\pi (x_1 + x_2 + m_t + g + x_5 + 0.5x_6)},
\end{aligned}$$

$$\mathcal{R}_{19} = \frac{x_7 - 0.5z}{\mu_0 \mu_r x_2 2\pi (x_1 + 0.5x_2)},$$

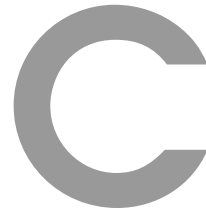
where

$$m_t = \max(x_3, x_4),$$

$$S_1 = 0.5z 2\pi (x_1 + x_2 + m_t + g),$$

$$S_2 = \begin{cases} (x_2 + m_t) 2\pi (x_1 + 0.5(x_2 + m_t)) & \text{if } x_2 + m_t \leq 0.5z \\ 0.5z 2\pi (x_1 + (x_2 + m_t - 0.5z)) & \text{if } x_2 + m_t > 0.5z, \end{cases}$$

$$r_2 = 0.5z.$$



NdFeB properties

The properties of the PM material considered for the ELMASP experimental setup from Section 5.5.4 are given in Table C.1 and the BH curve is shown in Fig. C.1.

Table C.1: NdFeB properties [90].

Type	BM35H
B_r	1.175T
bH_c	894kA/m
jH_c	1390kA/m
$(BH)_{max}$	264kJ/m ³

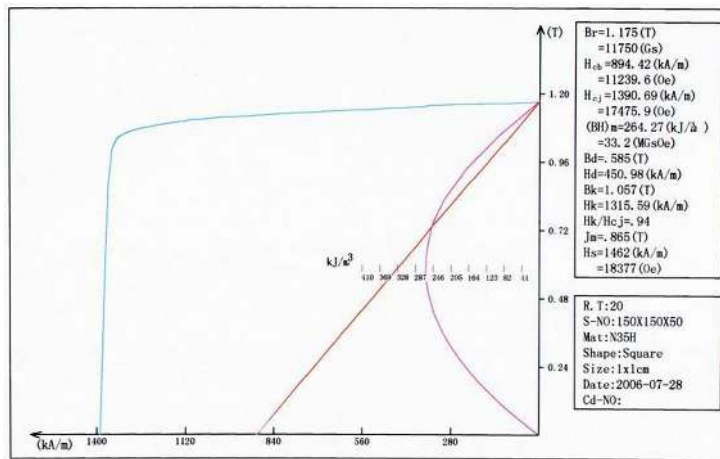


Figure C.1: Second quadrant of the BH characteristic of the permanent magnet used for the ELMASP experimental setup.

Bibliography

- [1] I. Martins, J. Esteves, G. Marques, and F. da Silva, "Permanent-magnets linear actuators for applicability in automobile active suspension," *IEEE Trans. Vehicular Technology*, vol. 55, no. 1, pp. 86 – 94, January 2006.
- [2] W. Jones, "Easy ride: Bose corp. uses speaker technology to give cars adaptive suspension," *Spectrum, IEEE*, vol. 42, no. 5, pp. 12–14, May 2005.
- [3] P. Gahlinger, "Motion sickness - how to help your patients avoid travel travail," 1999, vol. 106, no. 4, Postgraduate medicine.
- [4] T. Stoffregen and L. Smart, "Postural instability precedes motion sickness," *Brain Research Bulletin*, vol. 47, no. 5, pp. 437–448, 1998.
- [5] A. Benson, *Motion sickness*, 4th ed. Geneva: Encyclopedia of occupational health and safety, ch. 50, pp. 12-15, International Labour Office, 1998.
- [6] BMW. (2004) BMW Dynamic Drive. [Online]. Available: <http://www.bmw.com>
- [7] Jeep Cherokee. (2005) Dynamic handling system. [Online]. Available: http://www.wkjeeps.com/wk_suspension.htm
- [8] M. Bocker and R. Neuling, "Development of TRW's active roll control," *16th European mechanical dynamics users conference*, 2001.
- [9] P. Venhovens, "Optimal control of vehicle suspensions," Ph.D. dissertation, Technische Universiteit Delft, Delft, 1994.
- [10] R. Williams, "Automotive active suspensions," *IEE Coll. on Active Suspension Technology for Automotive and Railway Applications (Digest No: 1992/193)*, pp. 2/1–2/4, November 1992.
- [11] Citroen. (2001) Citroen hydraactive suspension. [Online]. Available: <http://www.citroen.com>

- [12] C. Longhurst. (2006) The suspension bible. [Online]. Available: http://www.carbibles.com/suspension_bible.html
- [13] Delphi. Delphi magneride. [Online]. Available: <http://www.delphi.com/>
- [14] Audi. Audi magnetic ride. [Online]. Available: <http://www.audi.com/>
- [15] MillenWorks. Magnetorheological fluid optimized active damper suspension (MROADS). [Online]. Available: <http://www.rodmillen.com/>
- [16] Sachs. ABC module. [Online]. Available: <http://www.zfsachs.com/>
- [17] Bose Corp. Innovative Thinking - Bose® Suspension System. [Online]. Available: <http://www.bose.com/>
- [18] T. Froeschle, R. Maresca, and J. Parison., “Electromechanical transducing along a path,” U.S. Patent 4,981,309, January, 1991.
- [19] S. Brown, “Vehicle suspension,” U.S. Patent 6,945,541, September, 2005.
- [20] Cambridge University Press. Cambridge Dictionaries Online. [Online]. Available: <http://www.dictionary.cambridge.org/>
- [21] I. Boldea, “Linear electromagnetic actuators and their control: a review,” *EPE Journal*, vol. 14, no. 1, pp. 43 – 50, February 2004.
- [22] S. Chevailler, “Comparative study and selection of criteria of linear motors,” Ph.D. dissertation, École Polytechnique Fédérale de Lausanne, Lausanne, Switzerland, 2006.
- [23] J. Søndergaard, “Optimization using surrogate models by the space mapping technique,” Ph.D. dissertation, Technical University of Denmark, Informatics and Mathematical Modeling, Lyngby, Denmark, 2003.
- [24] H. Choi, D. Kim, I. Park, and S. Hahn, “A new design technique of magnetic systems using space mapping algorithm,” *IEEE Trans. on Magnetics*, vol. 37, no. 5, pp. 3627 – 3630, September 2001.
- [25] J. Janssen, “Design of active suspension using electromagnetic devices,” Master’s thesis, Eindhoven University of Technology, Eindhoven, The Netherlands, 2006.
- [26] J. C. Dixon, *Tires, suspension and handling*, 2nd ed. London: Arnold, 1996.

- [27] BMW. (2004) BMW 5 Series Sedan Brochure. [Online]. Available: <http://www.bmw.com>
- [28] TNO Automotive Helmond, private communication.
- [29] H. Wallentowitz, "Scope for the integration of powertrain and chassis control systems: traction control - all-wheel drive - active suspension," in *Proceedings of the International Congress on Transportation Electronics*, 1990, pp. 439 – 453.
- [30] BMW. (2004) BMW 5 Series Sedan Brochure United States. [Online]. Available: <http://www.E60.net>
- [31] M. Bendsøe and O. Sigmund, *Topology optimization - theory, methods and applications*. Springer Verlag Berlin Heilderberg, 2004.
- [32] P. Venkataraman, *Applied optimization with MATLAB programming*. Wiley-Interscience, New York, 2002.
- [33] M. Bazaraa, H. Sherali, and C. Shetty, *Nonlinear programming - theory and applications (second edition)*. Wiley-Interscience, New Jersey, 2003.
- [34] J. Lagarias, J. Reeds, M. Wright, and P. Wright, "Convergence properties of the Nelder-Mead simplex method in low dimensions," *SIAM J. Optim.*, vol. 9, no. 1, pp. 112 – 147, December 1998.
- [35] J. Nocedal and S. Wright, *Numerical optimization (second edition)*. Springer, New York, 2006.
- [36] A. Conn, N. Gould, and P. L. Toint, *Trust-region methods*. SIAM, Philadelphia, 2000.
- [37] J. Bandler, R. Biernacki, S. Chen, P. Grobelny, and R. Hemmers, "Space mapping technique for electromagnetic optimization," *IEEE Trans. Microwave Theory Tech.*, vol. 42, no. 12, pp. 2536 – 2544, December 1994.
- [38] J. Bandler, Q. Cheng, S. Dakroury, A. Mohamed, M. Bakr, K. Madsen, and J. Søndergaard, "Space mapping: the state of the art," *IEEE Trans. Microwave Theory Tech.*, vol. 52, no. 1, pp. 337 – 361, January 2004.
- [39] A. Mohamed, "Recent trends in cad tools for microwave circuit design exploiting space mapping technology," Ph.D. dissertation, McMaster University, Hamilton, Ontario, 2005.

- [40] J. Snel, "Space mapping models for RF components," in *IEEE MTT-S Int. Microwave Symp. Workshop*, 2001.
- [41] D. Echeverría and P. Hemker, "Space mapping and defect correction," *Comp. Methods in Appl. Math.*, vol. 5, no. 2, pp. 107 – 136, 2005.
- [42] J. Bandler, Q. Cheng, D. Gebre-Mariam, K. Madsen, F. Pedersen, and J. Søndergaard, "EM-based surrogate modeling and design exploiting implicit, frequency and output space mappings," in *IEEE MTT-S Int. Microwave Symp. Dig.*, Philadelphia, PA, 2003, pp. 1003 – 1006.
- [43] D. Echeverría, "Multi-level optimization: space mapping and manifold mapping," Ph.D. dissertation, Centrum voor Wiskunde en Informatica, Amsterdam, The Netherlands, 2007.
- [44] K. Böhmer and H. Stetter, *Defect correction methods: theory and applications*. Springer, Berlin, 1984.
- [45] J. Bandler, R. Biernacki, S. Chen, and D. Omeragic, "Space mapping optimization of waveguide filters using finite element and mode-matching electromagnetic simulators," *Int. J. RF Microwave Computer-Aided Eng.*, vol. 9, pp. 54 – 70, 1999.
- [46] J. Bandler, R. Biernacki, S. Chen, and Y. Huang, "Design optimization of interdigital filters using aggressive space mapping and decomposition," *IEEE Trans. Microwave Theory Tech.*, vol. 45, pp. 761 – 769, May 1997.
- [47] M. Bakr, J. Bandler, and N. Georgieva, "An aggressive approach to parameter extraction," *IEEE Trans. Microwave Theory Tech.*, vol. 47, pp. 2428 – 2439, December 1999.
- [48] J. Bandler, A. Mohamed, M. Bakr, K. Madsen, and J. Søndergaard, "EM-based optimization exploiting partial space mapping and exact sensitivities," *IEEE Trans. Microwave Theory Tech.*, vol. 50, pp. 2741 – 2750, December 2002.
- [49] J. Bandler, D. Hailu, K. Madsen, and F. Pedersen, "A space-mapping interpolating surrogate algorithm for highly optimized EM-based design of microwave devices," *IEEE Trans. Microwave Theory Tech.*, vol. 52, pp. 2593 – 2600, November 2004.

- [50] S. Leary, A. Bhaskar, and A. Keane, "A constraint mapping approach to the structural optimization of an expensive model using surrogates," *Optimization and Engineering*, vol. 2, no. 4, pp. 385 – 398, 2001.
- [51] L. Encica, D. Echeverría, E. Lomonova, A. Vandenput, P. Hemker, and D. Lahaye, "Efficient optimal design of electromagnetic actuators using space-mapping," *Structural and Multidisciplinary Optimization*, vol. 33, no. 6, pp. 481 – 491, June 2007.
- [52] J. Bandler, R. Biernacki, S. Chen, R. Hemmers, and K. Madsen, "Electromagnetic optimization exploiting aggressive space mapping," *IEEE Trans. Microwave Theory Tech.*, vol. 43, pp. 2874 – 2882, December 1995.
- [53] C. Broyden, "A class of methods for solving nonlinear simultaneous equations," *Math. Comp.*, vol. 19, pp. 577 – 593, 1965.
- [54] M. Bakr, J. Bandler, R. Biernacki, S. Chen, and K. Madsen, "A trust region aggressive space mapping algorithm for EM optimization," *IEEE Trans. Microwave Theory Tech.*, vol. 46, pp. 2412 – 2425, December 1998.
- [55] M. Bakr, J. Bandler, N. Georgieva, and K. Madsen, "A hybrid aggressive space-mapping algorithm for EM optimization," *IEEE Trans. Microwave Theory Tech.*, vol. 47, pp. 2440 – 2449, December 1999.
- [56] M. Bakr, J. Bandler, K. Madsen, J. Rayas-Sánchez, and J. Søndergaard, "Space mapping optimization of microwave circuits exploiting surrogate models," *IEEE Trans. Microwave Theory Tech.*, vol. 48, pp. 2297 – 2306, December 2000.
- [57] M. Bakr, J. Bandler, K. Madsen, and J. Søndergaard, "An introduction to the space mapping technique," *Optimization and Engineering*, vol. 2, pp. 369 – 384, 2001.
- [58] J. Bandler, Q. Cheng, N. Nikolova, and M. Ismail, "Implicit space mapping optimization exploiting preassigned parameters," *IEEE Trans. Microwave Theory Tech.*, vol. 52, pp. 378 – 385, January 2004.
- [59] J. Bandler, Q. Cheng, D. Hailu, and N. Nikolova, "A space mapping design framework," *IEEE Trans. Microwave Theory Tech.*, vol. 52, pp. 2601 – 2610, November 2004.

- [60] S. Koziel, J. Bandler, and K. Madsen, "Space-mapping-based interpolation for engineering optimization," *IEEE Trans. Microwave Theory Tech.*, vol. 54, no. 6, pp. 2410 – 2421, June 2006.
- [61] D. Echeverría and P. Hemker, "On the manifold-mapping technique," Centrum voor Wiskunde en Informatica, Amsterdam, The Netherlands, Tech. Rep. MAS-R0612, 2006.
- [62] P. Hemker and D. Echeverría, "A trust-region strategy for manifold mapping optimization," *Journal of Computational Physics*, vol. 224, no. 1, pp. 464 – 475, May 2007.
- [63] K. Madsen and J. Søndergaard, "Convergence of hybrid space mapping algorithms," *Optimization and Engineering*, vol. 5, no. 2, pp. 145 – 156, 2004.
- [64] L. Vincente, "Space mapping: models, sensitivities, and trust-regions methods," *Optimization and Engineering*, vol. 4, pp. 159 – 175, 2003.
- [65] S. Koziel, J. Bandler, and K. Madsen, "Towards a rigorous formulation of the space mapping technique for engineering design," in *Int. Symp. Circuits Syst. (ISCAS 2005)*, Kobe, Japan, 2005, pp. 5605 – 5608.
- [66] L. Encica, J. Paulides, E. Lomonova, and A. Vandenput, "Aggressive output space-mapping optimization for electromagnetic actuators," *IEEE Trans. on Magnetics*, vol. 44, no. 6, pp. 1106 – 1109, June 2008.
- [67] J. Paulides, L. Encica, E. Lomonova, and A. Vandenput, "Optimal design of a long-stroke constant-force actuator," in *16th International Conference on the Computation of Electromagnetic Fields (COMPUMAG 2007)*, Aachen, Germany, 2007.
- [68] M. Redhe and L. Nilsson, "Optimization of the new saab 9-3 exposed to impact load using a space mapping technique," *Structural and Multidisciplinary Optimization*, vol. 27, pp. 411 – 420, 2004.
- [69] D. Finkel, "Direct optimization algorithm user guide," Centre Res. Sci. Comput., North Carolina State University, Raleigh, NC, Tech. Rep. CRSC-TR03-11, 2003.
- [70] D. Echeverría, D. Lahaye, L. Encica, and P. Hemker, "Optimization in electromagnetics with the space-mapping technique," *COMPEL: The International Journal for Computation and Mathematics in Electrical and Electronic Engineering*, vol. 24, no. 3, pp. 952 – 966, 2005.

- [71] R. Saldanha, S. Pelissier, K. Kadded, Y. Yonnet, and J. Coulomb, "Non-linear optimization methods applied to magnetic actuators design," *IEEE Trans. on Magnetics*, vol. 28, no. 2, pp. 1581 – 1584, March 1992.
- [72] L. Encica, E. Lomonova, and A. Vandenput, "A study of the space mapping approach to the inverse design problem of a coreless actuator," in *11th International Power Electronics and Motion Control Conference*, Riga, Latvia, 2004.
- [73] L. Encica, J. Makarovic, E. Lomonova, and A. Vandenput, "Space mapping optimization of a cylindrical voice coil actuator," *IEEE Trans. on Industry Applications*, vol. 42, no. 6, pp. 1437 – 1444, November - December 2006.
- [74] D. Echeverría, D. Lahaye, L. Encica, E. Lomonova, P. Hemker, and A. Vandenput, "Manifold-mapping optimization applied to linear actuator design," *IEEE Trans. on Magnetics*, vol. 42, no. 4, pp. 1183 – 1186, April 2006.
- [75] L. Encica, J. Paulides, D. Echeverria, E. Lomonova, and A. Vandenput, "A framework for efficient automated optimal design of electromagnetic actuators," in *12th Biennial IEEE Conference on Electromagnetic Field Computation*, Miami, USA, 2006.
- [76] J. Paulides, L. Encica, E. Lomonova, and A. Vandenput, "Active roll compensation for automotive applications using a brushless direct-drive linear permanent magnet actuator," in *37th IEEE Power Electronics Specialists Conference (PESC 2006)*, Jeju, Korea, 2006, pp. 1 – 6.
- [77] —, "Design considerations for a semi-active electromagnetic suspension system," *IEEE Trans. on Magnetics*, vol. 42, no. 10, pp. 3446 – 3448, October 2006.
- [78] L. Encica, J. Paulides, E. Lomonova, and A. Vandenput, "Electromagnetic and thermal design of a linear actuator using output polynomial mapping," *IEEE Trans. on Industry Applications*, vol. 44, no. 2, pp. 534 – 542, March-April 2008.
- [79] M. Dubois, "Optimized permanent magnet generator topologies for direct-drive wind turbines," Ph.D. dissertation, Delft University of Technology, Delft, The Netherlands, 2004.

- [80] J. Wang, G. Jewell, and D. Howe, "Design optimization and comparison of tubular permanent magnet machine topologies," *IEE Electr. Power Appl.*, vol. 148, no. 5, pp. 456 – 464, September 2001.
- [81] J. Wang and D. Howe, "Design optimization of radially magnetized, iron-cored, tubular permanent-magnet machines and drive systems," *IEEE Trans. on Magnetics*, vol. 40, no. 5, pp. 3261 – 3277, September 2004.
- [82] T. Miller, *Brushless permanent-magnet and reluctance motor drives*. Oxford University Press, 1993.
- [83] H. Roters, *Electromagnetic devices (first edition)*. John Wiley & Sons, New York, 1941.
- [84] *Maxwell 2D User Manual*, Ansoft Corp., 225 West Station Square Drive, Pittsburg, USA, 2006.
- [85] S. Brenner and R. Scott, *The mathematical theory of finite element methods (second edition)*. Springer-Verlag, Berlin, 2002.
- [86] J. Jin, *The finite element method in electromagnetics (second edition)*. Wiley-Interscience, Chichester, 2002.
- [87] J. Janssen, J. Paulides, E. Lomonova, and A. Vandenput, "Cogging force reduction in tubular permanent magnet actuators," in *IEMDC 2007*, 2007.
- [88] J. Paulides, "High performance 1.5mw 20000rpm permanent magnet generator with uncontrolled rectifier for 'more-electric' ship applications," Ph.D. dissertation, University of Sheffield, Sheffield, UK, 2005.
- [89] *ASTM Standard D2307 2007a: Standard Test Method for Thermal Endurance of Film-Insulated Round Magnet Wire*, ASTM International, West Conshohocken, PA, 2007.
- [90] Bakker Magnetics. Sciencepark Eindhoven 5502, 5692 EL Son, The Netherlands. [Online]. Available: <http://www.bakkermagnetics.com>
- [91] J. Paulides, E. Lomonova, and A. Vandenput, "Spring, assembly of spring and a damper, as well as a vehicle," Patent WO 2008/004854, January, 2008.

-
- [92] F. V. Berghen and H. Bersini, “CONDOR, a new parallel, constrained extension of powell’s UOBYQA algorithm: Experimental results and comparison with the DFO algorithm,” *Journal of Computational and Applied Mathematics*, vol. 181, pp. 157–175, September 2005.
- [93] L. Encica, J. Paulides, E. Lomonova, A. Vandenput, and B. van Leeuwen, “Spring, assembly of springs, assembly of a spring and a damper, as well as a vehicle comprising a spring,” Patent WO 2008/004871, January, 2008.
- [94] S. Koziel, J. Bandler, and K. Madsen, “Coarse model quality estimation for space mapping optimization algorithms,” in *Second Int. Workshop on Surrogate Modelling and Space Mapping for Engineering Optimization (SMSMEO-06)*, Lyngby, Denmark, 2006.

Summary

A novel proof-of-concept actuator topology for a fully electromagnetic active suspension solution that can provide both a zero-power spring characteristic and actuation forces necessary for vibration damping and vehicle body-roll control is proposed in this thesis. The commercially available active suspension systems are based on hydraulic or pneumatic solutions which are characterized by high cost and low response bandwidth. In contrast, an electromagnetic system can offer a high bandwidth at a reduced cost. However, an electromagnetic solution is highly constrained by the available space envelope, power supply requirements and thermal behavior, therefore, giving rise to a challenging design optimization problem, where a standard approach for the direct optimization, using highly accurate numerical models, becomes a time consuming process. As a result, the range of possible design choices, e.g., investigation of various topologies and/or materials, is restricted. However, the surrogate modeling techniques have been developed to address this issue, i.e., fast surrogate models are intended to replace the expensive model for the purpose of modeling or optimization of the latter. The space-mapping technique is a type of surrogate-based optimization method concept which allows expensive electromagnetic optimization to be performed efficiently with the help of inexpensive coarse models. Prior to the work related to this thesis only one publication has considered the space-mapping technique for the design of an electromagnetic actuator. Hence, an overview of the space-mapping optimization technique and publications resulted from the framework of this thesis is presented. Additionally, a new algorithm variant, i.e., aggressive output space-mapping, is introduced.

An intermediate design solution for electromagnetic active suspension is investigated at first, i.e., a hybrid solution consisting of a tubular brushless permanent magnet actuator connected in parallel with a mechanical spring. The concept is validated by a number of pre-design solutions obtained by means of the proposed algorithm variant for different actuator configurations. The obtained results indicate that a high force density actuator is required for the electromagnetic active suspension and that the considered slotted tubular per-

manent magnet actuator can fulfill the requirements. However, a suspension system based solely on this actuator type, i.e., without the addition of a mechanical spring for vehicle mass support, would not be viable due to the high power consumption, inadequate total volume and the required continuous supply of electrical energy. Consequently, an actuator that covers the performance envelope by means of a passive (zero-power) response and an active operation regime is required, which demands the development of a novel actuator concept. In this solution, all conventional mechanical suspension parts are removed. The passive spring is implemented by exploiting the cogging force component given by the attraction between permanent magnets and a slotted iron topology. The dynamic forces on the suspension, due to road noise, bumps or rolling tendency of the vehicle in corners, are compensated by actuation force generated by means of the incorporated excitation coils. The predicted passive linear spring characteristic is confirmed by means of an experimental prototype. This device is denoted in this thesis as the electromagnetic spring (ELMASP) and is characterized by a non-repetitive geometrical configuration with sloped stator teeth, a linear passive response for a stroke range of 0.175m with a stiffness of 30kN/m and a peak force of 6.5kN, and a commutated coil which provides a constant shift of the force profile for a constant excitation current, independent of the translator position. No other single actuator solution with these characteristics has been investigated in the literature up to this moment and two patents are issued to cover the passive and active design concepts.

Acknowledgments

The research related to this thesis has been carried out within the Electromechanics and Power Electronics (EPE) group at the Eindhoven University of Technology. This work would not have been possible without the support and contribution of my supervisors and colleagues.

My sincere and utmost gratitude goes to the late Professor André Vandenput for giving me the opportunity to work on this project, towards the Ph.D. degree, and for his always kind guidance and support during the years that I had the chance to work with him. I am honored to have been conducting research under his supervision and my sincere thoughts are with his wife, Mrs. Lisette Vandenput, and family.

I would like to express my deepest thanks to Elena Lomonova. Next to being my daily supervisor, she has been my guide since I came to the Netherlands for the first time. Her advices about both professional and personal matters have provided me with an invaluable support.

I wish to thank Professor Pieter Hemker for his guidance and help with the mathematical aspects of space-mapping and my colleagues from CWI Amsterdam, David Echeverría and Domenico Lahaye, for a valuable and interesting collaboration.

My sincere thanks to Johan Paulides for his many original ideas, help with the experimental setup, and, foremost, his friendship.

I am grateful to all my colleagues from the EPE group for a great working atmosphere and an exceptional social environment. Wherever my future may lead me, I will always have a special memory about this group.

Curriculum Vitae

Laurențiu Encică was born on 12th of June 1978 in Bucharest, Romania. He attended secondary school at the National College "Gheorghe Lazăr", Bucharest. In 2002 he received the Dipl.-Ing. degree from the University "Politehnica" of Bucharest. His graduation project has been carried out in 2002 during his traineeship within the Electromechanics and Power Electronics (EPE) group at the Eindhoven University of Technology. The subject of the project was the hybrid modeling and optimization of electromagnetic devices. From August 2003 he continued his research in the field of design and optimization of electromagnetic linear actuators at the EPE group towards the Ph.D. degree, which resulted in this thesis.